

©Copyright 2013

John Stakely Keller



A Search for the Neutral Higgs Bosons of the Minimal
Supersymmetric Standard Model with the ATLAS Detector at the
Large Hadron Collider

John Stakely Keller

A dissertation
submitted in partial fulfillment of the
requirements for the degree of

Doctor of Philosophy

University of Washington

2013

Reading Committee:

Anna Goussiou, Chair

Ann Nelson

Henry Lubatti

Program Authorized to Offer Degree:
Department of Physics

University of Washington

Abstract

A Search for the Neutral Higgs Bosons of the Minimal Supersymmetric Standard Model
with the ATLAS Detector at the Large Hadron Collider

John Stakely Keller

Chair of the Supervisory Committee:
Professor Anna Goussiou
Department of Physics

A search for the neutral Higgs bosons of the Minimal Supersymmetric Standard Model (MSSM), produced in proton-proton collisions recorded by the ATLAS detector, is presented. The data correspond to an integrated luminosity of 20.3 fb^{-1} , with a center of mass energy of 8 TeV. The search focuses on final states where the Higgs bosons decay into a $\tau^+\tau^-$ pair, with one τ lepton decaying leptonically and the other hadronically. Two analyses are performed which separately target low-mass and high-mass Higgs bosons, with the former divided into two sub-channels based on the presence or absence of a b-jet in final state. No evidence of new Higgs bosons is found, and upper limits are set on the cross-section times branching ratio of such Higgs bosons, and on the MSSM parameters m_A and $\tan\beta$.

TABLE OF CONTENTS

	Page
List of Figures	iii
List of Tables	vii
Chapter 1: Introduction	1
Chapter 2: Theory	3
2.1 The Standard Model	3
2.2 The Higgs mechanism	6
2.3 Supersymmetry	9
2.4 The Higgs Sector of the MSSM	12
Chapter 3: Apparatus	17
3.1 The Large Hadron Collider	17
3.2 ATLAS	20
Chapter 4: Samples	29
4.1 Data Sample	29
4.2 Monte Carlo Simulated Samples	29
Chapter 5: Reconstruction	32
5.1 Track reconstruction	32
5.2 Vertexing	32
5.3 Muons	34
5.4 Electrons	34
5.5 Jets	35
5.6 b-tagging	36
5.7 Tau leptons	37
5.8 Missing transverse energy	42
5.9 Resolving ambiguity in object selection	43

Chapter 6:	Event Selection	45
6.1	Pre-selection	45
6.2	Low-mass selection	46
6.3	High-mass selection	50
6.4	Mass reconstruction	51
Chapter 7:	Background Estimation	54
7.1	$Z \rightarrow \tau\tau$ background modelling	54
7.2	Multi-jet background modelling	56
7.3	Modelling of backgrounds with jets faking taus	61
7.4	Other backgrounds	64
7.5	Performance of background modelling	67
Chapter 8:	Systematic Uncertainties	74
8.1	Systematic Uncertainties due to background estimation	74
8.2	Systematic Uncertainties from Theory	75
8.3	Detector-related Systematic Uncertainties	77
Chapter 9:	Statistical Procedure	88
Chapter 10:	Results	91
Chapter 11:	Summary and Conclusions	97
Bibliography	99

LIST OF FIGURES

Figure Number	Page
2.1 The particles of the Standard Model.	4
2.2 The Higgs potential.	7
2.3 One loop corrections to the Higgs mass from a fermion and from a scalar. . .	10
2.4 The particle content of the MSSM. Scalar bosons are pictured in blue, spin-1/2 fermions in red, and spin-1 bosons in green. Also pictured are the hypothetical spin-2 graviton (G), and the spin-3/2 gravitino (\tilde{G}).	11
2.5 The masses of the charged and CP-even neutral Higgs bosons, as a function of mass of the CP-odd Higgs boson A . Plot from Reference [1]. The SUSY parameters have been chosen such that the quantum corrections maximize the mass of h	13
2.6 The branching ratio for h (top left), H (top right), and A (bottom), for $\tan\beta = 30$. Plots from Reference [1].	15
2.7 The leading-order diagrams for the dominant Higgs boson production mechanisms in the MSSM: gluon fusion (left), and b quark-associated production (right).	16
3.1 The CERN accelerator complex.	18
3.2 The LHC.	19
3.3 The ATLAS detector.	20
3.4 The ATLAS Inner Detector.	22
3.5 A view of the barrel portion of the ATLAS Inner detector.	23
3.6 The ATLAS calorimeters.	24
3.7 Detail of electromagnetic calorimeter module, indicating the granularity in each of the three layers.	24
3.8 The ATLAS Muon Spectrometer.	26
3.9 Schematic layout of one quadrant of the ATLAS Muon Spectrometer.	27
5.1 An illustration of the interactions of several types of particles within the ATLAS detector.	33
5.2 Event display including a b -tagged jet in the ATLAS detector. The secondary vertex and large impact parameters of the associated tracks are clearly visible.	37

5.3	Some variables used to distinguish hadronic taus from jets or from electrons. Upper left: R_{track} , the p_T -weighted average track distance from the jet center. Upper right: f_{core}^{corr} , the pileup-corrected fraction of the tau's energy within the core cone of $\Delta R < 0.1$. Lower left: S_T^{flight} , the transverse distance significance of the secondary vertex. Lower right: The fraction of high-threshold TRT hits for the leading track.	41
5.4	Variables used to reject muons faking taus. Left: f_{EM} , the electromagnetic fraction of the tau candidate's calorimeter energy. The two populations for muons correspond to the cases where the muon itself does or does not deposit energy in the calorimeter. Right: The ratio of the ID track p_T to the calorimeter energy. Shown for the category with low- f_{EM} , in the region of the calorimeter with poor muon coverage.	43
6.1	The variable $\Sigma\Delta\phi$ for the electron and muon channels, after the pre-selection requirements. A cut is made at 3.3. The signal contribution has been scaled up to increase visibility. The shaded bands indicate the total systematic uncertainty. See Section 7 for details on the background prediction.	47
6.2	The transverse mass between the lepton and E_T^{miss} for the electron and muon channels, after the cut on $\Sigma\Delta\phi$. A cut is made at 60 GeV in the b-veto sub-channel, and 45 GeV in the b-tag sub-channel. The signal contribution has been scaled up to increase visibility. The shaded bands indicate the total systematic uncertainty. See Section 7 for details on the background prediction.	48
6.3	Left: The b-tagging score (known as "MV1") for the leading jet in the event, after the cut on $\Sigma\Delta\phi$. Jets with a score above 0.7892 are considered "b-tagged". Right: The number of jets with transverse mass above 30 GeV, after requiring a 20 GeV b-tagged jet. No jets are allowed above 30 GeV other than the leading b-tagged jet. Electron and muon channels are combined. The shaded bands indicate the total systematic uncertainty. See Section 7 for details on the background prediction.	49
6.4	The azimuthal angle between the lepton and hadronic tau, for the electron and muon channels, after the cut on $\Sigma\Delta\phi$. A cut is made at 2.4 in the high-mass selection. The shaded bands indicate the total systematic uncertainty. See Section 7 for details on the background prediction.	50

6.5	The transverse mass of the hadronic tau minus the transverse mass of the lepton, after the cuts on $\Sigma\Delta\phi$ and $\Delta\phi(\text{lepton}, \tau_{\text{had}})$. Electron and muon channels are combined. A cut is made at 45 GeV in the high-mass selection. As explained in Section 7, the background estimation procedure is different for the low-mass and high-mass channels. The low-mass estimate has been used for the plot on the left, showing good agreement for the bulk of the distribution. The high-mass estimate has been used for the plot on the right, showing improved agreement in the high-mass signal region. The shaded bands indicate the total systematic uncertainty. See Section 7 for details on the background prediction.	51
6.6	Example of the probability distribution functions $\mathcal{P}(\Delta\theta, p_\tau)$ for a particular value of the original τ lepton momentum ($45 < p_\tau \leq 50$ GeV). These functions are used in the calculation of the global event probability $\mathcal{P}_{\text{event}}$ for three cases: leptonic decays (left plot), 1-prong taus (middle plot), and 3-prong taus (right plot). These distributions depend only on the decay type and initial momentum of the tau.	53
7.1	Example event displays of the embedding steps for a single $Z \rightarrow \mu\mu$ to $Z \rightarrow \tau\tau$ event: (a) after the selection, (b) after the Monte Carlo simulation, and (c) after the re-reconstruction.	56
7.2	The ratio of opposite-sign to same-sign multijet events measured in the anti-isolated regions, as a function of the ditau visible mass.	62
7.3	The transverse momentum of the hadronic tau for the electron and muon channels, after the cut on $\Sigma\Delta\phi$. The shaded bands indicate the total systematic uncertainty.	67
7.4	The transverse momentum of the electron or muon, after the cut on $\Sigma\Delta\phi$. The shaded bands indicate the total systematic uncertainty.	68
7.5	The missing trasverse energy for the electron and muon channels, after the cut on $\Sigma\Delta\phi$. The shaded bands indicate the total systematic uncertainty. . .	68
7.6	The invariant mass of the lepton and the hadronic tau, after the cut on $\Sigma\Delta\phi$. The shaded bands indicate the total systematic uncertainty.	69
7.7	The transverse momentum of the hadronic tau for the electron and muon channels, after the b-tag and prior to the veto on a second jet. The shaded bands indicate the total systematic uncertainty.	70
7.8	The transverse momentum of the electron or muon, after the b-tag and prior to the veto on a second jet. The shaded bands indicate the total systematic uncertainty.	71
7.9	The missing trasverse energy for the electron and muon channels, after the b-tag and prior to the veto on a second jet. The shaded bands indicate the total systematic uncertainty.	71

7.10	The invariant mass of the lepton and the hadronic tau, after the b-tag and prior to the veto on a second jet. The shaded bands indicate the total systematic uncertainty.	72
7.11	The p_T of the hadronic tau, after the cuts $\Sigma\Delta\phi < 3.3$ and $\Delta\phi(\tau,\text{lep}) < 2.4$. The plot on the left uses the low-mass b-veto background estimation technique, while the right uses the high-mass technique. The shaded bands indicate the total systematic uncertainty.	73
8.1	The effect of the embedding uncertainties on the ditau MMC mass distribution, shown for the low-mass b-veto selection.	76
10.1	Final invariant mass distributions after the low-mass b-veto selection, for the electron (left) and muon (right) sub-channels.	92
10.2	Final invariant mass distributions after the low-mass b-tag selection, for the electron (left) and muon (right) sub-channels.	92
10.3	Final invariant mass distributions after the high mass selection. Electron and muon events are combined.	93
10.4	Upper limit on $\tan\beta$ as a function of m_A , obtained from the low-mass analysis. The b-tag and b-veto sub-channels are combined.	94
10.5	Upper limit on $\tan\beta$ as a function of m_A , obtained from the low-mass b-tag (left) and b-veto (right) analyses.	94
10.6	Upper limit on $\tan\beta$ as a function of m_A , obtained from the high-mass analysis.	95
10.7	Upper limit on the cross-section times branching ratio for a new scalar boson produced via gluon fusion (left) or b-associated production (right), obtained from the low-mass analysis. The b-tag and b-veto sub-channels are combined.	95
10.8	Upper limit on the cross-section times branching ratio for a new scalar boson produced via gluon fusion (left) or b-associated production (right), obtained from the high-mass analysis.	96

LIST OF TABLES

Table Number		Page
2.1	The couplings of the MSSM Higgs bosons to up-type fermions, down-type fermions, and W and Z bosons.	14
5.1	Selected branching ratios for tau leptons [2].	38
7.1	Definition of signal and control regions according to the charge correlation between the light lepton and the τ lepton (OS vs. SS) and the isolation of the light lepton (isolation vs. inverted isolation).	57
7.2	Observed data events and expected numbers of events from simulation in the regions B, C, and D used in the multijet background estimation in the low-mass b-tag channel. For W +jets, Z +jets and $t\bar{t}$ samples a normalization correction factor (Section 7.3) is applied to the predicted MC event yields. .	58
7.3	Observed data events and expected numbers of events from simulation in the regions B, C, and D used in the multijet background estimation in the low-mass b-veto channel. For W +jets, Z +jets and $t\bar{t}$ samples a normalization correction factor (Section 7.3) is applied to the predicted MC event yields. .	59
7.4	Observed data events and expected numbers of events from simulation in the regions B, C, and D used in the multijet background estimation in the high-mass channel. For W +jets, Z +jets and $t\bar{t}$ samples a normalization correction factor (Section 7.3) is applied to the predicted MC event yields.	60
7.5	Opposite-sign to same-sign ratio for multijet events, as measured in regions B and D.	61
7.6	Opposite-sign to same-sign ratio for multijet events, as measured in regions with the anti-isolation criteria systematically varied. Here p_T 0.4 refers to the sum of the transverse momenta of tracks within a cone of 0.4 around the lepton, while E_T 0.2 refers to the total energy of calorimeter deposits within a cone of 0.2 around the lepton.	62
7.7	Number of events in the control regions used for normalizing the $Z \rightarrow \ell\ell$ backgrounds with jets faking taus. Veto, tag, and high refer to the low-mass b-veto, low-mass b-tag, and high-mass selections, while OS and SS refer to events with opposite-sign and same-sign lepton and tau candidates. . . .	64

7.8	Number of events in the control regions used for normalizing the W+jets background. Veto, tag, and high refer to the low-mass b-veto, low-mass b-tag, and high-mass selections, while OS and SS refer to events with opposite-sign and same-sign lepton and tau candidates.	65
7.9	Number of events in the control regions used for normalizing the top quark backgrounds. Veto, tag, and high refer to the low-mass b-veto, low-mass b-tag, and high-mass selections, while OS and SS refer to events with opposite-sign and same-sign lepton and tau candidates.	66
7.10	Scale factors used for normalizing the W, top, and $Z \rightarrow \ell\ell$ backgrounds. Errors are statistical.	66
8.1	Systematic uncertainty for embedded samples: ratios of the yields after the systematic variations in the embedded samples have been applied along with their statistical uncertainties.	76
8.2	Systematic uncertainty for the simulated background sample cross sections. For the singal uncertainties see the Appendix for more details.	78
8.3	Signal acceptances for several systematic deviations of the theory parameters contributing to the higgs boson and b-quark production. The different variations are added in quadrature to a total uncertainty on the signal acceptance in the b-tag and b-veto sample.	78
8.4	Signal acceptances for several systematic deviations of the theory parameters contributing to the higgs boson production through gluon fusion. The different variations are added in quadrature to a total uncertainty on the signal acceptance in the b-tag and b-veto sample.	79
8.5	Systematic uncertainty for the ALPGEN Z+jets MC.	80
8.6	Summary of detector-related systematic uncertainties for background and signal samples after the b-tagged selection for the electron channel (%). Signal refers to bbA production with $m_A = 150$ GeV and $\tan\beta = 20$. When uncertainty is asymmetric the one with the maximum absolute value is considered.	83
8.7	Summary of detector-related systematic uncertainties for background and signal samples after the b-tagged selection for the muon channel(%). Signal refers to bbA production with $m_A = 150$ GeV and $\tan\beta = 20$. When uncertainty is asymmetric the one with the maximum absolute value is considered.	84
8.8	Summary of detector-related systematic uncertainties for background and signal samples after the b-veto selection for the electron channel (%). Signal refers to ggA production with $m_A = 150$ GeV and $\tan\beta = 20$. When uncertainty is asymmetric the one with the maximum absolute value is considered.	85

8.9	Summary of detector-related systematic uncertainties for background and signal samples after the b-veto selection for the electron channel (%). Signal refers to ggA production with $m_A = 150$ GeV and $\tan\beta = 20$. When uncertainty is asymmetric the one with the maximum absolute value is considered.	86
8.10	Summary of detector-related systematic uncertainties for background and signal samples after the high-mass selection (%). Signal refers to bbA production with $m_A = 350$ GeV and $\tan\beta = 20$. When uncertainty is asymmetric the one with the maximum absolute value is considered.	87

ACKNOWLEDGMENTS

Thanks must go first to my advisor, Anna Goussiou, for invaluable guidance throughout my graduate career. I would also like to thank all of my other colleagues from the University of Washington, especially Justin Griffiths, Nikos Rompotis, and Matthew Beckingham, who have been a constant source of help along the way. Many thanks to all of my collaborators on ATLAS, especially those in the Higgs and tau groups whom I've had the pleasure of working with directly. Thanks also to my parents, for your patient and detailed explanations of the finer points of particle physics. Finally, thank you to my pub trivia teams in Seattle and Geneva. It wouldn't have been possible without you.

DEDICATION

For my brothers, David and Charles. This counts as your Christmas present.

Chapter 1

INTRODUCTION

On July 4, 2012, the ATLAS and CMS experiments at the Large Hadron Collider announced the discovery of a new particle, consistent with the Higgs boson of the Standard Model [3] [4]. This marked the beginning of a new era in particle physics.

The Higgs boson was first hypothesized in 1964 by Peter Higgs [5] [6] [7], by Robert Brout and Francois Englert [8], and by Gerald Guralnik, C.R. Hagen, and Tom Kibble [9]. These papers describe a mechanism whereby a “massless” particle may obtain a mass dynamically, through the process of spontaneous symmetry breaking. The theory was used by Glashow [10], Weinberg [11], and Salam [12] in 1967 to unify the electromagnetic and weak interactions into a single electroweak force. Together with Quantum Chromodynamics [13], this formed the Standard Model of particle physics, which could describe the interactions of all known sub-atomic particles. The model received validation with the discoveries of the gluon [14] and W and Z bosons [15] [16] [17] [18], and by the time the top quark was found in 1995 [19] [20], the Higgs boson stood as the only missing piece in the theory.

In this sense, the 2012 discovery marks the completion of a remarkably successful model. However, though it has stood for nearly half a century, the Standard Model is known to be an incomplete theory. The mass of the Higgs boson is quadratically divergent at high energies, and needs some mechanism to explain why it remains at the electroweak scale. Additionally, it contains no particle which can account for dark matter, whose existence is strongly implied by astronomical observations. Both of these issues can be solved by introducing Supersymmetry, a space-time symmetry which relates bosonic and fermionic fields.

Supersymmetry requires the existence of a new “partner” particle (or sparticle) for every particle in the Standard Model. Additionally, it requires that Electroweak symmetry breaking comes not from a single complex doublet but from two doublets, which leads to

five physical Higgs boson states. Two of these states are charged and three are neutral, one of which must be identified with the newly discovered boson. In this scenario, then, the 2012 announcement could be just the beginning of Higgs boson discovery at the LHC.

In this thesis, a search for the additional neutral Higgs bosons of the Minimal Supersymmetric Standard Model is presented. The analysis is conducted using proton-proton collisions at a center of mass energy of 8 TeV, produced by the LHC and collected by the ATLAS detector. The search considers Higgs boson decays into two tau leptons, where one lepton decays hadronically and the other decays leptonically. Higgs boson production via gluon fusion and in association with b-quarks are considered.

The thesis is organized as follows: In chapter 2, the theoretical background is presented, including the Standard Model, the Higgs mechanism, and Supersymmetry. Chapter 3 describes the Large Hadron Collider and the ATLAS experiment. Chapter 4 summarizes the data and simulated samples used in the analysis. Chapter 5 describes the techniques used to reconstruct the particles in a collision event. Chapter 6 describes the selection criteria applied to choose potential Higgs boson events. Chapter 7 discusses the estimation of background processes. Chapter 8 summarizes the systematic uncertainties considered. Chapter 9 describes the statistical techniques used to analyze the data. Chapter 10 presents the results of the search, and Chapter 11 gives a summary.

Chapter 2

THEORY

2.1 *The Standard Model*

2.1.1 *Overview*

The Standard Model (SM) of particle physics is a gauge theory which describes all known fundamental particles and their interactions. There are three forces in the SM: the strong, electromagnetic, and weak forces. Each force is mediated by one or more spin-1 bosons, namely, the gluon, the photon, and the W and Z bosons, respectively. Matter is composed of spin-1/2 fermions. These are arranged into three “generations” of four particles each. The fermions can be divided into quarks, which interact via the strong force, and leptons, which do not. Quarks have an electric charge of either $+2/3$ (the up, charm, and top quarks) or $-1/3$ (the down, strange, and bottom quarks). Leptons have a charge of either -1 (the electron, muon, and tau) or are neutral (the e , μ , and τ neutrinos). Additionally, every fermion has an anti-fermion, with identical properties but an opposite electrical charge.

All fermion flavors interact via the weak force, but only those with left-handed parity may do so. Introducing an explicit mass term, which treats left- and right-handed components equally, would therefore violate the weak symmetry. Furthermore, as we will see, adding a mass term for any of the gauge bosons would violate the associated symmetry, and yet the W and Z bosons are observed to be massive. These difficulties are overcome by introducing a new field, the Higgs field, which due to its self-interaction is preferentially non-zero everywhere. The otherwise massless particles may obtain an apparent mass by coupling to this field. This mechanism requires the existence of one additional fundamental particle: the spin-0 Higgs boson.

The particle content of the SM is shown in Figure 2.1.

Three generations of matter (fermions)					
	I	II	III		
mass	2.4 MeV/c ²	1.27 GeV/c ²	171.2 GeV/c ²	0	7 GeV/c ²
charge	$\frac{2}{3}$	$\frac{2}{3}$	$\frac{2}{3}$	0	0
spin	$\frac{1}{2}$	$\frac{1}{2}$	$\frac{1}{2}$	1	0
name	u up	c charm	t top	γ photon	H Higgs boson
Quarks	4.8 MeV/c ²	104 MeV/c ²	4.2 GeV/c ²	0	
	$-\frac{1}{3}$	$-\frac{1}{3}$	$-\frac{1}{3}$	0	
	$\frac{1}{2}$	$\frac{1}{2}$	$\frac{1}{2}$	1	
	d down	s strange	b bottom	g gluon	
Leptons	<2.2 eV/c ²	<0.17 MeV/c ²	<15.5 MeV/c ²	91.2 GeV/c ²	
	0	0	0	0	
	$\frac{1}{2}$	$\frac{1}{2}$	$\frac{1}{2}$	1	
	ν_e electron neutrino	ν_μ muon neutrino	ν_τ tau neutrino	Z⁰ Z boson	
	0.511 MeV/c ²	105.7 MeV/c ²	1.777 GeV/c ²	80.4 GeV/c ²	
	-1	-1	-1	±1	
	$\frac{1}{2}$	$\frac{1}{2}$	$\frac{1}{2}$	1	
	e electron	μ muon	τ tau	W[±] W boson	

Figure 2.1: The particles of the Standard Model.

2.1.2 The Strong Interaction

The strong interaction is described by a gauge theory known as Quantum Chromodynamics (QCD), based on an SU(3) gauge symmetry [13]. The QCD portion of the SM lagrangian may be written as [2]:

$$\mathcal{L}_{\text{QCD}} = -\frac{1}{2} \text{tr} \mathbf{G}_{\mu\nu} \mathbf{G}^{\mu\nu} + i \bar{u} (\partial_\mu - i g_s \mathbf{G}_\mu^a T^a) \gamma^\mu u + i \bar{d} (\partial_\mu - i g_s \mathbf{G}_\mu^a T^a) \gamma^\mu d. \quad (2.1)$$

In this equation, \mathbf{G}_μ^a is the gluon field, with a running over the components of the 8 representation of SU(3). $\mathbf{G}_{\mu\nu}$ is the field strength tensor for the gluon field; the first term is the kinetic term for gluons. u and d are Dirac spinors associated with up- and down-type quarks (a sum over the 3 generations is implied); g_s is the strong coupling constant; T^a are the SU(3) generators (represented e.g. by the Gell-Mann matrices); and γ^μ are the Dirac matrices. The second and third terms therefore contain the kinetic term for quarks and the strong coupling between quarks and gluons.

An important feature of QCD is confinement. The force between two colored particles increases with distance, and it is therefore energetically impossible to separate a pair into two bare particles. Instead, as they are separated, the additional energy stored in the gluon

field leads to the production of quark-antiquark pairs to screen the color charge. This repeats until the energy in the gluon field is not enough to create another $q\bar{q}$ pair, and the produced quarks form into color-neutral bound states. From an experimental perspective, this means that individual colored particles are never observed in collisions, but rather show up as clusters of collimated hadrons, known as “jets”.

2.1.3 The Electroweak Interaction

The electromagnetic and weak (electroweak) interactions [10] [11] [12] are described by a gauge theory based on the group $SU(2) \times U(1)$. The electroweak portion of the SM lagrangian is given by:

$$\begin{aligned}
\mathcal{L}_{EW} = & -\frac{1}{4}B_{\mu\nu}B^{\mu\nu} - \frac{1}{8}\text{tr } \mathbf{W}_{\mu\nu}\mathbf{W}^{\mu\nu} \\
& + (\bar{\nu}_L, \bar{e}_L) \tilde{\sigma}^\mu i \left[\partial_\mu - i\frac{g_1}{2}B_\mu + i\frac{g_2}{2}\mathbf{W}_\mu \right] \begin{pmatrix} \nu_L \\ e_L \end{pmatrix} \\
& + \bar{e}_R \sigma^\mu i [\partial_\mu - ig_1 B_\mu] e_R + \bar{\nu}_R \sigma^\mu i \partial_\mu \nu_R + (\text{h.c.}) \\
& + (\bar{u}_L, \bar{d}_L) \tilde{\sigma}^\mu i \left[\partial_\mu - i\frac{g_1}{6}B_\mu + i\frac{g_2}{2}\mathbf{W}_\mu \right] \begin{pmatrix} u_L \\ d_L \end{pmatrix} \\
& + \bar{u}_R \sigma^\mu i \left[\partial_\mu + i\frac{2g_1}{3}B_\mu \right] u_R + \bar{d}_R \sigma^\mu i \left[\partial_\mu - i\frac{g_1}{3}B_\mu \right] d_R + (\text{h.c.})
\end{aligned} \tag{2.2}$$

Here B and \mathbf{W} are the gauge boson vector potentials for $U(1)$ and $SU(2)$, respectively, and the first line contains their kinetic terms; e and ν are the charged lepton and neutrino fields, σ are the Pauli matrices, and g_1 and g_2 are the coupling constants associated with B and \mathbf{W} . It can be seen that the left- and right-handed fermion fields are treated differently by the electroweak interaction; in particular, the left-handed components interact as a doublet under $SU(2)$ while the right-handed components interact as singlets.

\mathbf{W} is comprised of three fields, W_1 , W_2 , and W_3 . The first two of these mix to form the positive and negative W bosons observed in experiment:

$$W^\pm = \frac{1}{\sqrt{2}} (W_1 \mp iW_2) \tag{2.3}$$

The third component of \mathbf{W} mixes with B to form the massive Z field and the massless

electromagnetic field A :

$$\begin{aligned} Z &= \cos \theta_W W_3 - \sin \theta_W B \\ A &= \sin \theta_W W_3 + \cos \theta_W B \end{aligned} \tag{2.4}$$

The angle θ_W is known as the weak mixing angle or the Weinberg angle.

2.2 The Higgs mechanism

As explained above, adding explicit mass terms for the weak bosons or fermions would break the gauge symmetry. To account for the masses then, a new complex scalar field ϕ is introduced [5] [6] [7] [8] [9], which is a doublet under SU(2). We may write [21]:

$$\phi = \frac{1}{\sqrt{2}} \begin{pmatrix} \phi_1 + i\phi_2 \\ \phi_3 + i\phi_4 \end{pmatrix}. \tag{2.5}$$

The scalar field enters the lagrangian as follows:

$$\begin{aligned} \mathcal{L}_{\text{Higgs}} &= \left| \left(\partial_\mu - ig_1 \frac{Y}{2} B_\mu - ig_2 \frac{\sigma_i}{2} W_\mu^i \right) \phi \right|^2 \\ &\quad - \mu^2 \phi^\dagger \phi - \lambda (\phi^\dagger \phi)^2 \end{aligned} \tag{2.6}$$

The second line contains the Higgs potential. If both μ^2 and λ are positive, then the minimum is at zero and spontaneous symmetry breaking does not occur. If instead we have $\mu^2 < 0$, then the minimum of the potential occurs at

$$\phi^\dagger \phi = \frac{-\mu^2}{2\lambda} = \frac{v^2}{2}, \tag{2.7}$$

where we have defined v , the vacuum expectation value of the field. A graph of this potential is shown in Figure 2.2.

There are three gauge degrees of freedom from the SU(2) symmetry, and we may use these to eliminate ϕ_1 , ϕ_2 , and ϕ_4 . This implies that exactly three particles will become massive because of this interaction. We may further write $\phi_3(x) = (v + H(x))/\sqrt{2}$, where $H(x)$ is a function centered on zero. We therefore have:

$$\phi = \begin{pmatrix} 0 \\ \frac{v + H(x)}{\sqrt{2}} \end{pmatrix}. \tag{2.8}$$

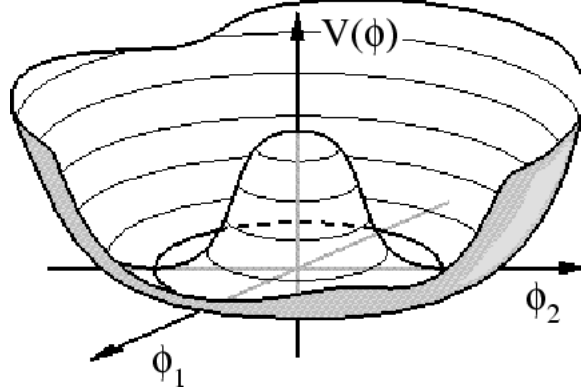


Figure 2.2: The Higgs potential.

To see the effect on the electroweak gauge bosons, we may substitute the vacuum expectation value of this field (i.e. set $H(x) = 0$) into the lagrangian. For the terms involving the gauge fields, we obtain

$$\mathcal{L}_{\text{Higgs}} = \left| \left(g_2 \frac{\sigma_i}{2} W_\mu^i + \frac{g_1}{2} B_\mu \right) \begin{pmatrix} 0 \\ \frac{v}{\sqrt{2}} \end{pmatrix} \right|^2. \quad (2.9)$$

Using the explicit representation of the Pauli matrices, this becomes:

$$\mathcal{L}_{\text{Higgs}} = \frac{g_2^2 v^2}{8} \left[(W_\mu^1)^2 + (W_\mu^2)^2 \right] + \frac{v^2}{8} (g_2 W_\mu^3 - g_1 B_\mu)^2. \quad (2.10)$$

If we write $g_1/g_2 = \tan \theta_W$, then we can substitute Equations 2.3 and 2.4 to obtain

$$\mathcal{L}_{\text{Higgs}} = \frac{1}{2} \left(\frac{gv}{2} \right)^2 \left[|W_\mu^+|^2 + |W_\mu^-|^2 \right] + \frac{1}{2} \frac{v^2 (g_1^2 + g_2^2)}{2} Z_\mu^2. \quad (2.11)$$

We therefore have positive and negative W bosons with masses

$$M_W = \frac{gv}{2} \quad (2.12)$$

and a Z boson with mass

$$M_Z = \frac{v}{2} \sqrt{g_1^2 + g_2^2} = \frac{M_W}{\cos \theta_W}. \quad (2.13)$$

The A field, orthogonal to the Z , remains massless, as expected.

The function $H(x)$ corresponds to a new particle, the Higgs boson. We may derive its couplings by substituting $(v + H(x))/\sqrt{2}$ into the above equations. To get the self-coupling, we use the Higgs potential in Equation 2.6, and obtain (up to a constant)

$$v^2\lambda H^2 + v\lambda H^3 + \frac{\lambda H^4}{4}. \quad (2.14)$$

The Higgs boson is therefore massive, with $m_H = \sqrt{2\lambda v}$, and couples to itself. The mass is not predicted by the theory. For the interactions with the gauge bosons, we may directly substitute $(v + H(x))$ for v in Equation 2.11:

$$\frac{vg^2}{2}HW^2 + \frac{g^2}{4}H^2W^2 + \frac{vg^2}{4\cos^2\theta_W}HZ^2 + \frac{g^2}{8\cos^2\theta_W}H^2Z^2. \quad (2.15)$$

The Higgs does not couple to the electromagnetic field, and is therefore electrically neutral.

2.2.1 Generation of fermion masses

Because the weak interaction treats left- and right-handed fermion fields differently, adding any explicit mass term to the Lagrangian, which would have the form $-m(\psi_L\bar{\psi}_R + \psi_R\bar{\psi}_L)$, would break the symmetry. However, the mass can be generated dynamically via interactions with the Higgs field ϕ . Explicitly, we may introduce the following interactions to the Lagrangian (taking for example the down-type quarks):

$$\mathcal{L}_{\text{Yukawa}} = -g_D \left[(\bar{u}_L, \bar{d}_L) \phi d_R + \bar{d}_R \bar{\phi} \begin{pmatrix} u_L \\ d_L \end{pmatrix} \right], \quad (2.16)$$

where g_D is the coupling constant for down-type quarks. Using the gauge freedom as before to write

$$\phi = \begin{pmatrix} 0 \\ \frac{v + H(x)}{\sqrt{2}} \end{pmatrix}. \quad (2.17)$$

we may substitute this into Equation 2.16 to obtain

$$\mathcal{L}_{\text{Yukawa}} = -\frac{g_D v}{\sqrt{2}} [\psi_L^D \bar{\psi}_R^D + \psi_R^D \bar{\psi}_L^D] - \frac{g_D H}{\sqrt{2}} [\psi_L^D \bar{\psi}_R^D + \psi_R^D \bar{\psi}_L^D]. \quad (2.18)$$

We can see that the first term is equivalent to a mass term for the fermion, with mass

$$m_D = \frac{g_D v}{\sqrt{2}}. \quad (2.19)$$

The second term corresponds to an interaction between the Higgs boson and the fermion. We can see therefore that the Higgs boson coupling to a fermion is directly proportional to the fermion's mass.

2.3 Supersymmetry

2.3.1 The Hierarchy Problem

Although the Standard Model as presented can explain with reasonable success all particle interactions observed so far at experiments, there are various theoretical and experimental reasons why it is believed to be an incomplete theory. Among the most compelling of these is the Hierarchy Problem, which deals with the unexpectedly low Higgs boson mass [22].

The mass of the Higgs boson in the Standard Model is quadratically divergent at high energies. This is addressed in Quantum Field Theory by introducing an ultraviolet cutoff scale Λ_{UV} , which must be at least as high as the scale at which new physics effects enter the theory. In particular, we may write:

$$m_H^2 = m_0^2 + \mathcal{O}(\Lambda_{UV}^2), \quad (2.20)$$

with m_0 the tree-level mass. For instance, Figure 2.3 shows the 1-loop corrections to the Higgs mass from a fermion and from a scalar boson. These diagrams change the Higgs mass by

$$\Delta m_H^2 = -\frac{|\lambda_f|^2}{8\pi^2} \Lambda_{UV}^2 + \dots \quad (2.21)$$

for the fermion and

$$\Delta m_H^2 = \frac{|\lambda_S|^2}{16\pi^2} \Lambda_{UV}^2 + \dots \quad (2.22)$$

for the boson. The problem occurs because the ultraviolet cutoff is usually thought to be somewhere around the Planck scale, which is some 15 orders of magnitude higher than the electroweak scale where the observed Higgs mass lies. If there is any Higgs coupling (even indirect coupling) to particles beyond the Standard Model, then there must be some remarkable cancellation to ensure that the Higgs mass remains at the electroweak scale. This can be accomplished either by assuming a great deal of fine-tuning in the corrections, or by introducing a new symmetry which ensures that the various corrections cancel.

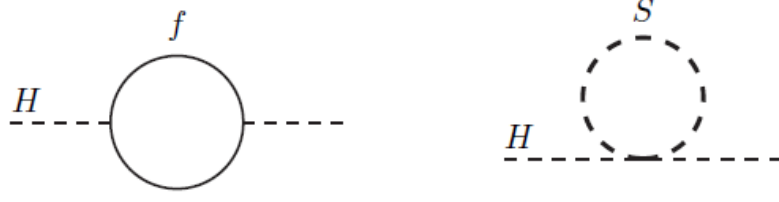


Figure 2.3: One loop corrections to the Higgs mass from a fermion and from a scalar.

Supersymmetry provides a solution to this problem by introducing a new spacetime symmetry, which transforms bosonic states into fermionic ones, and vice-versa [23]. Under supersymmetry, particles are grouped into *supermultiplets*, which must contain an equal number of bosonic and fermionic degrees of freedom. A Dirac fermion (which has two degrees of freedom) may therefore be in a supermultiplet with two scalar bosons. It is easy to see from equations 2.21 and 2.22 that the total first-order corrections to the Higgs mass from this multiplet would cancel; it can be shown that they cancel at higher orders as well.

2.3.2 The Minimal Supersymmetric Standard Model

The supermultiplet just described, containing one fermion and two scalars, is known as a chiral supermultiplet. In the Minimal Supersymmetric Standard Model (MSSM) [24], all of the SM fermions reside in chiral supermultiplets. Their supersymmetric “partners” are scalars and are denoted by prepending an “s” to the front of the names: squarks, sleptons, sneutrinos, etc. The gauge bosons of the SM must be matched with spin-1/2 fermions, in what is called a gauge supermultiplet. Because the gauge fields are massless (prior to spontaneous symmetry breaking), both the fermions and bosons in such a multiplet have two degrees of freedom. The new fermions are denoted by adding “-ino” as a suffix to the gauge boson names: Wino, gluino, etc.

As a scalar the Higgs boson must reside in a chiral supermultiplet, partnered with a *higgsino*. However, supersymmetry dictates that the single SU(2) Higgs doublet introduced in the previous section is insufficient; two doublets with opposite hypercharge must give mass separately to the up-type and down-type fermions. We will discuss the implications of this

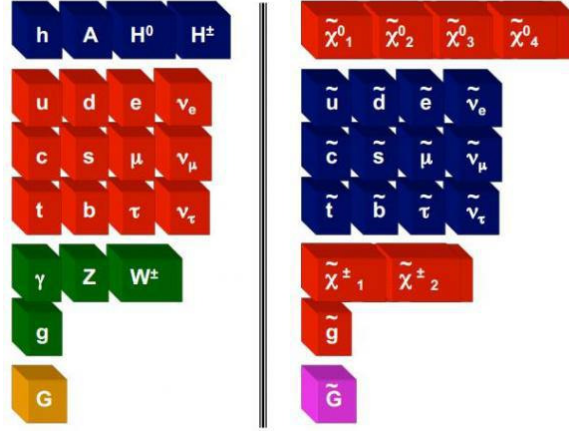


Figure 2.4: The particle content of the MSSM. Scalar bosons are pictured in blue, spin-1/2 fermions in red, and spin-1 bosons in green. Also pictured are the hypothetical spin-2 graviton (G), and the spin-3/2 gravitino (\tilde{G}).

in more detail in the next section.

In total there are four color-neutral and electrically-neutral supersymmetric fermions (the neutral Wino, the Bino, and two neutral higgsinos), and four color-neutral charged supersymmetric fermions (the charged Winos and higgsinos). The observable mass eigenstates are a mixture of these fields, known as neutralinos (χ^0) and charginos (χ^\pm). The full particle content of the MSSM can be seen in Figure 2.4.

If supersymmetry were an exact symmetry of nature, all members of a supermultiplet would have the same mass. Current limits from direct searches at the LHC place the minimum squark and gluino masses above about 1 TeV, depending on the details of the model. It is clear therefore that SUSY is a broken symmetry. This is done by introducing a “soft” supersymmetry breaking term into the Lagrangian:

$$\mathcal{L} = \mathcal{L}_{SUSY} + \mathcal{L}_{soft}, \quad (2.23)$$

where \mathcal{L}_{SUSY} is exactly invariant under a supersymmetric transformation. \mathcal{L}_{soft} denotes the fact that the SUSY-breaking terms contain only parameters with positive mass dimension. In this way, the relation between the dimensionless parameters is unchanged, allowing the divergent corrections to the Higgs mass to still cancel.

2.4 The Higgs Sector of the MSSM

As mentioned before, the structure of supersymmetry requires two scalar doublets to generate masses separately for the up- and down-type fermions. We may write these explicitly as [1]:

$$\phi_1 = \begin{pmatrix} \phi_1^0 \\ \phi_1^+ \end{pmatrix}, \quad \phi_2 = \begin{pmatrix} \phi_2^- \\ \phi_2^0 \end{pmatrix}. \quad (2.24)$$

Because each component of the doublets is complex, there are now eight Higgs fields. As before, however, three of the fields may be set to zero by the gauge freedom, which corresponds to the Higgs fields giving mass to the W^+ , W^- , and Z bosons. The remaining fields are the real parts of the charged components, the real parts of the neutral components, and one of the imaginary parts of the neutral components. These correspond to the five observable Higgs bosons of the MSSM: the charged bosons H^+ and H^- , the neutral and CP-even H and h (H is conventionally chosen as the heavier), and the CP-odd A .

In order for spontaneous symmetry breaking to occur, we must again assume that the Higgs fields have non-zero vacuum expectation values. Expanding about these minima we may write:

$$\phi_1 = \begin{pmatrix} v_1 + H_1^0 + iA_1^0 \\ H^+ \end{pmatrix}, \quad \phi_2 = \begin{pmatrix} H^- \\ v_2 + H_2^0 + iA_2^0 \end{pmatrix}. \quad (2.25)$$

The physical Higgs states are formed as mixtures of these fields, as follows:

$$\begin{pmatrix} h \\ H \end{pmatrix} = \begin{pmatrix} \cos \alpha & \sin \alpha \\ -\sin \alpha & \cos \alpha \end{pmatrix} \begin{pmatrix} H_1^0 \\ H_2^0 \end{pmatrix} \quad (2.26)$$

$$\begin{pmatrix} G^0 \\ A \end{pmatrix} = \begin{pmatrix} \cos \beta & \sin \beta \\ -\sin \beta & \cos \beta \end{pmatrix} \begin{pmatrix} A_1^0 \\ A_2^0 \end{pmatrix}, \quad (2.27)$$

where G^0 is the Goldstone boson responsible for generating the Z boson mass. The mixing angle β is related to the vacuum expectation values by $\tan \beta = \frac{v_2}{v_1}$. The charged Higgs mass, the three neutral Higgs masses, and the two mixing angles α and β determine the Higgs sector of the theory. However, supersymmetry tightly constrains what terms may appear

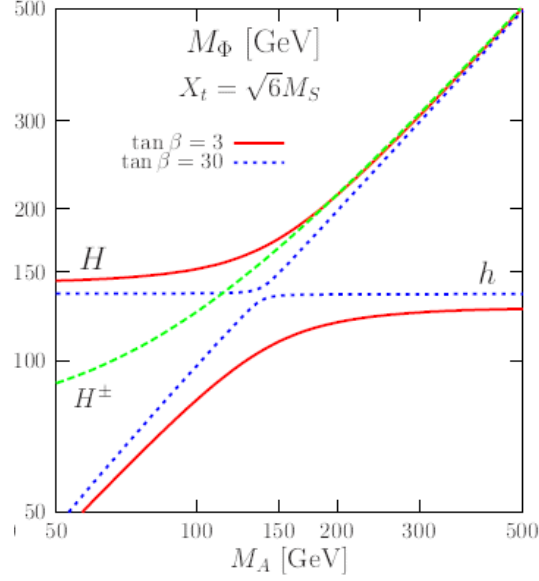


Figure 2.5: The masses of the charged and CP-even neutral Higgs bosons, as a function of mass of the CP-odd Higgs boson A . Plot from Reference [1]. The SUSY parameters have been chosen such that the quantum corrections maximize the mass of h .

in the lagrangian, which leads to only two parameters being free. These are usually taken to be m_A and $\tan \beta$; all the other parameters may be determined from these two, up to quantum corrections. In particular:

$$m_{H^\pm}^2 = m_A^2 + m_W^2, \quad (2.28)$$

and

$$m_{h,H}^2 = \frac{1}{2} \left[m_A^2 + m_Z^2 \mp \sqrt{(m_A^2 + m_Z^2)^2 - 4m_A^2 m_Z^2 \cos^2 2\beta} \right]. \quad (2.29)$$

This equation implies that one of the CP-even Higgs bosons is nearly degenerate in mass with A , while the other has a mass which is nearly independent of A . This can be seen in Figure 2.5. The value of the “cross-over” mass, (i.e. the mass of H at low m_A or the mass of h at high m_A) depends on the higher-order quantum corrections, and is usually between 115 and 135 GeV.

The couplings of the neutral Higgs bosons to various SM particles are shown in Table 2.1. From these, we can see that the decay into two W or Z bosons, which is dominant

in the SM for high Higgs masses, is suppressed for h and H and absent for A (due to CP conservation). In addition, the coupling to up-type quarks, such as the top quark, is suppressed for high values of $\tan \beta$. This means that decays into the heaviest down-type fermions, the b quark and tau lepton, will be dominant for all values of m_A .

Table 2.1: The couplings of the MSSM Higgs bosons to up-type fermions, down-type fermions, and W and Z bosons.

Φ	$g_{\Phi\bar{u}u}$	$g_{\Phi\bar{d}d}$	$g_{\Phi VV}$
h	$\cos \alpha / \sin \beta$	$-\sin \alpha / \cos \beta$	$\cos(\alpha - \beta)$
H	$\sin \alpha / \sin \beta$	$\cos \alpha / \cos \beta$	$\sin(\alpha - \beta)$
A	$\cot \beta$	$\tan \beta$	0

The branching ratios for the three neutral Higgs bosons are shown in Figure 2.6, for the value $\tan \beta = 30$. In particular, for the region where m_A and $\tan \beta$ are large, the couplings of h are very similar to the Standard Model Higgs boson. This is known as the de-coupling regime. Likewise, for small values of m_A , the couplings of H are relatively similar to the Standard Model Higgs boson. In this way, the newly-discovered particle can be easily accommodated within the framework of the MSSM.

In addition to the decay modes, the couplings also tell us about the Higgs boson production mechanisms and cross-sections. Because of the enhanced couplings to b quarks at high $\tan \beta$, b -associated production is strongly enhanced, and becomes one of the dominant mechanisms. Additionally, gluon fusion production, which proceeds through a t or b quark loop, is enhanced by the stronger b quark coupling at high $\tan \beta$. Meanwhile, vector boson fusion, ZH and WH production are suppressed. The Feynman diagrams for the dominant production mechanisms are shown in Figure 2.7.

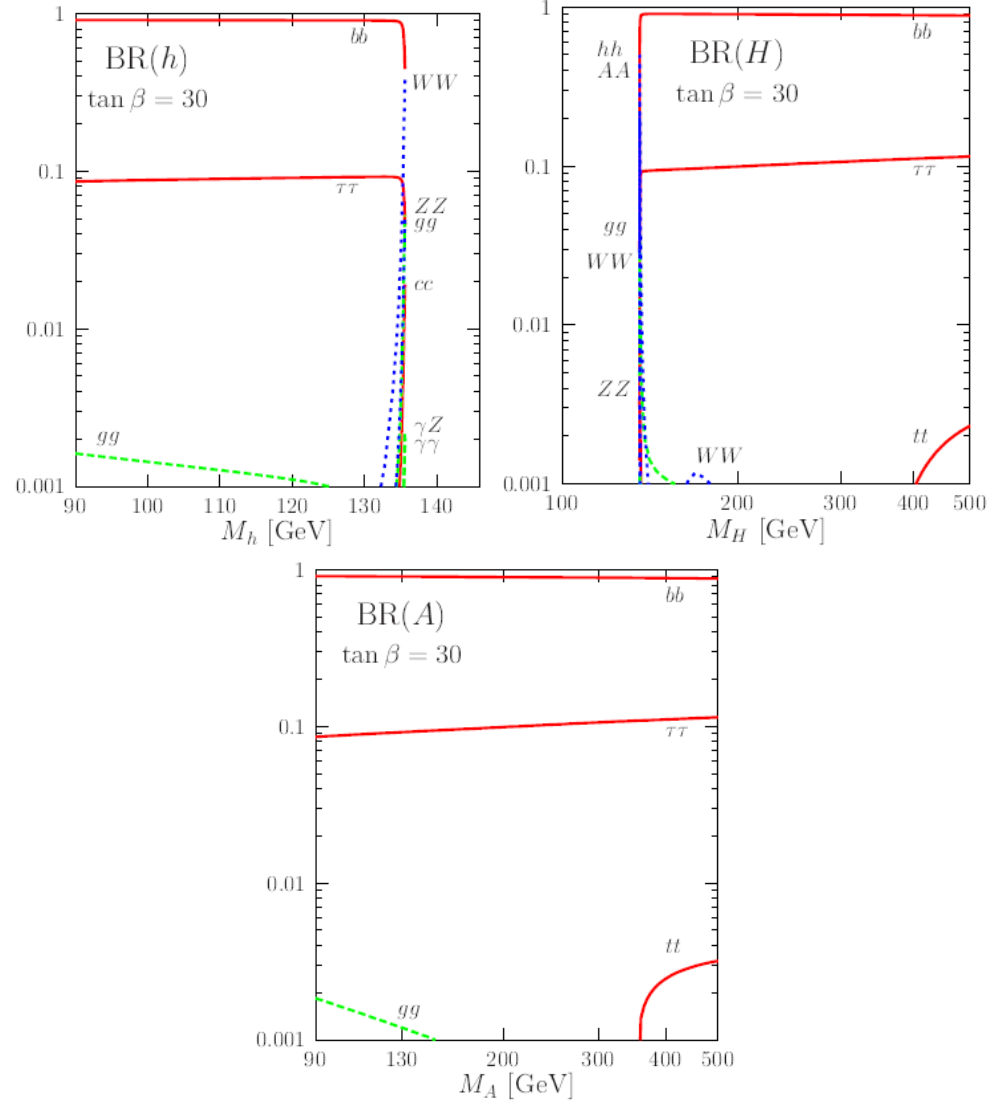


Figure 2.6: The branching ratio for h (top left), H (top right), and A (bottom), for $\tan\beta = 30$. Plots from Reference [1].

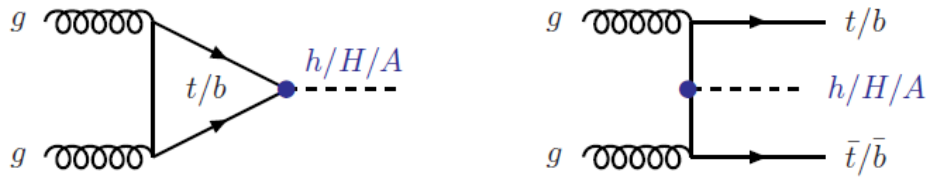


Figure 2.7: The leading-order diagrams for the dominant Higgs boson production mechanisms in the MSSM: gluon fusion (left), and b quark-associated production (right).

Chapter 3

APPARATUS

3.1 The Large Hadron Collider

The Large Hadron Collider (LHC) is the world's most powerful particle accelerator [25]. It is 27 kilometers long and located in a tunnel about 100 meters underground, near the city of Geneva, Switzerland. It is designed to accelerate protons in counter-rotating beams to energies as high as 7 TeV, with 4 TeV being the highest energy so far attained. The beams collide at four points along the ring, each of which houses one of the LHC experiments.

3.1.1 The CERN Accelerator Complex

CERN uses a succession of accelerators in order to bring protons to progressively higher energies, culminating in the LHC. The protons are collected by stripping electrons from hydrogen atoms using a duoplasmatron. These protons are formed into bunches and injected into the Linear Accelerator (LINAC), followed by the Proton Synchrotron booster. This accelerates them to an energy of 1.4 GeV, before injecting them into the Proton Synchrotron (PS), which further increases their energy to 25 GeV. From the PS the protons are injected into the Super Proton Synchrotron (SPS), where they attain an energy of 450 GeV before injection into the LHC. This sequence is illustrated in Figure 3.1.

3.1.2 The LHC

The LHC is segmented into eight sectors, each of which contains a straight section and an arc, as seen in Figure 3.2. The straight sections in sectors 1, 2, 5, and 8 contain beam crossings, which produce collisions for the ATLAS, ALICE, CMS, and LHCb experiments, respectively. Sector 4 contains Radio Frequency cavities which accelerate the beam, while sectors 3 and 7 contain beam collimation systems. Finally, sector 6 contains the beam dump, where protons are removed from the beamlines and their energy dissipated in a graphite

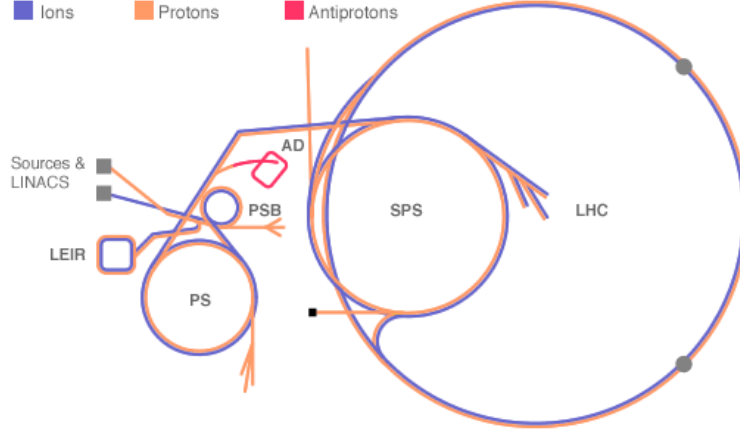


Figure 3.1: The CERN accelerator complex.

target.

The bending power in the arcs is provided by 1232 superconducting dipole magnets which create magnetic fields up to 8 Tesla. Additionally, 392 quadrupole magnets, located in the straight section, serve to focus the beam.

Because of the radio frequency power source, protons in the LHC are grouped into bunches, with up to 1.6×10^{11} protons in each bunch. The LHC is designed to collide up to 2808 bunches, with 25 ns spacing between them. However, the data used in this analysis contained a maximum of 1380 bunches, with a minimum spacing of 50 ns.

The number of events N which occur for a given process is proportional to the cross-section for the process, σ , and the integrated luminosity, \mathcal{L}_{int} :

$$N = \mathcal{L}_{int} \sigma. \quad (3.1)$$

The cross-section for the process depends on the particles being collided and the center-of-mass energy of the collision. The luminosity is a time-dependent quantity defined as

$$\mathcal{L}_{inst} = \frac{f N_1 N_2}{A}, \quad (3.2)$$

where f is the frequency of collision, N_1 and N_2 the numbers of protons being collided, and A the cross-sectional area for the collision. In parameters directly applicable to the proton

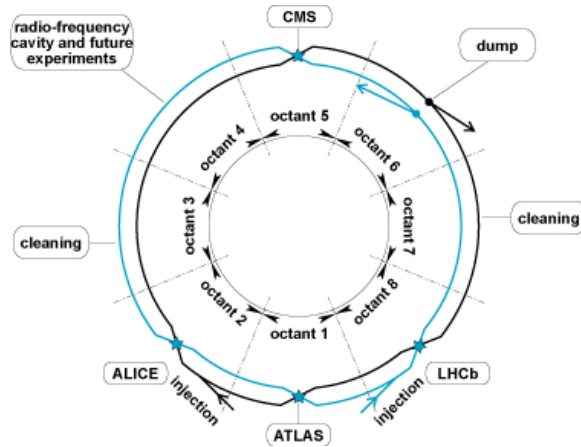


Figure 3.2: The LHC.

beams in the LHC, this can be written as:

$$\mathcal{L}_{inst} = \frac{f n_b N^2 \gamma}{4\pi \epsilon_n \beta_*}. \quad (3.3)$$

Here n_b is the number of bunches, N is the number of protons per bunch, γ is a relativistic factor, ϵ_n is the normalized transverse beam emittance (a measure of the particle divergence in the xy plane), and β_* is the beta function at the interaction point (a measure of the amplitude modulation due to the quadrupole focusing).

Because of the large number of protons in each bunch and the tight collimation, it is likely that multiple proton collisions will occur within a single bunch crossing. This phenomenon is known as pileup, or more specifically, as in-time pileup. Additionally, because the 50 ns bunch spacing is faster than the response time of some detector components, the effects from neighboring bunch crossings can be seen in event reconstruction, which is referred to as out-of-time pileup. The amount of pileup depends heavily on the instantaneous luminosity and so changes within a fill and between fills. At the highest luminosities during the 2012 run, more than 30 interactions per bunch crossing occurred; while during more typical conditions, about 15 interactions could be expected.

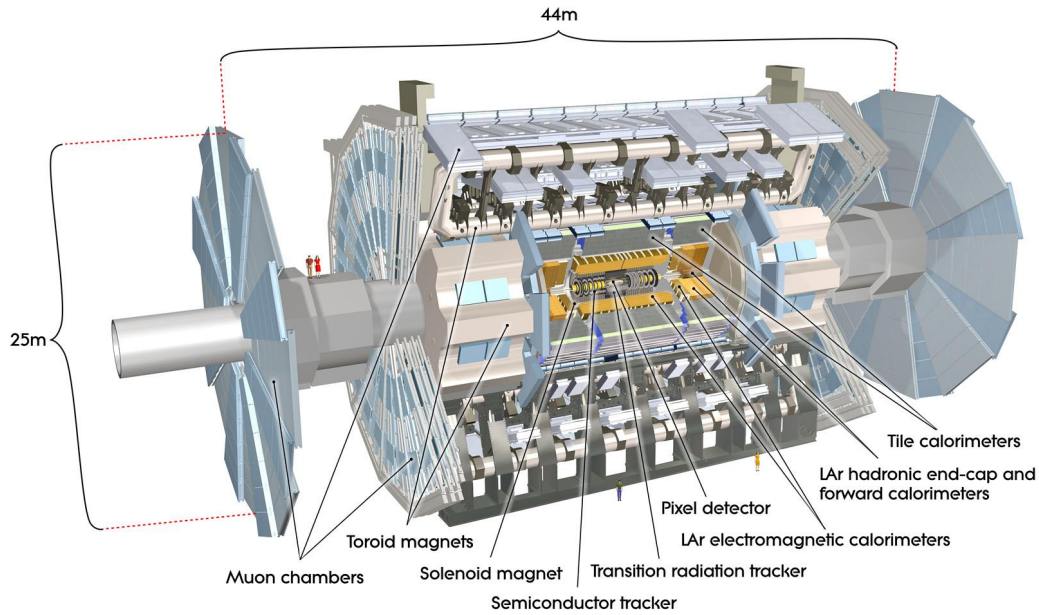


Figure 3.3: The ATLAS detector.

3.2 ATLAS

ATLAS [26] is a multi-purpose detector designed to be able to measure a wide range of physics processes in the challenging conditions provided by the LHC. Like other modern particle physics detectors, ATLAS is built in layers: An inner tracking detector to measure the direction and momentum of charged particles, a calorimeter to measure the energy of charged and neutral particles, and a muon spectrometer to identify the particles which can escape the calorimeter. A 2 T solenoidal magnet lies between the inner detector and calorimeter, while three toroidal magnets provide an average magnetic field of 0.5 T in the area of the muon spectrometer.

ATLAS uses a right-handed coordinate system, with the z -axis pointing along the beam line, the x -axis pointing to the center of the ring, and the y -axis pointing towards the sky. The polar and azimuthal angles are denoted as θ and ϕ , respectively. The polar angle is

usually replaced by the pseudorapidity η , defined as:

$$\eta = -\ln \left(\tan \left(\frac{\theta}{2} \right) \right). \quad (3.4)$$

The pseudorapidity approximates the true rapidity y , defined as

$$y = \frac{1}{2} \ln \left(\frac{E + p}{E - p} \right), \quad (3.5)$$

which is invariant under boosts in the z direction. The approximation is valid when a particle's mass is much less than its energy, and becomes exact for massless particles. The “distance” between two particles is commonly measured using ΔR , which is defined as

$$\Delta R = \sqrt{\Delta\eta^2 + \Delta\phi^2}. \quad (3.6)$$

Because of the data storage and bandwidth limitations, ATLAS can only store a small fraction of the 20,000 events which occur each second. In order to ensure that the most interesting events get recorded, a multi-level trigger system is used to reduce the readout to a manageable rate.

3.2.1 The Inner Detector

The Inner Detector (ID) extends 3.5 m in z and 1.2 m in R , and covers the pseudorapidity region $|\eta| < 2.5$. It is composed of three subsystems: the pixel detector, the semi-conductor tracker (SCT), and the transition radiation tracker (TRT). The purpose of the ID is to reconstruct tracks left by charged particles, to measure the momentum of these tracks and to combine the tracks into vertices corresponding to different proton interactions or to displaced particle decays. The layout of the ID is illustrated in Figures 3.4 and 3.5.

The pixel detector has very high granularity and lies at the innermost place in the detector. It consists of a barrel component with three concentric layers, and three endcap disks on either end. The detecting elements are pixel sensors with a minimum size of $50 \times 400 \mu\text{m}$ ($\phi \times z$). The resolutions in the barrel region is approximately $\sigma_R = 10 \mu\text{m}$, $\sigma_z = 115 \mu\text{m}$, while for the endcaps they are $\sigma_\phi = 10 \mu\text{m}$, $\sigma_R = 115 \mu\text{m}$.

Surrounding the pixel detector is the semi-conductor tracker, which is based on silicon microstrip technology. It consists of four layers in the barrel and nine disks in each endcap.

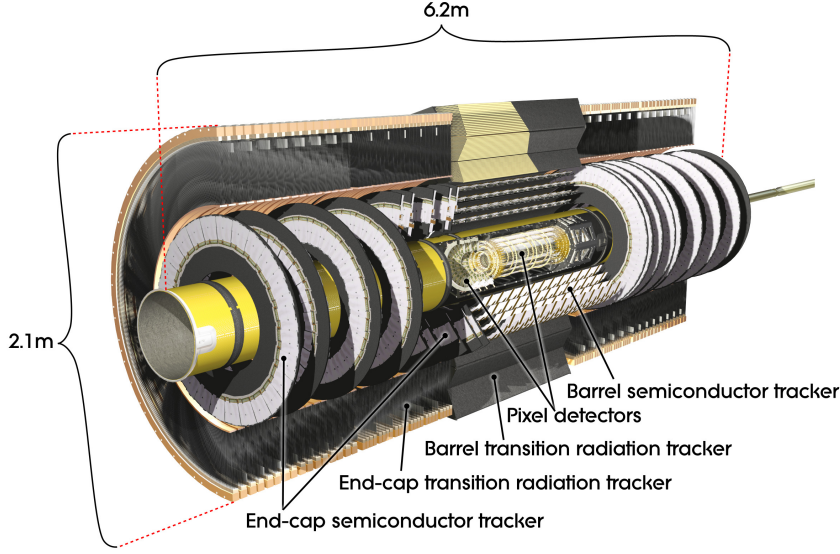


Figure 3.4: The ATLAS Inner Detector.

In the barrel there are two strips for each layer, one aligned along the z axis and one aligned at a 40 mrad offset; similarly, in the endcaps the first layer is aligned radially while the second is offset by 40 mrad. This setup allows for at least four measurements in R , ϕ , and z for a typical charged particle. The resolution is approximately $\sigma_\phi = 17 \mu\text{m}$, and $\sigma_{Rz} = 580 \mu\text{m}$.

The outermost layer of the ID is the transition radiation tracker. It consists of straw tubes 4 mm in diameter, which are filled with a Xe-based gas mixture, and have a central high-voltage wire for collecting ionizing electrons. The TRT contains 73 straw layers in the barrel and 160 planes in the endcap. Because of the length of the tubes (71 cm in the barrel and 37 in the endcap), only two coordinates may be measured with any accuracy: (R, ϕ) in the barrel and (z, ϕ) in the endcap. Additionally, foils are interleaved with the straw tubes, which causes low-mass particles to produce transition radiation. The transition radiation is collected by the straws and results in an electrical pulse with a greater charge. This information can be used for particle identification, in particular to distinguish electrons from pions or other heavier hadrons.

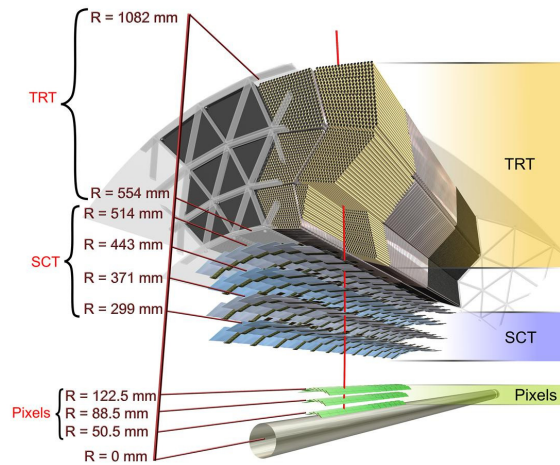


Figure 3.5: A view of the barrel portion of the ATLAS Inner detector.

3.2.2 The Calorimeter

The ATLAS calorimeter consists of an electromagnetic and a hadronic component. It provides energy measurements of charged and neutral particles with nearly full hermetic coverage in the pseudorapidity range $|\eta| < 4.5$. The layout of the different components is shown in Figure 3.6.

The electromagnetic calorimeter (ECAL) is a lead-liquid-Argon (LAr) sampling calorimeter based on an accordion geometry (see Figure 3.7). It is divided into a barrel, covering $|\eta| < 1.475$, and two endcaps covering $1.375 < |\eta| < 3.2$. In the region $|\eta| < 2.5$, corresponding to the ID coverage, there are three layers including a very finely segmented first layer. This allows for precise position measurements and for directional pointing, even for photons with no ID track. Outside of $|\eta| < 2.5$, there are two layers providing a coarser granularity. The ECAL has a typical depth between 22 and 33 radiation lengths for electrons and photons, and an average energy resolution $\sigma_E/E = 10\%/\sqrt{E[\text{GeV}]}$. There is additionally a thin presampler layer of liquid Argon just before the first ECAL layer, which aids in correcting for energy losses in material prior to the calorimeter.

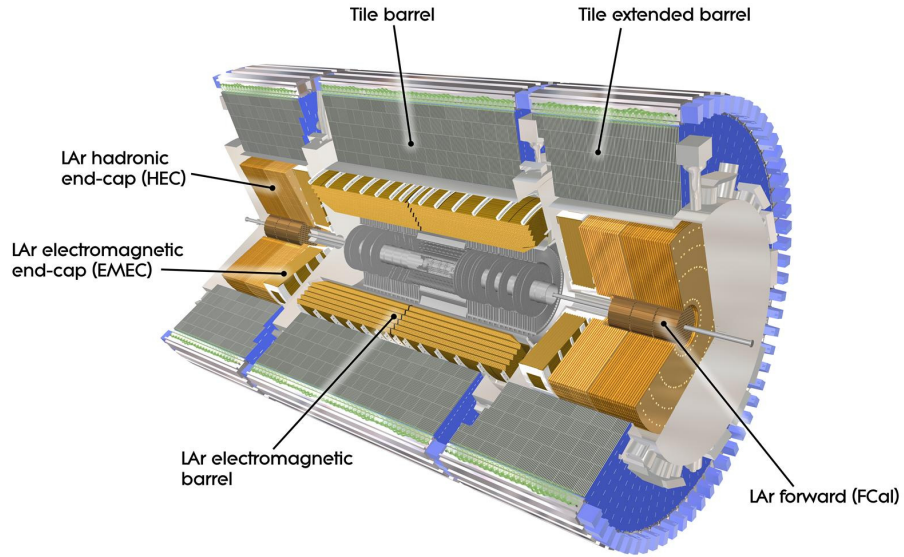


Figure 3.6: The ATLAS calorimeters.

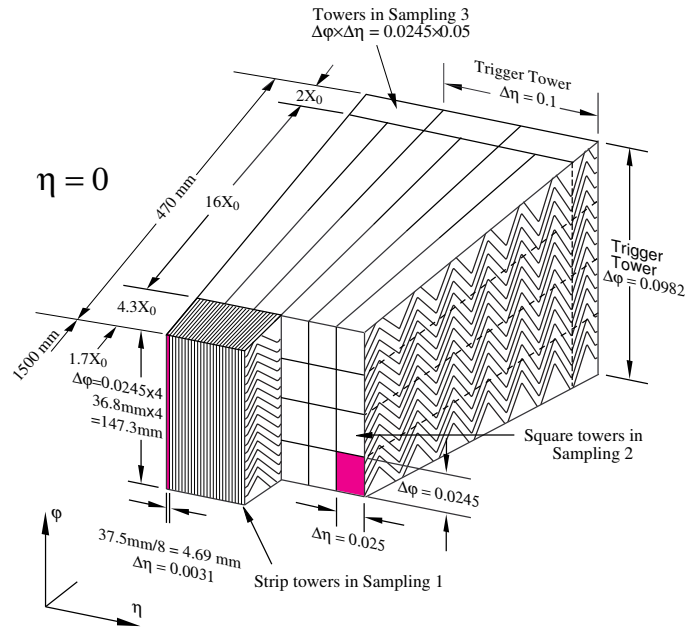


Figure 3.7: Detail of electromagnetic calorimeter module, indicating the granularity in each of the three layers.

In the barrel region, covering $|\eta| < 1.7$, the hadronic calorimeter uses scintillating plastic tiles as the active material, interleaved with a steel absorber. In the endcap regions, which extend from $|\eta| = 1.5$ to $|\eta| = 3.2$, LAr is the active material and copper plates serve as the absorber. The HCAL has a typical depth of about 11 interaction lengths when combined with the ECAL, and has an average energy resolution $\sigma_E/E = 50\%/\sqrt{E[\text{GeV}]}$.

The forward calorimeter extends the pseudorapidity coverage to $|\eta| < 4.9$. It consists of three layers, each of which uses LAr as the sensitive medium. The first layer uses copper as the absorber, and is optimized for electromagnetic measurements, while the second and third layers use a tungsten absorber, and are designed for hadronic energy measurements. The average depth is between 7 and 9 interaction lengths, and the average energy resolution $\sigma_E/E = 100\%/\sqrt{E[\text{GeV}]}$.

3.2.3 The Muon Spectrometer

As minimally ionizing particles, muons are usually capable of traversing the ID and calorimeters without losing much of their energy. The muon spectrometer (MS) is designed to provide precision measurements and triggering capability for these or other charged particles which may escape the calorimeter. The MS is divided into barrel and endcap sections, separated at $|\eta| = 1.05$, and contains three layers. The MS uses four technologies: Monitored Drift Tubes (MDT's) and Cathode Strip Chambers (CSC's) for precision measurements and Resistive Plate Chambers (RPC's) and Thin Gap Chambers (TGC's) for triggering. The layout is shown in Figures 3.8 and 3.9.

The MDT's provide precision coverage throughout the MS, except for the innermost layer of the endcaps in the range $|\eta| > 2.0$ (where the rate is very high). Each drift tube contains a pressurized Ar-CO₂ gas mixture and a central anode wire at 3080 V. Charged particles traversing a tube cause ionization in the gas, leading to an avalanche of particles collected by the anode wire. The distance of closest approach of the muon to the wire can be measured with a precision of approximately 10 microns. An MDT chamber consists of 6 or 8 layers of tubes, arranged in two multi-layers, so that segments may be formed by comparing drift times in neighboring tubes. Because of the toroidal magnetic field, the MDT chambers

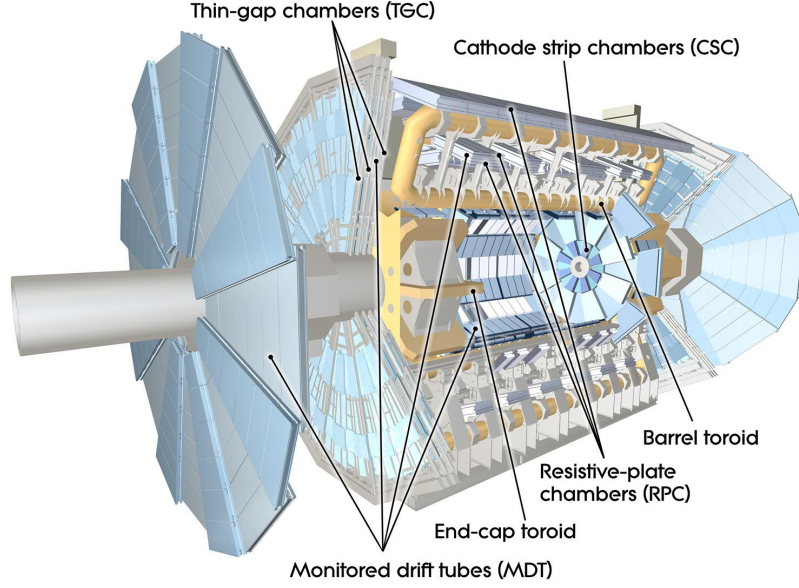


Figure 3.8: The ATLAS Muon Spectrometer.

are arranged to provide precise measurements of η (where the bending occurs), while the ϕ coordinate is measured by the trigger chamber.

The CSC's are multi-wire proportional chambers fitted with cathode strips, which detect the effects of ions repelled by the anode wires after a muon passes. The anode wires are arranged radially outward, while the cathode strips may be either parallel or perpendicular to the wires, to allow both η and ϕ measurements. Each CSC chamber is composed of four planes yielding four measurements per track. The resolution is approximately 40 microns in R and 5 mm in ϕ .

The RPC's provide the muon trigger in the barrel of the MS. They are gaseous parallel plate detectors without wires. Each RPC chamber contains two gas-gap layers of 2 mm each, with an electric field of 4.9 kV/mm in the gap. The signals are read out via metallic strips on either side of the gas gap. There are three layers of RPC chambers; the first two are located on either side of the middle MDT layer, while the outer layer is located on the outermost MDT layer.

The TGC's provide triggering capabilities in the endcap region of the MS. They consist

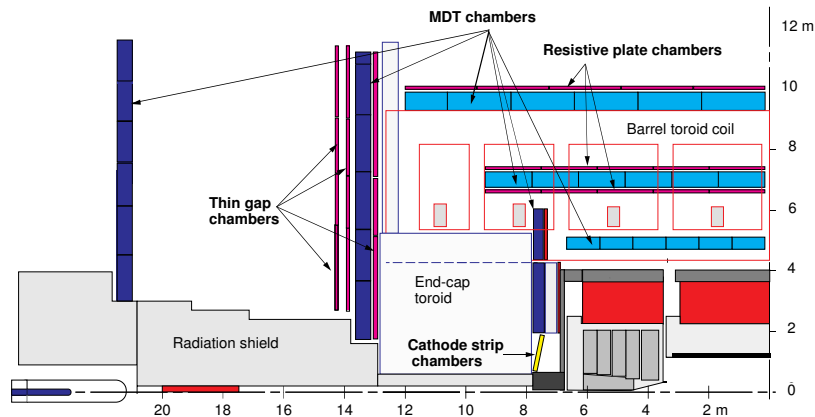


Figure 3.9: Schematic layout of one quadrant of the ATLAS Muon Spectrometer.

of a gas volume with a plane of wires held at 2900 V, and two cathodes. The wires are arranged to measure the η coordinate while the cathode strips measure the ϕ coordinate. There are four layers of TGC's, the first of which is located inside the first MDT/CSC layer, while the other three surround the middle MDT chambers.

3.2.4 The Trigger System

With events occurring every 50 ns, and requiring about 1.5 MB to store and 20 sec of CPU time to reconstruct, recording all of the collisions in ATLAS would clearly not be feasible. However, the cross-section for most physics processes is quite small compared to the total pp cross-section, and most of the events contain elastic collisions or other well-understood processes. In order to reduce the rate to a manageable level, while maintaining efficiency for interesting physics processes, ATLAS employs a three-tiered trigger system.

The first trigger level, L1, is based on hardware and uses information from the calorimeters and muon sub-detectors. It locates potentially interesting high- p_T objects within regions of interest (ROI's) in η and ϕ . These are passed to the Central Trigger Processor (CTP), along with information about the type of object and its p_T , which returns a decision based on a pre-set trigger menu. Events are accepted by the CTP at a rate of approximately 75 kHz.

The ROI's for events passing L1 are fed to the next trigger level, L2. L2 is software-

based, and has access to the full detector granularity only in the area around the ROI's. It reduces the rate to approximately 5kHz.

Events which pass L2 are processed by the final trigger level, known as Event Filter (EF). The EF performs a simplified version of the full event reconstruction. Events which pass the EF are scheduled to be reconstructed offline. In the 2012 run the EF output rate was about 1 kHz, which is limited by the data storage capabilities of ATLAS. However, the CPU time for event reconstruction was a tighter bottleneck, so that only 650 Hz was scheduled for immediate processing. The remaining events were stored in a raw format and reconstructed during the LHC shutdown; these are not used in this thesis.

Chapter 4

SAMPLES

4.1 *Data Sample*

The data used in this analysis was recorded with the ATLAS detector during 2012, using proton-proton collisions from the LHC at a center-of-mass energy of 8 TeV. A total integrated luminosity of 23.3 fb^{-1} was delivered by the LHC in this period. However, the analysis considers only data for which the full ATLAS detector was on and operational. This leads to a final integrated luminosity of $20.3 \pm 0.6 \text{ fb}^{-1}$.

4.2 *Monte Carlo Simulated Samples*

In order to search for the MSSM Higgs bosons, we must compare the observed data to the expectations from the background-only and background + signal hypotheses. To determine these expectations, it is necessary to simulate the various physics processes that occur during proton collisions, and how they appear in the detector.

4.2.1 *Event Generation*

Monte Carlo event generation of physics processes consists of two parts: the Matrix Element (ME), which simulates the effects of the primary parton collision, and the Parton Shower (PS), which simulates the subsequent hadronization of the resulting bare quarks and gluons.

As explained in Section 2, the two relevant signal production processes which we consider are gluon fusion and b -associated production. The first process is generated POWHEG [27], a next-to-leading-order (NLO) event generator, for the ME, and PYTHIA [28] for the PS. b -associated production is modelled using SHERPA [29] for both the ME and PS. Only a CP-even Higgs boson has been simulated, at 19 mass points between 90 and 800 GeV. For a given signal hypothesis, each of the three neutral Higgs bosons is modelled by choosing

the mass point closest to the theoretical prediction and scaling to the theoretical cross-section [30] [31], and the contributions of all three are added.

W and Z bosons form a large background for the analysis. These are modelled using the leading-order ALPGEN [32] event generator, interfaced with PYTHIA for the parton shower, using the MLM scheme [33] to match between the two. The $t\bar{t}$ process is simulated using POWHEG, with PYTHIA for the PS. Single top production was modelled with Ac-erMC [34], interfaced to HERWIG [35] for the PS. For the diboson WZ and ZZ samples, MC@NLO with HERWIG was used, while WW was modelled with ALPGEN and HERWIG.

For all of the samples, other than the Higgs production with SHERPA, the tau lepton decay is not modelled directly by the generator but instead handled by the specialized TAUOLA [36] generator. Additionally, photon radiation from charged leptons in the final state is modelled with PHOTOS [37] in the leading-log approximation.

4.2.2 Detector Simulation

After the event generator produces the set of final-state particles, together with their four-momenta, these are then passed through a simulation of the ATLAS detector [38] built with the GEANT4 [39] program, to model the interaction of the particles with the material of the detector. This is done in a series of discrete steps. At each step, a particle has a specified chance to decay or to undergo a material interaction, and afterward the four-momentum of each particle is re-computed. More than 10^7 steps are performed in the simulation of an event, with the majority occurring in the calorimeter.

After the detector simulation, the energy deposits from the particles are translated into hits in the detector through the process of digitization. At this point, the full event reconstruction is applied to the simulated and digitized events, using identical algorithms to the ones used for real data.

The bulk of the event generation was done before the data were collected, and hence before the exact pileup conditions in data were known. For this reason, events were simulated with a wide range of values for the average number of proton interactions per event. Simulated events are then re-weighted so that the pileup distributions match between data

and Monte Carlo.

Chapter 5

RECONSTRUCTION

The MSSM Higgs search makes use of electrons, muons, jets, b-tagging, τ leptons, and missing energy in order to identify events. This chapter summarizes how these high-level physics objects are reconstructed by combining information from the various sub-detectors. The basic particle signatures in the detector are illustrated in Figure 5.1.

5.1 Track reconstruction

Track reconstruction in ATLAS is performed using two algorithms: an “inside-out” and an “outside-in” approach [40]. The inside-out algorithm is run first, and begins by converting the raw detector hits into three-dimensional space-time points. Seeds are then formed from these points using the pixel and the first layers of the SCT. The seeds are subsequently extended to the end of the ID and hits along the path are associated with the track using a Kalman filter [41]. The tracks are then re-fit using all associated hits, and quality criteria are applied to get rid of fake tracks or choose between overlapping ones.

The outside-in approach is performed after the inside-out. Segments are formed from hits in the TRT, excluding hits already assigned to tracks from the first algorithm. These are then extrapolated back to the interaction point, and hits in the SCT or pixel detectors are associated to the track, after applying quality criteria. The track is then re-fit using all of the associated hits.

5.2 Vertexing

In order to be considered for vertex reconstruction, tracks must satisfy the following quality criteria [42]:

- $p_T > 500$ MeV

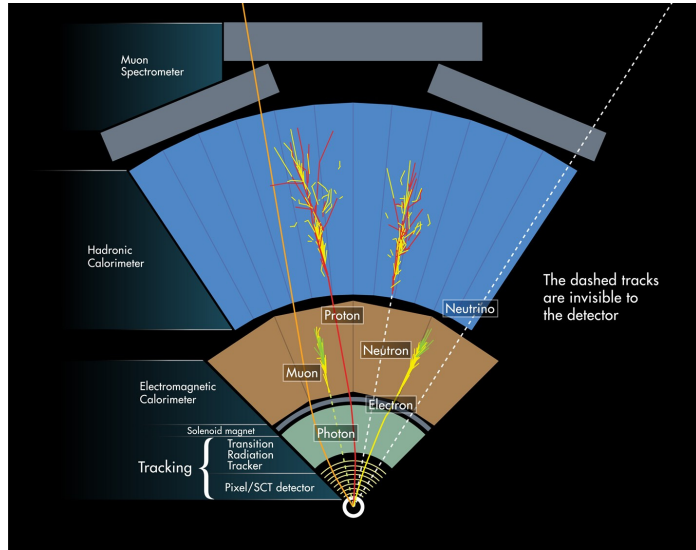


Figure 5.1: An illustration of the interactions of several types of particles within the ATLAS detector.

- $|d_0| < 4 \text{ mm}$
- $\sigma(d_0) < 5 \text{ mm}$
- $\sigma(z_0) < 10 \text{ mm}$
- at least 2 hits in the pixel detector
- at least 4 hits in the SCT

where d_0 and z_0 are the transverse and longitudinal impact parameters measured with respect to the center of the luminous region, and σ the associated uncertainties.

Vertices are then formed from the tracks with an adaptive fitting algorithm, which uses an iterative χ^2 minimization routine [40]. The process is repeated until all tracks are associated with vertices, or until it is not possible to form a vertex with a lower χ^2 . Of the vertices thus constructed, the primary vertex is chosen as the one with the highest sum p_T^2 of the associated tracks.

5.3 Muons

Muon reconstruction [40] begins with information only from the muon spectrometer. Straight-line segments are formed from multiple hits within a given MDT or CSC chamber, and are required to point towards the primary vertex. When possible, ϕ information is provided by the nearby trigger chamber. Segments from two or more stations are then combined to create *stand-alone* muon tracks. The muon track parameters are extrapolated to the primary vertex accounting for energy loss in the calorimeter (usually a few GeV).

At this point, an attempt is made to match tracks between the inner detector and muon spectrometer. If a match is found with a suitably small χ^2 , the result is a *combined* muon. The coordinates of the combined muon are derived from a statistical combination of the ID and MS tracks. Finally, an attempt is made to geometrically match ID tracks to segments in the MS which had not formed tracks. Where a match is found, the result is a *segment-tagged* muon. To select events with muons in the final state, only combined muons are considered; however segment-tagged or stand-alone muons are used for resolving ambiguity between overlapping objects.

In order to reject muons from decaying hadrons, candidates are required to be isolated from nearby activity in the detector. The sum of all calorimeter deposits within a cone of $\Delta R < 0.2$ around the muon's track (excluding the energy deposited by the muon itself) must have a transverse energy less than 6% of the muon's transverse momentum. Additionally, the sum of the transverse momenta of all tracks within a cone of $\Delta R < 0.4$ around the muon's track must be less than 6% of the muon's transverse momentum. For calculating this variable, only tracks associated with the same vertex as the muon are considered. The value of 6% was optimized to maximize rejection of muons from hadron decays, while maintaining high efficiency for muons in signal events.

5.4 Electrons

Electrons are reconstructed in the pseudorapidity range $|\eta| < 1.37$ or $1.52 < |\eta| < 2.47$, with the gap corresponding to the crack region between the barrel and endcaps of the electromagnetic calorimeter. Two-dimensional clusters are reconstructed using a sliding

window in the second layer of the ECAL [43]. A track in the ID is required to match the cluster within 0.01 in η [44]. The energy of the electron candidate is taken from the calorimeter deposit while the direction is taken from the associated track.

At this point, quality criteria are applied to the electron candidate to reject charged hadrons or converted photons which can pass the reconstruction. These include requirements on the energy leakage into the hadronic calorimeter, the shape of the cluster, the quality of the track, and the match between the track and the cluster. Three levels of tightness are defined. To select events with electrons in the final state, only the tightest identification is used, but as with muons, the looser criteria are used for resolving overlapping objects.

The same isolation criteria which are applied to muons are used for electrons as well.

5.5 Jets

A jet in high energy physics refers to the collimated collection of particles which result from the hadronization of high-energy quarks or gluons. Jet reconstruction in ATLAS begins by forming topological clusters in the calorimeter [45]. The clustering algorithm looks for cells with energy at least 4σ above the electronic noise threshold. Neighboring cells with energies at least 2σ above the noise threshold are added iteratively to the cluster, and in the final step all neighboring cells are added.

The calorimeter produces a different response for electromagnetic particles (electrons or photons) and for hadrons, even if they had the same initial energy. One must therefore decide whether to measure calorimeter deposits at the electromagnetic energy scale, or the jet energy scale (JES). Initially, all deposits are treated as electromagnetic, as the calorimeter was calibrated using electromagnetic particles. Prior to being formed into jets, the topological clusters are scaled to the JES [46] [47], to be consistent with originating from hadrons.

Once the topo-clusters have been formed, they are combined into jets using the anti- k_t algorithm [48]. This algorithm defines a “distance” d_{ij} between two clusters i and j as

follows:

$$d_{ij} = \min(k_{ti}^{-2}, k_{tj}^{-2}) \frac{\Delta_{ij}^2}{R^2}, \quad (5.1)$$

where k_t is the transverse momentum of the cluster, Δ_{ij} is the distance between the two clusters (ΔR), and R is the distance parameter of the algorithm, which for ATLAS is set to 0.4. Jets are then formed according to the following procedure:

- For a given cluster i , if $k_{ti}^{-2} < \min_j \{d_{ij}\}$, then i is declared a jet and removed from the list of clusters.
- If $k_{ti}^{-2} > \min_j \{d_{ij}\}$, then the cluster j which minimizes d_{ij} is added to i to form a single cluster.
- The process repeats until all clusters have been formed into jets.

The anti- k_t algorithm is used because it is well-behaved at low energies, and avoids collinear splitting.

To reject jets from pileup interactions, the Jet Vertex Fraction (JVF) is calculated. It is defined as the transverse momentum of the tracks within the jet which are associated with the primary vertex, divided by the total transverse momentum of all tracks within the jet. A cut of $\text{JVF} > 0.5$ is applied to jets within the acceptance of the tracker. Additionally, cleaning requirements [49] are applied to the jet to reduce non-physics backgrounds, such as noise bursts.

5.6 *b*-tagging

Due to the relatively heavy mass of b mesons, hadrons containing b -quarks may travel a macroscopic distance before decaying to lighter hadrons. This fact can be exploited to “ b -tag” certain jets as originating from a b -quark. In particular, for these jets a secondary vertex can be formed, the b -hadron decay chain can be reconstructed, and the associated tracks will frequently have large impact parameters with respect to the beam line. These three pieces of information are combined into a discriminator using an Artificial Neural Network [50]. The efficiency of the discriminator depends heavily on the p_T of the b -jet,

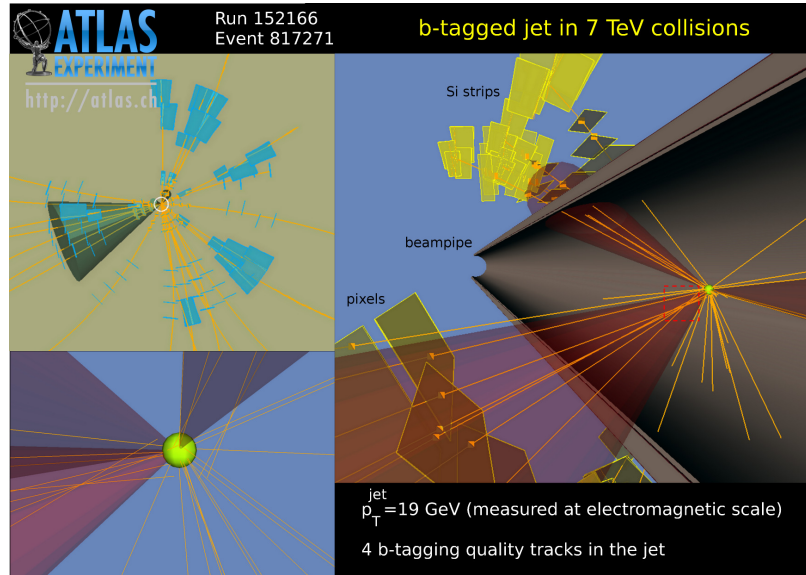


Figure 5.2: Event display including a b-tagged jet in the ATLAS detector. The secondary vertex and large impact parameters of the associated tracks are clearly visible.

and is about 40% for the b-associated Higgs production considered in this analysis. The efficiency is a few percent for charm quark-initiated jets, and below 1% for jets initiated by light quarks or gluons.

5.7 Tau leptons

Tau leptons decay 35.2% of the time to an electron or muon, plus two neutrinos. In this case the lepton is indistinguishable from those produced in any other process, and they will be reconstructed by the algorithms described above. In the remaining cases, the tau decays hadronically, usually to one or three charged pions (or sometimes kaons), plus zero, one or two neutral hadrons. Identifying these decays is the goal of tau identification.

The mass of the tau lepton is 1.776 GeV [2]. Because this is much less than the energies of taus we consider (which must be at least 20 GeV), the decay products are likely to be very tightly collimated. Along with low track multiplicity, this is the basic information used to distinguish taus from quark or gluon-initiated jets. Additionally, the proper lifetime of the tau is 0.2906 ps, corresponding to a distance of 87.11 μm . Although this is less than for

Table 5.1: Selected branching ratios for tau leptons [2].

Decay mode	Branching Ratio
All leptonic	35.2
$e\nu_\tau\bar{\nu}_e$	17.8
$\mu\nu_\tau\bar{\nu}_\mu$	17.4
All 1-prong hadronic	49.1
$\pi^-\nu_\tau$	10.8
$\pi^-\pi^0\nu_\tau$	25.5
$\pi^-\pi^0\pi^0\nu_\tau$	9.5
All 3-prong hadronic	15.2
$\pi^-\pi^-\pi^+\nu_\tau$	9.3
$\pi^-\pi^-\pi^+\pi^0\nu_\tau$	4.6

b-jets, it can sometimes provide discriminating power.

5.7.1 Tau reconstruction

Hadronic taus are reconstructed in the same manner as jets, i.e. by running the anti- k_t algorithm on topological calorimeter clusters. The seed jets are required to be within the acceptance of the tracking detector ($|\eta| < 2.5$) [51]. To account for the different calorimeter responses to hadronic taus, the energy of the jet is re-scaled to the tau energy scale (TES), which is derived from Monte Carlo simulation [52]. The rescaling depends on the transverse momentum, pseudorapidity, and number of tracks of the tau. The uncertainty on this procedure is estimated using a combination of Monte Carlo, test-beam data, and data from dedicated low-luminosity LHC runs [52].

Tracks are associated with the tau candidate if they lie within $\Delta R < 0.2$ from the seed jet axis. Additionally, the p_T must be above 1 GeV, and the transverse and longitudinal impact parameters must be within 1.0 and 1.5 mm, respectively. The impact parameters are calculated with respect to the vertex which maximizes the JVF for the tau in question.

Tracks in the annulus $0.2 < \Delta R < 0.4$ are used in calculating discriminating variables but not in classifying the taus as either 1 or 3-prong.

The number of neutral pions within a tau is calculated using the Boosted Decision Tree (BDT) method [53]. Variables are defined based on the number of clusters within the tau candidate, the matching between these clusters and the tracks, and the energy profile of the clusters in the calorimeter.

5.7.2 Distinguishing taus from quark and gluon jets

Rejection of jets from quarks and gluons is achieved using a Boosted Decision Tree [53]. The following variables are used:

•

$$f_{track} = \frac{p_T^{leadtrack}}{\Sigma E_T^{EM}(cells)}. \quad (5.2)$$

The sum in the denominator refers to the transverse energy, calibrated at electromagnetic scale, of all cells associated to the tau candidate within $\Delta R < 0.2$. The variable is corrected to account for the presence of pileup.

•

$$f_{core}^{corr} = \frac{\Sigma^{\Delta R < 0.1} E_T^{EM}}{\Sigma^{\Delta R < 0.2} E_T^{EM}} \quad (5.3)$$

The sums run over all cells associated to the tau candidate. The variable is corrected to account for the presence of pileup.

•

$$R_{track} = \frac{\Sigma_i p_{T,i} \Delta R_i}{\Sigma_i p_{T,i}} \quad (5.4)$$

The sum runs over all tracks within $\Delta R < 0.4$ from the tau axis.

- N_{iso}^{trk} : the number of tracks in the isolation annulus $0.2 < \Delta R < 0.4$. Used for 1-prong taus only.
- m_{tracks} : the invariant mass of the track system. Used for 3-prong taus only.

- ΔR_{max} : the maximum distance of track from the tau axis. Used for 3-prong taus only.
- S_{trk}^{IP} : impact parameter significance of the track. Used for 1-prong taus only.
- S_T^{flight} : transverse distance significance of the secondary vertex. Used for 3-prong taus only.
- N_{π^0} : the number of reconstructed neutral pions.

•

$$f_{\pi^0} = \frac{\Sigma p_T(\pi^0)}{p_T} \quad (5.5)$$

The fraction of the tau's transverse momentum carried by the associated π^0 's.

- m_{trk,π^0} : the invariant mass of the tracks and π^0 's associated to the tau.

The BDT's are trained separately for 1 and 3-prong taus. The cuts are chosen to achieve a constant signal efficiency in p_T , which is 60% for this analysis. The efficiency for QCD jets varies with p_T , and is usually a few percent for 1-prong, and less than 1% for 3-prong.

5.7.3 Distinguishing taus from electrons and muons

Electrons are very likely to pass tau reconstruction, since they consist of a single track and an associated cluster. By performing a geometric overlap removal with identified electrons, most of these can be rejected. However, the number of electrons which fail electron identification is non-negligible, and the rate at which they pass tau ID is large enough that a dedicated veto is still necessary. This is achieved using a BDT. Input variables include the fraction of high-threshold TRT hits, the fraction of the energy left in the electromagnetic calorimeter (f_{EM}), the match between the track momentum and calorimeter energy (at electromagnetic scale), and cluster shape variables which are sensitive to the difference between electrons and pions. For an efficiency of 85% for identified taus, more than 99% of electron fakes can be rejected.

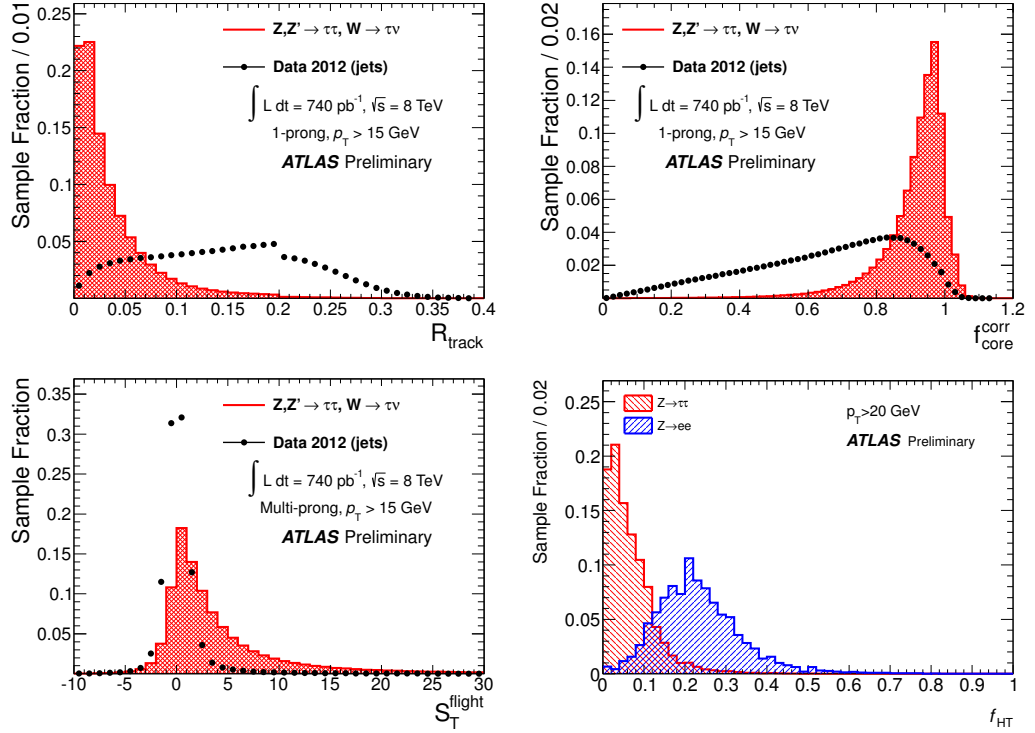


Figure 5.3: Some variables used to distinguish hadronic taus from jets or from electrons. Upper left: R_{track} , the p_T -weighted average track distance from the jet center. Upper right: f_{core}^{corr} , the pileup-corrected fraction of the tau's energy within the core cone of $\Delta R < 0.1$. Lower left: S_T^{flight} , the transverse distance significance of the secondary vertex. Lower right: The fraction of high-threshold TRT hits for the leading track.

Because muons are minimally ionizing particles, they seldom deposit enough energy in the calorimeter to be reconstructed as taus. However, significant bremsstrahlung is possible, and the muon may also radiate a photon before the calorimeter or otherwise overlap coincidentally with a calorimeter deposit. Again, the most effective means of reducing this background is through overlap removal with reconstructed muons; however, because the muons have frequently lost more energy than expected, the usual reconstruction may fail, and a dedicated veto is applied. First, reconstructed tau candidates are classified according to f_{EM} : for muons which are losing energy themselves the value is very low, while for muons where the calorimeter energy comes from other sources the value is very high (tau candidates with intermediate f_{EM} automatically pass the veto). Next, the candidates are classified by detector region; in regions where there is poor muon spectrometer coverage, overlap removal is less effective and a tighter cut is applied. Finally, for each classification, a cut is made on f_{track} . The variable is frequently anomalously high for muons if it has not deposited all of its energy in the calorimeter. An efficiency greater than 96% is obtained for true taus, while about half of the muon fakes are removed with this method. Figure 5.4 shows the variables used for muon rejection.

5.8 Missing transverse energy

Neutrinos (as well as some hypothetical particles) interact only via the weak interaction, and are therefore able to escape the detector without leaving any signature. However, their presence can frequently be inferred using the conservation of momentum. This is not possible generally, because it is not known what fraction of the proton's momentum each interacting parton had, and so an unknown amount of momentum could be left with the other proton constituents and escape down the beam pipe. However, the total momentum in the plane transverse to the beam should be zero initially, so that significant missing transverse energy (E_T^{miss}) is a clear indication for neutrinos.

The E_T^{miss} is calculated by considering each reconstructed object in an event (muons, electrons, photons, hadronic taus, and jets), each calibrated to its energy scale [54]. Additionally, calorimeter deposits which are not associated to an high- p_T object are included, calibrated at the electromagnetic scale. This introduces a sensitivity to the amount of

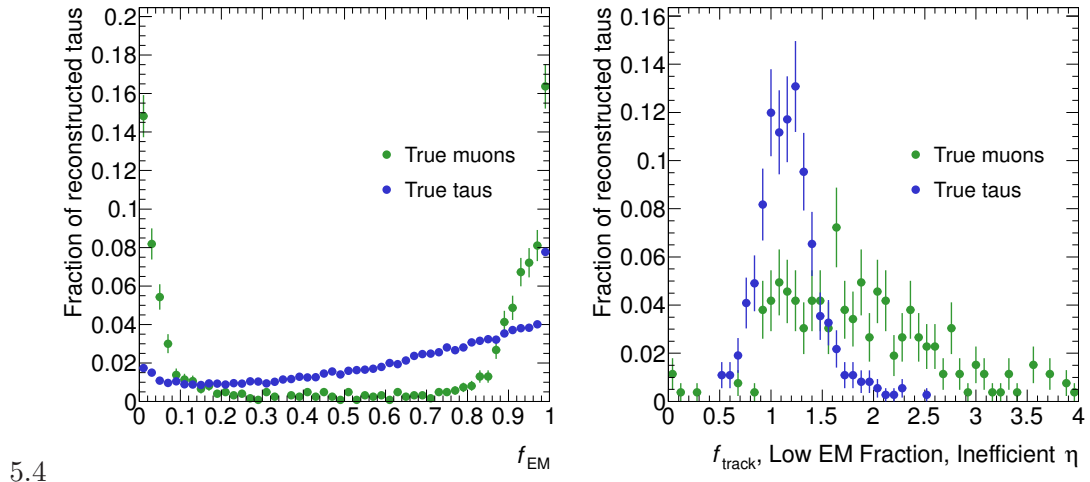


Figure 5.4: Variables used to reject muons faking taus. Left: f_{EM} , the electromagnetic fraction of the tau candidate’s calorimeter energy. The two populations for muons correspond to the cases where the muon itself does or does not deposit energy in the calorimeter. Right: The ratio of the ID track p_T to the calorimeter energy. Shown for the category with low- f_{EM} , in the region of the calorimeter with poor muon coverage.

pileup, and at high luminosities the E_T^{miss} resolution can be seriously degraded. For this reason a correction to the term is introduced by attempting to match each deposit to the primary vertex, which leads to very stable resolution with increasing pileup.

5.9 Resolving ambiguity in object selection

It is not uncommon for an individual particle traversing the detector to be reconstructed by two or more of the algorithms described above. In order to resolve the potential ambiguity, a geometric overlap removal is performed between objects with a distance less than 0.2 in ΔR . This is done in the following order:

- Muon candidates are selected with the loosest quality criteria, and a p_T threshold of 4 GeV. Overlapping electron, tau, or jet candidates are removed.
- Remaining electron candidates are selected with the loosest quality criteria, with a p_T threshold of 15 GeV, and including the region $1.37 < |\eta| < 1.52$. Overlapping tau and jet candidates are removed.

- Remaining tau candidates are selected with a p_T cut of 20 GeV and standard quality criteria. Overlapping jet candidates are removed.

Chapter 6

EVENT SELECTION

This section describes the event selection criteria which are applied in order to distinguish MSSM Higgs events from the background processes. The selection applied depends on the Higgs mass hypothesis being tested; for Higgs masses below 200 GeV, the “low-mass” selection is used, while for higher masses the “high-mass” selection is used. The analyses use a common set of pre-selection criteria. Finally, the reconstruction of the invariant mass of the Higgs boson is described.

6.1 Pre-selection

Pre-selection refers to the basic quality criteria which are applied to events, as well as to the object selection necessary to define the event variables. The requirements which are applied are as follows:

- **Trigger** : Events must have been recorded by either a single-electron or single-muon trigger. The triggers have p_T thresholds of 24 GeV for the lepton, and include loose isolation and quality criteria.
- **Cleaning**: In order to suppress sources of fake jets or E_T^{miss} , events are rejected if they contain evidence of detector malfunction or non-collision backgrounds, such as cosmic rays. Specific problems include energy spikes in the hadronic endcap calorimeter, and coherent noise in the electromagnetic calorimeter [49].
- **Vertex**: At least one vertex with at least four tracks is required.
- **Lepton selection**: An isolated, high-quality lepton with transverse momentum $p_T > 26$ GeV, of the same flavor as the trigger which recorded the event.

- **Dilepton veto:** Events are rejected if they contain a second lepton. The looser lepton definitions used for overlap removal are used for the dilepton veto.
- **Tau selection:** Exactly one hadronic tau candidate passing the standard identification criteria, with $p_T > 25$ GeV is required.
- **Opposite sign:** The hadronic tau and the lepton must have opposite-sign charge.

6.2 Low-mass selection

After the pre-selection, the largest source of background comes from W+jets events, in which the hadronic tau is faked by an associated jet. Two variables are used to reduce this background. The first is $\Sigma\Delta\phi$, which is defined as the azimuthal angle between the lepton and the E_T^{miss} , plus the azimuthal angle between the τ_{had} and the E_T^{miss} :

$$\Sigma\Delta\phi = \Delta\phi(E_T^{miss}, \tau_h) + \Delta\phi(E_T^{miss}, lepton). \quad (6.1)$$

For signal events, the E_T^{miss} is due to the neutrinos from the tau decay, which are closely aligned with the tau decay products. It is therefore expected that the E_T^{miss} be aligned with one of them, especially the leptonic decay which has two neutrinos, or in between them due to vector addition. In either case, the value is seldom much more than pi. For W+jets events, the E_T^{miss} and lepton come from the W, while the tau candidate comes from a re-coiling jet. In these events it is usual that all three objects are well-separated, leading to relatively higher values of $\Sigma\Delta\phi$.

The second variable used is the transverse mass between the lepton and the E_T^{miss} , defined as

$$m_T = \sqrt{2p_T^{\text{lep}} E_T^{\text{miss}} (1 - \cos \Delta\phi)}, \quad (6.2)$$

The motivation for this cut is similar to the motivation for $\Sigma\Delta\phi$. The E_T^{miss} is usually closely aligned with the lepton for signal, which leads to small values. For W+jets events m_T peaks close to the W boson mass, as it is formed from the W decay products. Additionally, in top quark events, most of the objects have fairly high momentum, and there is no tendency

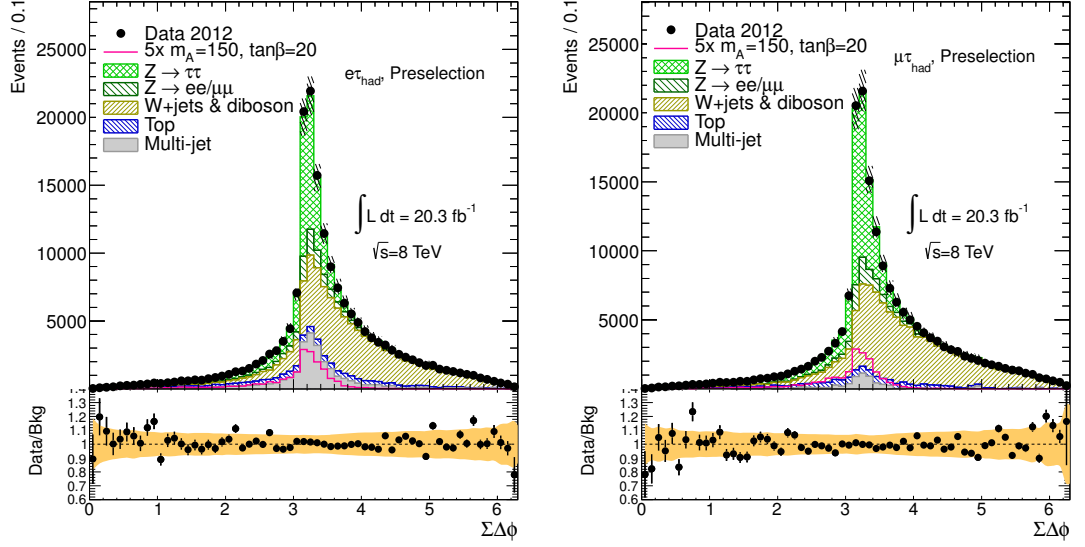


Figure 6.1: The variable $\Sigma\Delta\phi$ for the electron and muon channels, after the pre-selection requirements. A cut is made at 3.3. The signal contribution has been scaled up to increase visibility. The shaded bands indicate the total systematic uncertainty. See Section 7 for details on the background prediction.

for the E_T^{miss} and lepton to be aligned, so large values of m_T are expected. Plots of these variables may be seen in Figures 6.1 and 6.2.

After pre-selection, the event sample is split into b-tagged and b-vetoed sub-categories. Events in the b-tagged sub-category must have at least 1 jet which passes the b-tagging criterion, while events in the b-vetoed sub-category cannot have such a jet. This enhances the sensitivity to the b-associated production mechanism, while also targeting the gluon fusion Higgs production process. In the b-veto sub-category, the cuts $\Sigma\Delta\phi < 3.3$ and $m_T < 60$ GeV are applied. In the b-tag sub-category, the cut $m_T < 45$ GeV is applied. To reduce the contribution of top backgrounds in the b-tagged category, events are vetoed if there is an additional jet (besides the leading b-tagged jet) with transverse momentum above 30 GeV. Figure 6.2 shows the b-tagging score distribution, and the number of jets with $p_T > 30$ GeV after requiring one b-jet.

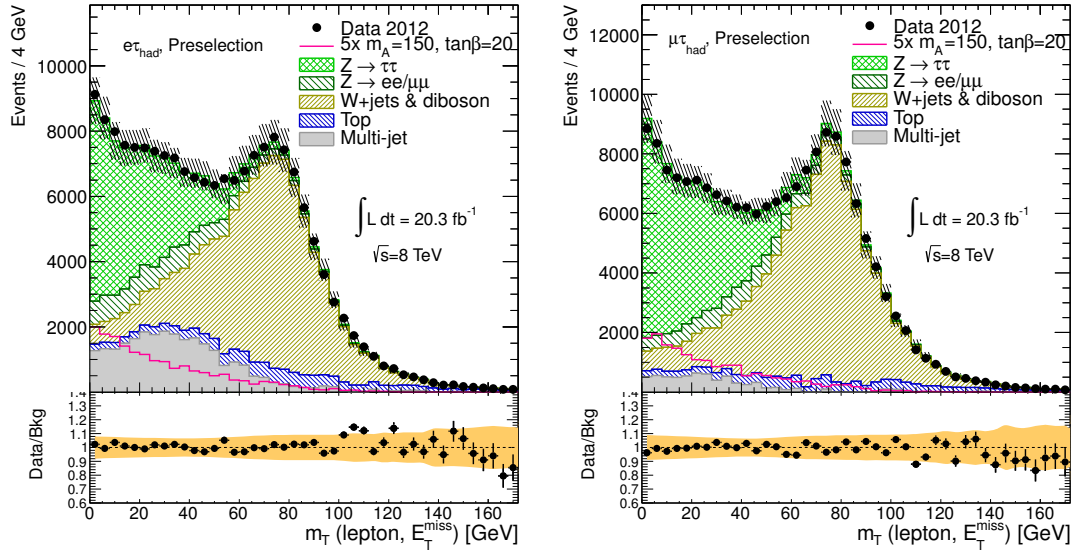


Figure 6.2: The transverse mass between the lepton and E_T^{miss} for the electron and muon channels, after the cut on $\Sigma\Delta\phi$. A cut is made at 60 GeV in the b-veto sub-channel, and 45 GeV in the b-tag sub-channel. The signal contribution has been scaled up to increase visibility. The shaded bands indicate the total systematic uncertainty. See Section 7 for details on the background prediction.

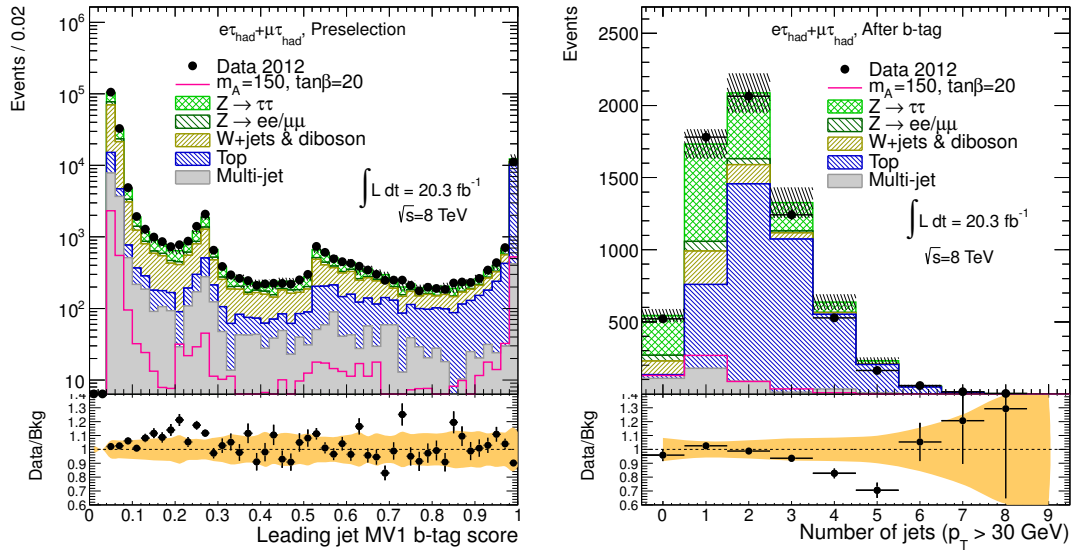


Figure 6.3: Left: The b-tagging score (known as “MV1”) for the leading jet in the event, after the cut on $\Sigma\Delta\phi$. Jets with a score above 0.7892 are considered “b-tagged”. Right: The number of jets with transverse mass above 30 GeV, after requiring a 20 GeV b-tagged jet. No jets are allowed above 30 GeV other than the leading b-tagged jet. Electron and muon channels are combined. The shaded bands indicate the total systematic uncertainty. See Section 7 for details on the background prediction.

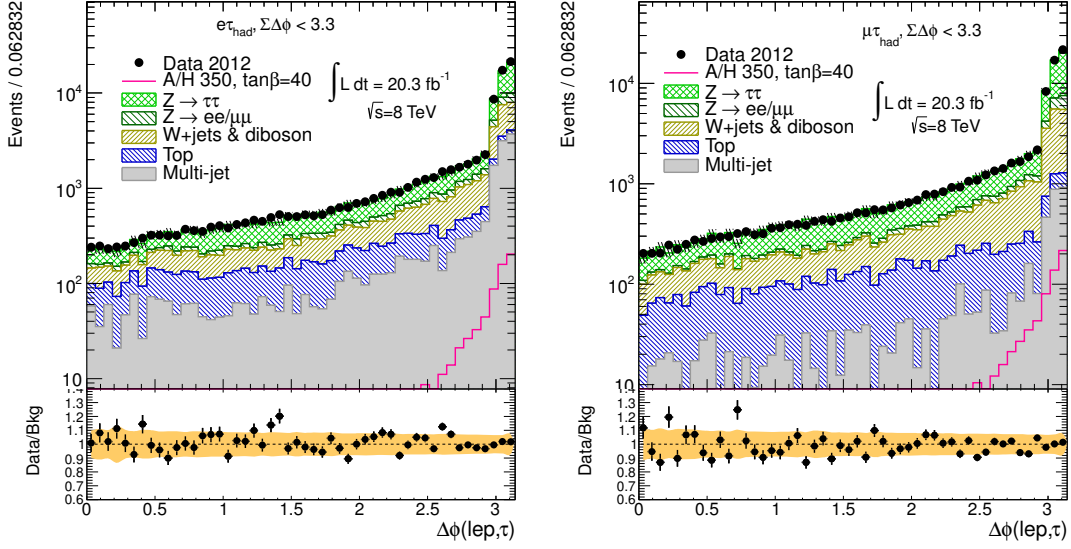


Figure 6.4: The azimuthal angle between the lepton and hadronic tau, for the electron and muon channels, after the cut on $\Sigma\Delta\phi$. A cut is made at 2.4 in the high-mass selection. The shaded bands indicate the total systematic uncertainty. See Section 7 for details on the background prediction.

6.3 High-mass selection

Due to the higher transverse momenta of the tau leptons, and to the typically lower relative transverse momentum of the decaying Higgs boson, the kinematics of high-mass and low-mass ditau resonances differ considerably. These differences are exploited to provide strong background rejection without having to use information on the associated jet(s).

As in the low-mass b-veto selection, the $\Sigma\Delta\phi$ is required to be less than 3.3. Because the p_T of the Higgs is lower relative to the mass for heavy Higgs bosons, the decaying tau leptons are typically well-separated. The azimuthal angle difference between the lepton and τ_{had} must be above 2.4. The distribution of this angular distance is shown in Figure 6.4.

Finally, hadronically decaying tau leptons usually have a higher percentage of visible vs. invisible energy compared to leptonically decaying tau leptons (which have two neutrinos). For this reason, the hadronic tau candidate is required to have a p_T at least 45 GeV greater than the lepton. This variable ($\Delta p_T = p_T(\tau_{had}) - p_T(lepton)$) offers excellent separation

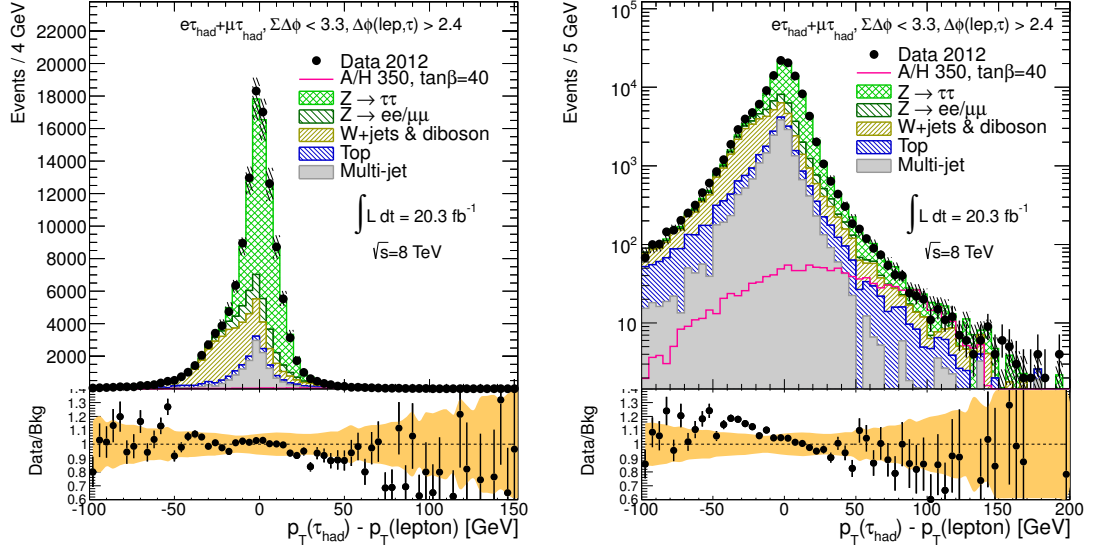


Figure 6.5: The transverse mass of the hadronic tau minus the transverse mass of the lepton, after the cuts on $\Sigma\Delta\phi$ and $\Delta\phi(\text{lepton}, \tau_{\text{had}})$. Electron and muon channels are combined. A cut is made at 45 GeV in the high-mass selection. As explained in Section 7, the background estimation procedure is different for the low-mass and high-mass channels. The low-mass estimate has been used for the plot on the left, showing good agreement for the bulk of the distribution. The high-mass estimate has been used for the plot on the right, showing improved agreement in the high-mass signal region. The shaded bands indicate the total systematic uncertainty. See Section 7 for details on the background prediction.

from W and top backgrounds, for which the lepton is usually harder, as well as from Z and QCD multijet backgrounds, which seldom have such a large imbalance. This can be seen in Figure 6.5.

The high mass selection is applied when testing Higgs boson mass hypotheses greater than or equal to 200 GeV. Electron and muon events are treated as a single category for high mass, in order to ensure adequate statistics, while in the low-mass channels they are taken separately and statistically combined.

6.4 Mass reconstruction

After the event selection, the ditau invariant mass distribution of the resulting event sample is used to test the signal hypotheses against the background-only hypothesis. However, due

to the presence of multiple un-detected neutrinos, it is impossible to fully reconstruct the Higgs boson candidate mass. Instead, a likelihood-based approach known as the Missing Mass Calculator (MMC) [55] is employed.

In a semi-leptonic di-tau event, there are seven unknown kinematic quantities:: x -, y -, and z -components of the invisible momentum carried by neutrino(s) for each of the two taus in the event, and the invariant mass of the two neutrinos from the leptonic tau decay. However, there are only 4 equations available:

$$\begin{aligned}
E_x^{miss} &= p_{\text{mis}_1} \sin \theta_{\text{mis}_1} \cos \phi_{\text{mis}_1} + p_{\text{mis}_2} \sin \theta_{\text{mis}_2} \cos \phi_{\text{mis}_2} \\
E_y^{miss} &= p_{\text{mis}_1} \sin \theta_{\text{mis}_1} \sin \phi_{\text{mis}_1} + p_{\text{mis}_2} \sin \theta_{\text{mis}_2} \sin \phi_{\text{mis}_2} \\
M_{\tau_1}^2 &= m_{\text{mis}_1}^2 + m_{\text{vis}_1}^2 + 2\sqrt{p_{\text{vis}_1}^2 + m_{\text{vis}_1}^2} \sqrt{p_{\text{mis}_1}^2 + m_{\text{mis}_1}^2} \\
&\quad - 2p_{\text{vis}_1} p_{\text{mis}_1} \cos \Delta\theta_{vm_1} \\
M_{\tau_2}^2 &= m_{\text{vis}_2}^2 + 2\sqrt{p_{\text{vis}_2}^2 + m_{\text{vis}_2}^2} \sqrt{p_{\text{mis}_2}^2 + m_{\text{mis}_2}^2} \\
&\quad - 2p_{\text{vis}_2} p_{\text{mis}_2} \cos \Delta\theta_{vm_2}.
\end{aligned} \tag{6.3}$$

In these equations, $M_\tau=1.777$ GeV is the tau invariant mass, E_x^{miss} and E_y^{miss} are the x - and y -components of the E_T^{miss} vector, $p_{\text{vis}_{1,2}}$, $m_{\text{vis}_{1,2}}$, $\theta_{\text{vis}_{1,2}}$, $\phi_{\text{vis}_{1,2}}$ are the momenta, invariant masses, polar and azimuthal angles of the visible τ decay products. All of these quantities are measured in the event. The remaining variables are the unknowns: the combined invisible (“missing”) momenta $\vec{p}_{\text{mis}_{1,2}}$ carried away by the neutrino (or neutrinos) for each of the two decaying τ ’s, and the invariant mass of the neutrinos in the leptonic τ decay, m_{mis_1} . Finally, $\Delta\theta_{vm_{1,2}}$ is the angle between the vectors \vec{p}_{mis} and \vec{p}_{vis} for each of the two taus, and it can be expressed in terms of the other variables.

Although the number of unknowns exceeds the number of constraints, some solutions of this under-constrained system are more likely, and additional knowledge of the τ decay kinematics can be used to distinguish them from less likely ones. In particular, events are weighted according to the 3-dimensional angle between the directions of visible and invisible tau decay products ($\Delta\theta_{3D}$). Figure 6.6 shows the $\Delta\theta_{3D}$ angle for the three different tau decay types: leptonic, 1-prong hadronic and 3-prong hadronic, using tau decays simulated with PYTHIA and TAUOLA, and reconstructed with the full ATLAS detector simulation.

The probability density functions have been derived by fitting these distributions with a linear combination of Gaussian and Landau functions.

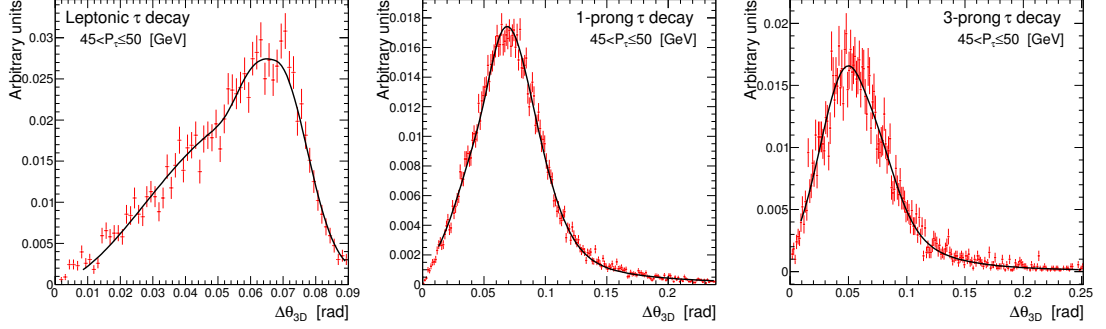


Figure 6.6: Example of the probability distribution functions $\mathcal{P}(\Delta\theta, p_\tau)$ for a particular value of the original τ lepton momentum ($45 < p_\tau \leq 50$ GeV). These functions are used in the calculation of the global event probability \mathcal{P}_{event} for three cases: leptonic decays (left plot), 1-prong taus (middle plot), and 3-prong taus (right plot). These distributions depend only on the decay type and initial momentum of the tau.

The system of Eqs. 6.3 may be solved for any point in the $(\phi_{\text{mis}_1}, \phi_{\text{mis}_2}, m_{\text{mis}_1})$ parameter space. For each point in that space, the vectors $\vec{p}_{\text{mis}_{1,2}}$ are fully defined and, therefore, the angle $\Delta\theta_{3D\ 1,2}$ between the vector $\vec{p}_{\text{vis}_{1,2}}$ and the current assumed direction of $\vec{p}_{\text{mis}_{1,2}}$ is calculated. To evaluate the probability of each point in the parameter space, $\Delta\theta_{3D}$ distributions are used as shown in Fig. 6.6, taking into account additionally the dependence of the distribution on the momentum of the initial tau and its decay type.

For each event, the $(\phi_{\text{mis}_1}, \phi_{\text{mis}_2}, m_{\text{mis}_1})$ parameter space is scanned, and the resulting $m_{\tau\tau}$ is weighted according to the probability of the point in the parameter space. The result is a distribution of $m_{\tau\tau}$ values, and the mode of this distribution is chosen as the Higgs boson candidate mass for the event. Figures 10.1, 10.2, and 10.3 show the final MMC invariant mass distribution in the three final state categories.

Chapter 7

BACKGROUND ESTIMATION

In order to test the signal hypothesis, it is necessary to have a solid understanding of the expected distributions from all of the known Standard Model processes. Although this can be done using Monte Carlo simulation, correctly modelling proton collisions is difficult and comes with large uncertainties. For this reason, the background predictions have been estimated, wherever possible, directly using the data.

7.1 $Z \rightarrow \tau\tau$ background modelling

The process $Z \rightarrow \tau\tau$ forms a final state very similar to the MSSM Higgs signal, and is the most important background, particularly at low mass. For this reason, correctly modelling the background is critical, and should be done using data, if possible. However, it is very difficult to define a selection that gives a pure sample of $Z \rightarrow \tau\tau$ events that is not also contaminated by potential signal events.

$Z \rightarrow \mu\mu$ decays provide a good starting point to model $Z \rightarrow \tau\tau$ events in a data-driven way. Except for effects due to the different muon and tau masses, the two processes are kinematically identical, including other activity in the event. Due to the small Higgs coupling to muons, $Z \rightarrow \mu\mu$ events provide a virtually signal-free signature of two isolated, high-energy muons with opposite charge. In order to model $Z \rightarrow \tau\tau$, these $Z \rightarrow \mu\mu$ events are modified using an embedding technique which replaces the muons from the Z decay by the decay products of simulated taus. Here, the tau lepton kinematics are given by the kinematics of the original muons and the tau decays are taken from the Monte Carlo simulation, which is justified by the comparatively well-understood decays of Z bosons and τ -leptons.

The procedure of embedding simulated tau decays into $Z \rightarrow \mu\mu$ data events proceeds as follows:

- **Selection of $Z \rightarrow \mu\mu$ events:** The selection of the $Z \rightarrow \mu\mu$ input data requires exactly two muons as defined in Section 5 with $p_T > 25$ GeV. In addition, these muons are required to have a common primary vertex and an invariant mass greater than 40 GeV.

- **Extraction of the $Z \rightarrow \mu\mu$ kinematics:**

The kinematics of the Z boson and its decay are reconstructed from the selected muons in the data events. The muons are then replaced by simulated taus, with their four-momenta rescaled in the Z rest frame, so that

$$p_\tau = \sqrt{E_\mu^2 - m_\tau^2}$$

in order to account for the mass difference between the muons and taus.

- **Production of corresponding simulated $Z \rightarrow \tau\tau$ decays:** Using the extracted kinematics, an event containing only the decaying tau leptons is run through the full ATLAS detector simulation. The final output of this step is a clean $Z \rightarrow \tau\tau$ event without calorimeter noise or pile-up, which will be referred to as a *mini event*.
- **Merging of data and simulated information:** In order to replace the muons with the correspondingly simulated tau, all associated muon tracks are removed in the original $Z \rightarrow \mu\mu$ data event. To subtract the energy deposition of the muons in the calorimeter, a second *mini event* with the initial $Z \rightarrow \mu\mu$ kinematics is produced, and the simulated calorimeter energy is subtracted from the $Z \rightarrow \mu\mu$ data event on cell level. Then all calorimeter cell energies from the simulated $Z \rightarrow \tau\tau$ event are added to the corresponding data, and all tracks are copied. This inserts the pure $Z \rightarrow \tau\tau$ decay into the data environment while keeping the event properties as close to data conditions as possible.
- **Re-reconstruction of the embedded events:** The resulting $Z \rightarrow \tau\tau$ hybrid events are then submitted to a full event reconstruction, so that all objects and the missing transverse energy are recreated from the modified cells and tracks.

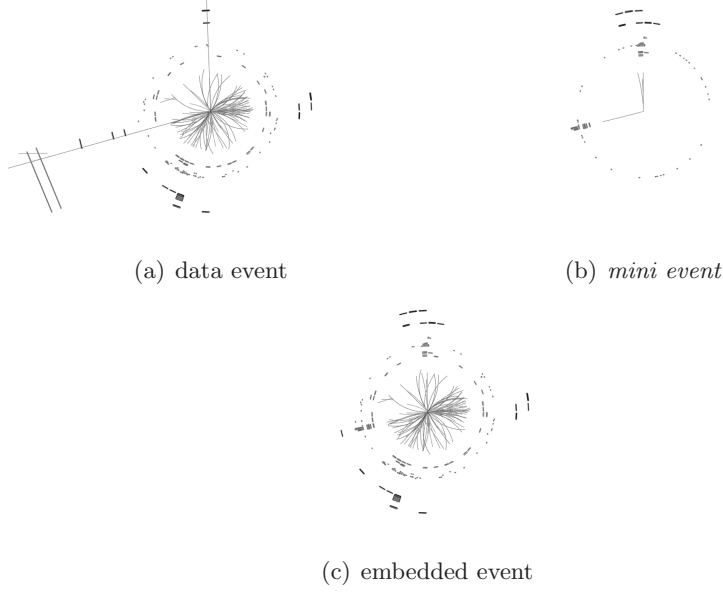


Figure 7.1: Example event displays of the embedding steps for a single $Z \rightarrow \mu\mu$ to $Z \rightarrow \tau\tau$ event: (a) after the selection, (b) after the Monte Carlo simulation, and (c) after the re-reconstruction.

An example of the process may be seen in Figure 7.1. In the analysis, the embedded event sample is used to model the shape of the relevant distributions as well as the relative selection efficiencies, after a basic trigger and object selection. It is not straightforward, however, to obtain the absolute normalization from the embedded events alone. For this reason, the embedding is normalized to the prediction from Monte Carlo at the pre-selection stage.

7.2 *Multi-jet background modelling*

Although they contain neither a true hadronic tau nor a true electron or muon, multi-jet events may pass the event selection if both of these objects come from mis-identified jets; and due to the very large cross-section for multi-jet production, this background cannot be ignored. Estimating this background from simulation is difficult for a variety of reasons. The huge cross section for multi-jet events, combined with the relatively small fake rate after the selection requirements and the integrated luminosity of the data sample used in this

study, would require the generation of an unrealistically large number of events. Moreover, the rate at which jets are misidentified as taus cannot be reliably simulated by Monte Carlo.

These difficulties are overcome by estimating the multijet background directly from data using a two-dimensional sideband extrapolation method, commonly known as an ABCD method. To implement this, two selection criteria are chosen which are uncorrelated for multijet events, and the sample is split into four regions, by either applying or reversing each criterion. The two variables chosen are the charge correlation between the lepton and hadronic tau, and the isolation of the lepton. These two variables are used to define four regions depending on whether the tau and lepton charges have the same sign (SS) or opposite sign (OS), and whether the lepton passes or fails the isolation criteria (see Section 5. The lepton must fail both track and calorimeter isolation to be included in this region). All selection criteria besides these are applied as normal, and the estimation is done separately for each of the three signal regions (low-mass b-tagged, low-mass b-vetoed, and high-mass). The four regions will be denoted as A (the signal region), B, C and D, see Table 7.1.

Table 7.1: Definition of signal and control regions according to the charge correlation between the light lepton and the τ lepton (OS vs. SS) and the isolation of the light lepton (isolation vs. inverted isolation).

	Isolation	Inverted Isolation
OS	A (Signal)	B
SS	C	D

The estimation of the multijet background in region A (signal region) is done by extrapolating the event rate and shape of region C (the same-sign, isolated region) using the Opposite-Sign to Same-Sign ratio measured from regions B and D :

$$n_A^{multijet} = n_C \frac{n_B}{n_D} \equiv r_{B/D} n_C. \quad (7.1)$$

The regions B, C, and D are not completely multijet-pure, and other backgrounds must be subtracted before Eq. 7.1 can be applied. In particular, region C contains a significant

amount of W +jets. These processes are estimated from simulation, and in cases where the Monte Carlo is scaled to data (such as W and top, as described in the next section), this scaling is also performed in the regions B, C, and D. The populations of the ABCD regions are shown in Tables 7.2, 7.3, and 7.4 for the three channels. The contributions of non-multijet processes is also shown. The values of the opposite-sign to same-sign ratio are shown in Table 7.5.

Table 7.2: Observed data events and expected numbers of events from simulation in the regions B, C, and D used in the multijet background estimation in the low-mass b -tag channel. For W +jets, Z +jets and $t\bar{t}$ samples a normalization correction factor (Section 7.3) is applied to the predicted MC event yields.

Electron Channel, low-mass b -tag sample			
	B	C	D
Data	807	313	783
$Z \rightarrow \tau\tau$	5.6 ± 1.5	5.7 ± 1.1	0.9 ± 0.6
W +jets	1.9 ± 1.2	69.8 ± 10.3	0.0 ± 0.0
top	6.1 ± 1.4	18.2 ± 4.0	1.5 ± 0.8
$Z \rightarrow \ell\ell$	0.0 ± 0.0	22.4 ± 9.8	0.0 ± 0.0
Diboson	0.7 ± 0.7	4.3 ± 1.3	0.0 ± 0.0
Muon Channel, low-mass b -tag sample			
	B	C	D
Data	651	208	621
$Z \rightarrow \tau\tau$	4.3 ± 0.9	4.0 ± 0.9	0.6 ± 0.3
W +jets	2.4 ± 1.7	108.7 ± 21.0	0.0 ± 0.0
top	2.0 ± 0.8	21.3 ± 4.4	1.5 ± 0.6
$Z \rightarrow \ell\ell$	0.0 ± 0.0	20.6 ± 10.5	0.0 ± 0.0
Diboson	0.0 ± 0.0	2.1 ± 0.8	0.0 ± 0.0

Table 7.3: Observed data events and expected numbers of events from simulation in the regions B, C, and D used in the multijet background estimation in the low-mass b -veto channel. For W +jets, Z +jets and $t\bar{t}$ samples a normalization correction factor (Section 7.3) is applied to the predicted MC event yields.

Electron Channel, b -veto sample			
	B	C	D
Data	17724	17647	16092
$Z \rightarrow \tau\tau$	453.2 ± 10.7	401.6 ± 17.5	12.8 ± 4.4
W +jets	106.6 ± 9.6	3296.7 ± 80.3	58.3 ± 10.7
top	30.7 ± 5.5	157.3 ± 11.6	16.8 ± 4.6
$Z \rightarrow \ell\ell$	68.3 ± 20.4	2539.2 ± 107.7	18.9 ± 5.7
Diboson	2.0 ± 0.6	108.8 ± 5.5	1.8 ± 0.7
Muon Channel, b -veto sample			
	B	C	D
Data	11110	8394	9352
$Z \rightarrow \tau\tau$	350.2 ± 8.2	310.1 ± 15.0	6.9 ± 3.7
W +jets	51.6 ± 10.1	3496.2 ± 101.1	15.7 ± 3.9
top	25.2 ± 4.8	154.2 ± 11.6	18.6 ± 6.0
$Z \rightarrow \ell\ell$	11.1 ± 3.7	1335.3 ± 90.1	3.0 ± 1.2
Diboson	3.9 ± 1.2	97.6 ± 5.5	0.4 ± 0.3

Table 7.4: Observed data events and expected numbers of events from simulation in the regions B, C, and D used in the multijet background estimation in the high-mass channel. For W +jets, Z +jets and $t\bar{t}$ samples a normalization correction factor (Section 7.3) is applied to the predicted MC event yields.

Electron Channel, high-mass sample			
	B	C	D
Data	273	89	212
$Z \rightarrow \tau\tau$	4.1 ± 1.3	2.5 ± 1.1	0.4 ± 0.4
W +jets	4.0 ± 1.5	27.3 ± 6.3	0.0 ± 0.0
top	3.4 ± 0.9	7.7 ± 1.5	2.1 ± 0.8
$Z \rightarrow \ell\ell$	1.2 ± 1.1	5.0 ± 2.5	0.0 ± 0.0
Diboson	0.1 ± 0.1	2.3 ± 0.8	0.3 ± 0.3
Muon Channel, high-mass sample			
	B	C	D
Data	390	56	316
$Z \rightarrow \tau\tau$	5.1 ± 1.2	3.3 ± 0.9	0.0 ± 0.0
W +jets	3.0 ± 1.3	25.5 ± 6.7	0.4 ± 0.3
top	2.9 ± 0.8	6.7 ± 1.7	1.3 ± 0.6
$Z \rightarrow \ell\ell$	1.6 ± 1.0	5.3 ± 2.2	0.0 ± 0.0
Diboson	0.0 ± 0.0	3.2 ± 1.1	0.0 ± 0.0

7.2.1 Tests of the ABCD method predictions

The method assumes that the two variables in use are un-correlated, i.e. that the opposite-sign to same-sign ratio for multijet events does not depend on the lepton isolation. This has been tested by splitting the anti-isolated regions into sub-regions near the isolation threshold and far away from the threshold. The value of $r_{B/D}$ in these regions can be seen in Table 7.6, and may be compared to Table 7.5. Some variation is seen in the intermediate regions, especially at high mass, which is taken as a systematic uncertainty on the method.

Table 7.5: Opposite-sign to same-sign ratio for multijet events, as measured in regions B and D.

	Electron Channel	Muon Channel
b-tag	1.02 ± 0.05	1.04 ± 0.06
b-veto	1.067 ± 0.012	1.146 ± 0.017
high	1.24 ± 0.12	1.20 ± 0.09

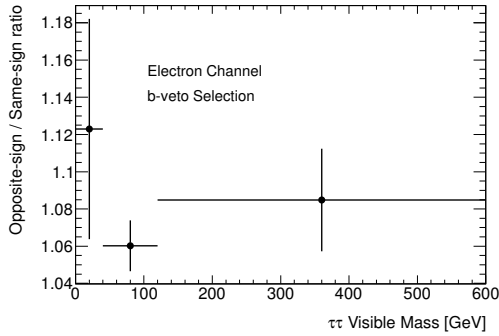
Additionally, $r_{B/D}$ may vary across the invariant mass range considered, as different kinematics may lead to different fractions of quark and gluon processes. A lower ratio is typically seen at higher masses, as shown in Figure 7.2. This is most relevant for the low-mass b-veto category: the requirement of a b-jet reduces charge correlations in the b-tag category; while for the high-mass selection, there are insufficient statistics to observe a trend. A 10% uncertainty is assigned in the b-veto category to account for possible variations across the mass range relevant for this category, while in the high-mass selection, a 12% uncertainty is applied.

7.3 Modelling of backgrounds with jets faking taus

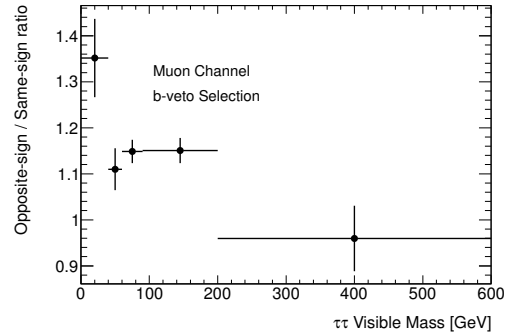
The rate at which quark or gluon-initiated jets fake the hadronic tau signature is very difficult to model correctly in simulation. For this reason, backgrounds in which the identified tau comes from a jet (sometimes or always) are normalized using control regions in the data. The backgrounds estimated in this way are W+jets, top (both single-top and $t\bar{t}$),

Table 7.6: Opposite-sign to same-sign ratio for multijet events, as measured in regions with the anti-isolation criteria systematically varied. Here $p_T 0.4$ refers to the sum of the transverse momenta of tracks within a cone of 0.4 around the lepton, while $E_T 0.2$ refers to the total energy of calorimeter deposits within a cone of 0.2 around the lepton.

Electron	$p_T 0.4 > 0.06$	$p_T 0.4 > 0.06$	$0.06 > p_T 0.4 > 0.12$	$p_T 0.4 > 0.12$
Channel	$0.06 < E_T 0.2 < 0.12$	$E_T 0.2 > 0.12$	$E_T 0.2 > 0.06$	$E_T 0.2 > 0.06$
b-tag	0.98 ± 0.09	1.03 ± 0.06	0.93 ± 0.11	1.04 ± 0.06
b-veto	1.065 ± 0.019	1.068 ± 0.015	1.07 ± 0.03	1.068 ± 0.014
high	0.91 ± 0.18	1.37 ± 0.15	1.17 ± 0.30	1.25 ± 0.13
Muon	$p_T 0.4 > 0.06$	$p_T 0.4 > 0.06$	$0.06 > p_T 0.4 > 0.12$	$p_T 0.4 > 0.12$
Channel	$0.06 < E_T 0.2 < 0.12$	$E_T 0.2 > 0.12$	$E_T 0.2 > 0.06$	$E_T 0.2 > 0.06$
b-tag	1.10 ± 0.11	1.01 ± 0.07	1.13 ± 0.11	0.99 ± 0.07
b-veto	1.12 ± 0.03	1.16 ± 0.02	1.24 ± 0.03	1.09 ± 0.02
high	0.76 ± 0.16	1.30 ± 0.11	1.21 ± 0.17	1.20 ± 0.11



(a)



(b)

Figure 7.2: The ratio of opposite-sign to same-sign multijet events measured in the anti-isolated regions, as a function of the ditau visible mass.

and $Z \rightarrow \ell\ell$. For the latter, only events in which the reconstructed tau comes from an associated jet are measured in this way. Events where an electron fakes a tau are scaled using a fake rate measurement described in [51], while the less common events where a muon fakes a tau are taken from simulation, with a large uncertainty applied.

Separate control regions are defined for each of the three signal states (low-mass b-veto, low-mass b-tag, and high-mass). This is necessary for low mass because the b-tagging requirement can affect strongly the flavor composition of the sample, and for high mass because the “tau” p_T spectrum is much harder due to the selection. Both of these effects are correlated with the jet-to-tau fake rate.

For the $Z \rightarrow \ell\ell$ background, the dilepton veto is dropped, and instead two opposite-sign, same-flavor leptons are required. (This is in addition to the regular tau identification requirement). The invariant mass of the two leptons must be between 70 and 110 GeV. For the scale factor in the b-tagged region, an additional b-tagged jet with p_T below 60 GeV is required. Finally, for the high-mass region, the p_T requirement of the tau is raised to 85 GeV (This ensures roughly equivalent “tau” p_T spectra between the signal and control regions).

For the W+jets background, the $\Sigma\Delta\phi$ is required to be above 3.6, and the E_T^{miss} must be above 30 GeV. To obtain the scale factor for the b-vetoed sub-channel, a veto on any b-tagged jets is applied. For the b-tagged sub-channel, exactly one b-tagged jet, with p_T less than 60 GeV, is required. Finally, in the high-mass region, a veto on b-tagged jets is applied, the tau p_T must be above 100 GeV, and the E_T^{miss} cut is raised to 40 GeV. To increase statistics in this region, the $\Sigma\Delta\phi$ is only required to be above 3.4.

For the top background, at least one b-tagged jet with p_T above 60 GeV is required. Additionally, E_T^{miss} must be above 20 GeV, and the m_T between the lepton and the E_T^{miss} must be above 60 GeV. Finally, the scalar sum of the transverse momentum of all jets in the event must be at least 150 GeV. These criteria are applied for both low-mass sub-channels. At high mass, the tau p_T is raised to 85 GeV, and the jet p_T sum requirement is loosened to 100 GeV.

The predicted and observed event yields for each control region are shown in Tables 7.7, 7.8, and 7.9. To derive the scale factors, backgrounds other than the one in question are

first subtracted from the data in each region. For W and top, the scale factors are derived separately for opposite-sign and same-sign events, due to different flavor composition of the jets or taus in these samples. In any case, no difference is observed between the electron and muon channels, so a combined scale factor is used. Finally, there is a non-negligible contribution of W backgrounds in the top control regions, and vice-versa. To account for this, the scale factors (k_W and k_t) are derived simultaneously, by solving the following equations:

$$\begin{aligned} n_{Data}^{W-reg} - n_{other}^{W-reg} &= k_W * n_W^{W-reg} + k_t * n_t^{W-reg} \\ n_{Data}^{t-reg} - n_{other}^{t-reg} &= k_W * n_W^{t-reg} + k_t * n_t^{t-reg}. \end{aligned} \tag{7.2}$$

The k -factors thus derived are shown in Table 7.10.

Table 7.7: Number of events in the control regions used for normalizing the $Z \rightarrow \ell\ell$ backgrounds with jets faking taus. Veto, tag, and high refer to the low-mass b-veto, low-mass b-tag, and high-mass selections, while OS and SS refer to events with opposite-sign and same-sign lepton and tau candidates.

$Z \rightarrow \ell\ell$ region	Data	$Z \rightarrow \ell\ell$ (jet-fake)	Other backgrounds
veto, $e\tau_{had}$ channel	6174	7661.3	178.0
tag, $e\tau_{had}$ channel	138	102.8	21.6
high, $e\tau_{had}$ channel	362	478.7	24.6
veto, $\mu\tau_{had}$ channel	11294	13958.9	330.2
tag, $\mu\tau_{had}$ channel	268	145.2	42.9
high, $\mu\tau_{had}$ channel	632	890.0	40.7

7.4 Other backgrounds

The remaining backgrounds which are considered are $Z \rightarrow \ell\ell$ events in which an electron or muon is identified as a hadronic tau, and diboson WW, WZ, and ZZ production. $Z \rightarrow$

Table 7.8: Number of events in the control regions used for normalizing the W+jets background. Veto, tag, and high refer to the low-mass b-veto, low-mass b-tag, and high-mass selections, while OS and SS refer to events with opposite-sign and same-sign lepton and tau candidates.

W+jets region	Data	W+jets	Other backgrounds
veto, SS, $e\tau_{had}$ channel	14992	14133.6	793.7
veto, OS, $e\tau_{had}$ channel	39540	45708.4	3119.1
tag, SS, $e\tau_{had}$ channel	188	113.7	32.9
tag, OS, $e\tau_{had}$ channel	652	342.2	316.5
high, SS, $e\tau_{had}$ channel	63	70.4	7.8
high, OS, $e\tau_{had}$ channel	279	409.1	69.8
veto, SS, $\mu\tau_{had}$ channel	16926	16900.4	1327.4
veto, OS, $\mu\tau_{had}$ channel	46670	55995.2	3958.6
tag, SS, $\mu\tau_{had}$ channel	198	176.6	49.9
tag, OS, $\mu\tau_{had}$ channel	657	391.7	336.3
high, SS, $\mu\tau_{had}$ channel	53	67.0	13.2
high, OS, $\mu\tau_{had}$ channel	13	370.2	73.5

Table 7.9: Number of events in the control regions used for normalizing the top quark backgrounds. Veto, tag, and high refer to the low-mass b-veto, low-mass b-tag, and high-mass selections, while OS and SS refer to events with opposite-sign and same-sign lepton and tau candidates.

top region	Data	top	Other backgrounds
tag/veto, SS, $e\tau_{had}$ channel	598	470.0	79.2
tag/veto, OS, $e\tau_{had}$ channel	2363	2016.3	103.3
high, SS, $e\tau_{had}$ channel	39	33.6	28.5
high, OS, $e\tau_{had}$ channel	340	317.6	26.6
tag/veto, SS, $\mu\tau_{had}$ channel	600	478.4	86.2
tag/veto, OS, $\mu\tau_{had}$ channel	2322	2113.4	93.0
high, SS, $\mu\tau_{had}$ channel	51	29.5	15.8
high, OS, $\mu\tau_{had}$ channel	379	321.9	30.7

Table 7.10: Scale factors used for normalizing the W, top, and $Z \rightarrow \ell\ell$ backgrounds. Errors are statistical.

Channel	Opposite Sign	Same Sign
$Z \rightarrow \ell\ell$, veto	0.784 ± 0.008	
$Z \rightarrow \ell\ell$, tag	1.38 ± 0.11	
$Z \rightarrow \ell\ell$, high	0.69 ± 0.03	
W+jets, veto	0.776 ± 0.010	0.96 ± 0.03
W+jets, tag	0.82 ± 0.07	1.03 ± 0.13
W+jets, high	0.57 ± 0.05	0.69 ± 0.13
top, veto	1.09 ± 0.02	1.09 ± 0.05
top, tag	1.09 ± 0.08	1.08 ± 0.18
top, high	1.07 ± 0.09	0.91 ± 0.30

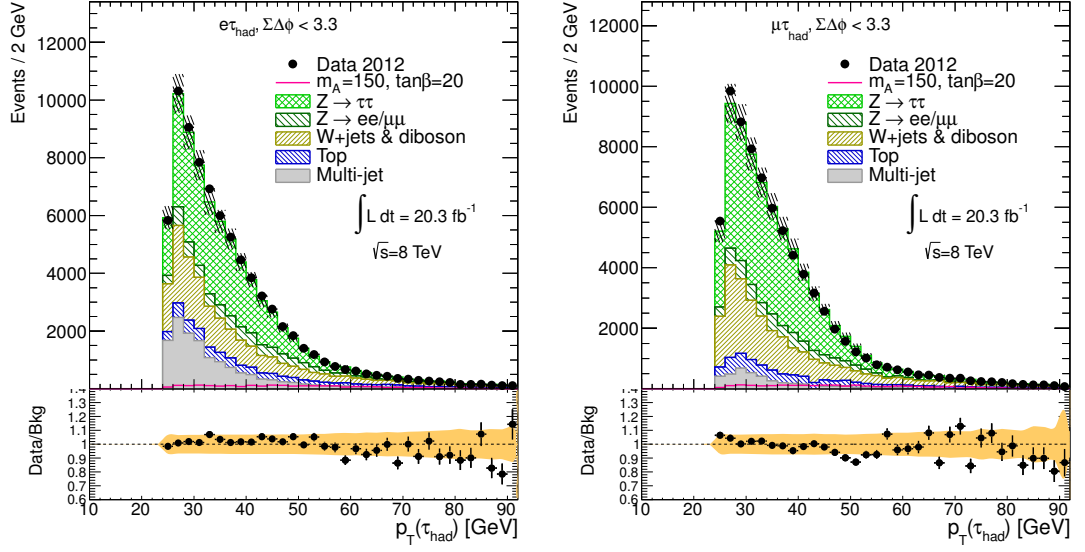


Figure 7.3: The transverse momentum of the hadronic tau for the electron and muon channels, after the cut on $\Sigma\Delta\phi$. The shaded bands indicate the total systematic uncertainty.

$\ell\ell$ events are taken from simulation, with a correction applied for the electron-to-tau fake rate as measured in data. The small diboson backgrounds are taken from simulation.

7.5 Performance of background modelling

Distributions for the selection variables comparing data to the background prediction have been shown in Section 6. This section shows further kinematic distributions, plotted with certain cuts removed from the selection criteria to reduce possible signal contributions. These plots were used as validation of the background estimation procedure prior to unblinding the signal regions.

7.5.1 Validation for the low-mass b -veto channel

Figures 7.3 to 7.6 show the p_T of the hadronic tau and the lepton, the E_T^{miss} , and the invariant mass of the visible tau decay products, all plotted prior to the b -jet veto and the cut $m_T < 60$.

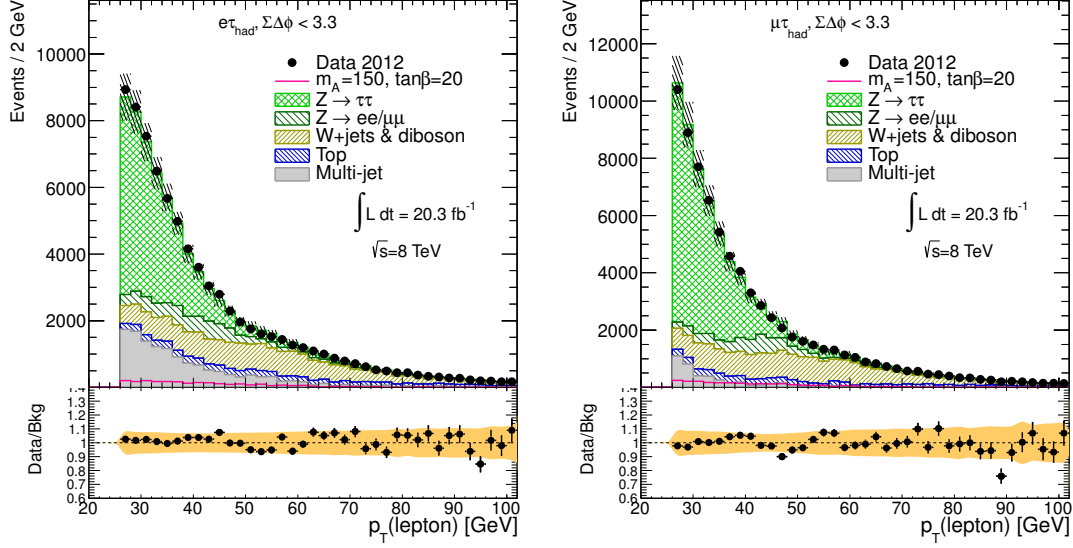


Figure 7.4: The transverse momentum of the electron or muon, after the cut on $\Sigma\Delta\phi$. The shaded bands indicate the total systematic uncertainty.

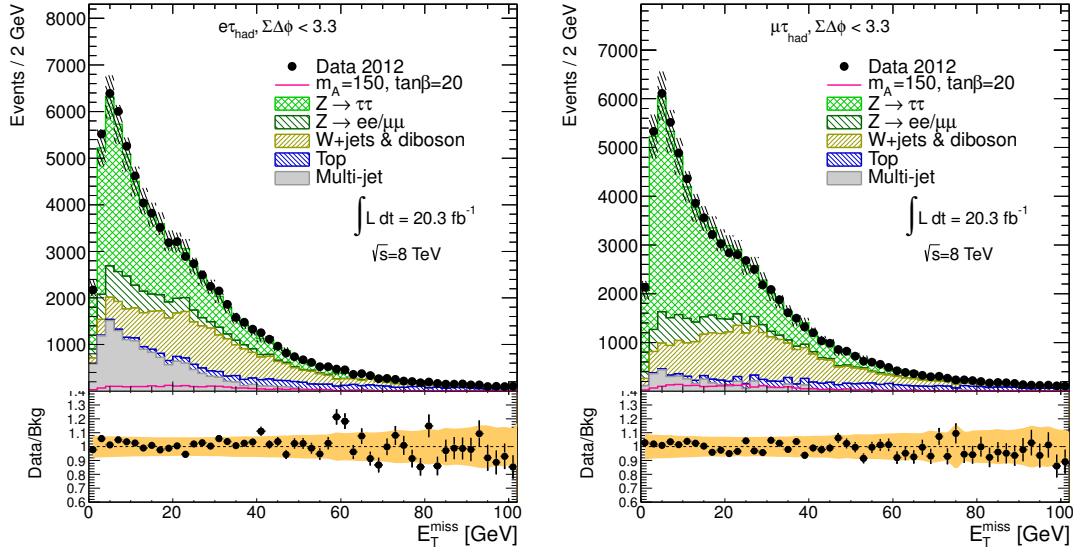


Figure 7.5: The missing trasverse energy for the electron and muon channels, after the cut on $\Sigma\Delta\phi$. The shaded bands indicate the total systematic uncertainty.

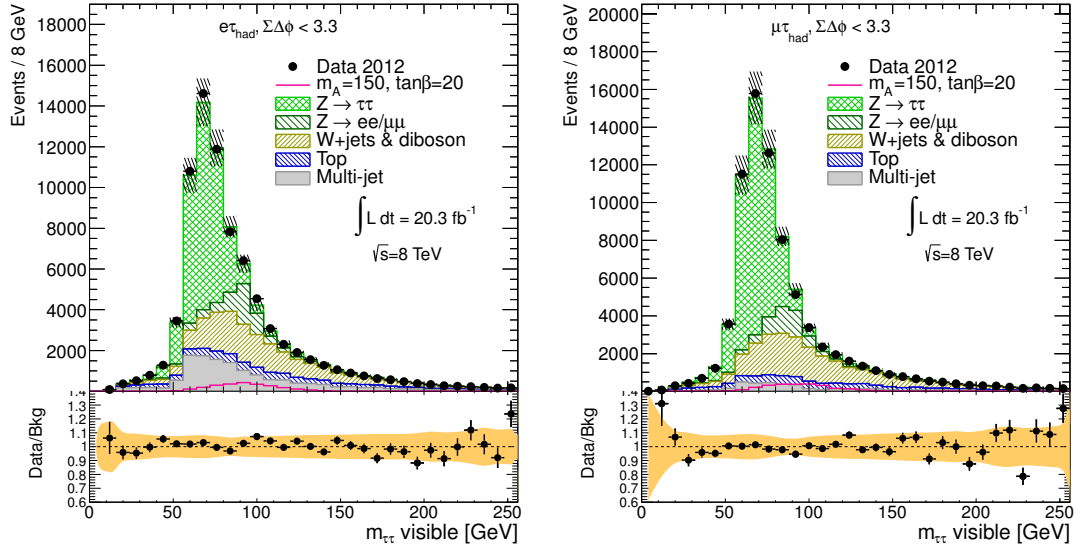


Figure 7.6: The invariant mass of the lepton and the hadronic tau, after the cut on $\Sigma\Delta\phi$. The shaded bands indicate the total systematic uncertainty.

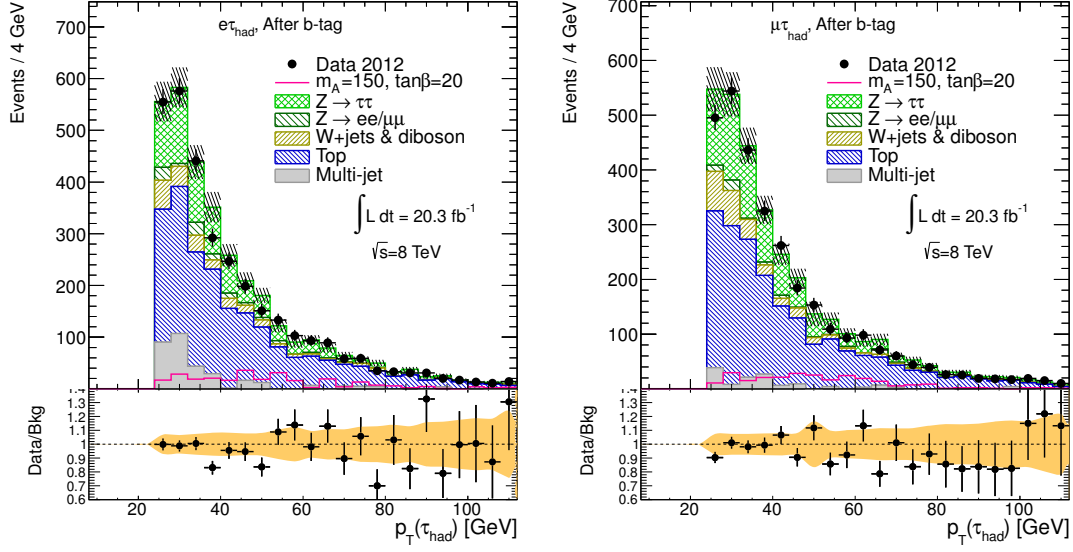


Figure 7.7: The transverse momentum of the hadronic tau for the electron and muon channels, after the b-tag and prior to the veto on a second jet. The shaded bands indicate the total systematic uncertainty.

7.5.2 Validation for the low-mass b-tag channel

Figures 7.7 to 7.10 show the p_T of the hadronic tau and the lepton, the E_T^{miss} , and the invariant mass of the visible tau decay products, all plotted after the b-tag requirement and the cut $m_T < 45$. This is equivalent to the full low-mass b-tag selection, without the veto on a second jet.

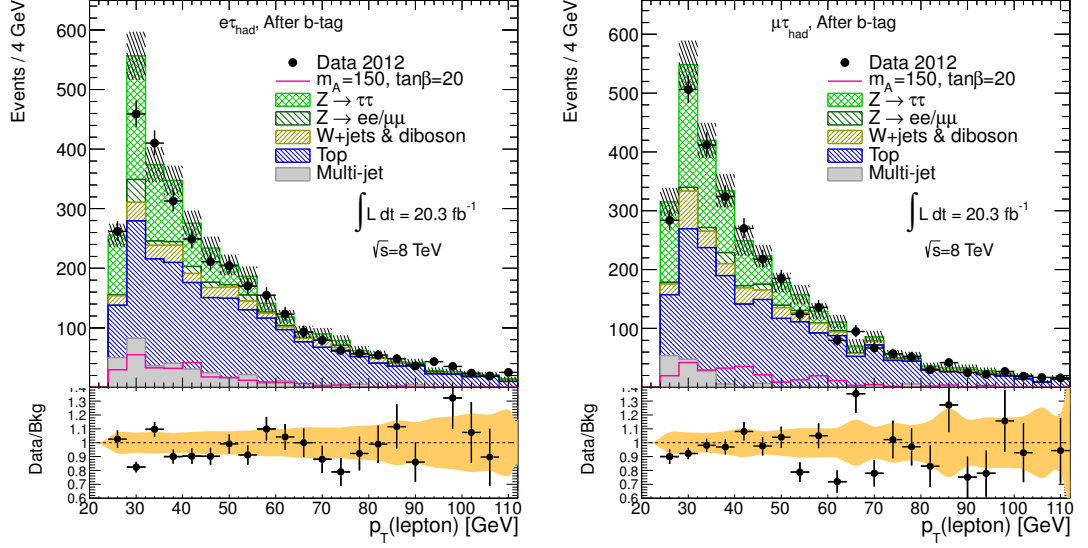


Figure 7.8: The transverse momentum of the electron or muon, after the b-tag and prior to the veto on a second jet. The shaded bands indicate the total systematic uncertainty.

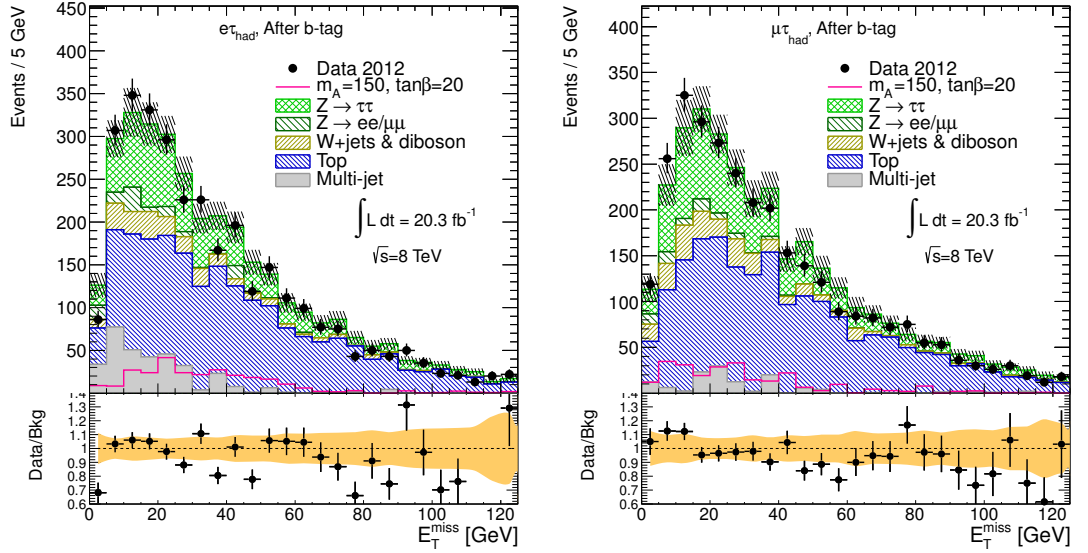


Figure 7.9: The missing transverse energy for the electron and muon channels, after the b-tag and prior to the veto on a second jet. The shaded bands indicate the total systematic uncertainty.

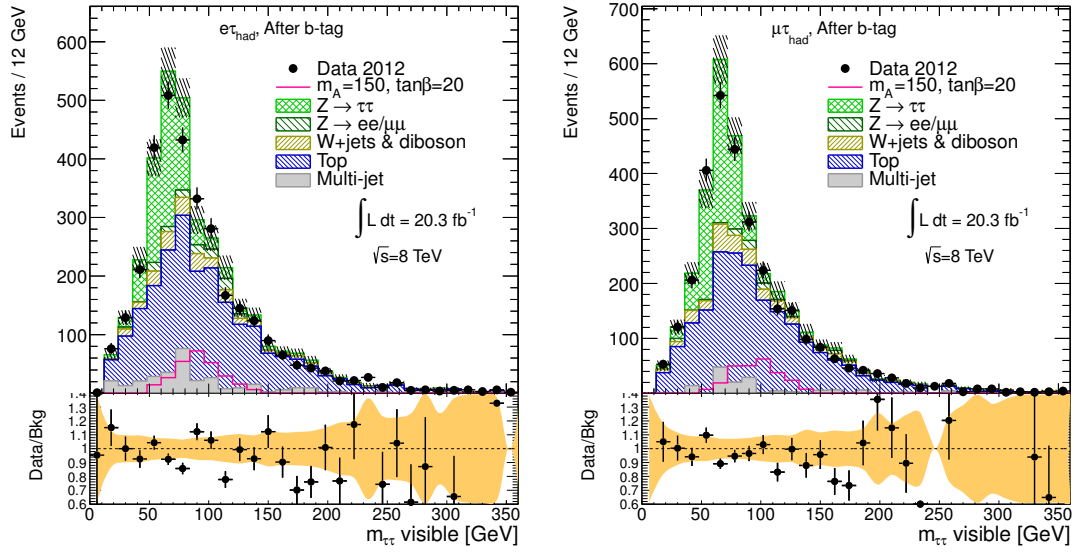


Figure 7.10: The invariant mass of the lepton and the hadronic tau, after the b-tag and prior to the veto on a second jet. The shaded bands indicate the total systematic uncertainty.

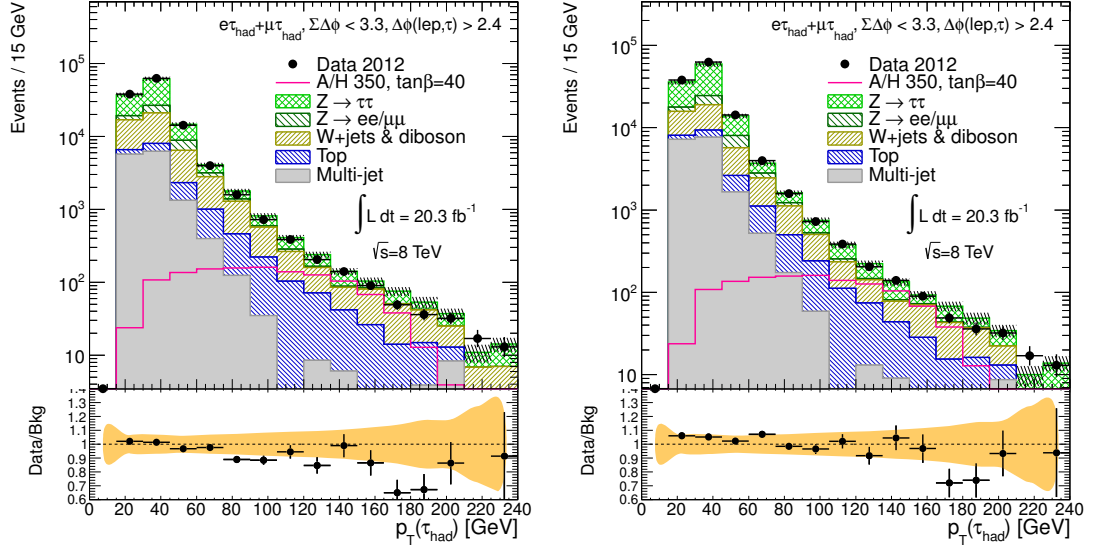


Figure 7.11: The p_T of the hadronic tau, after the cuts $\Sigma\Delta\phi < 3.3$ and $\Delta\phi(\tau, \text{lep}) < 2.4$. The plot on the left uses the low-mass b-veto background estimation technique, while the right uses the high-mass technique. The shaded bands indicate the total systematic uncertainty.

7.5.3 Validation for the high-mass channel

The very tight cut $\Delta p_T > 45$ implies that all events passing the high-mass selection are in the tail of the tau p_T distribution, and care must be taken to ensure that this is modelled correctly. As described above, all of the control regions are defined with a very tight p_T cut on the tau. Figure 7.11 shows the tau p_T distribution, using either the low-mass b-veto scale factors or the high-mass scale factors. The low-mass scale factors are seen to do well in the first few bins which contain most of the data, but perform poorly in the very high bins. Meanwhile, the high-mass scale factors give a much better agreement in the tail, which is the only important region for the high mass selection. This gives confidence that the background estimation is performing as it was intended. A similar argument applies to the level of agreement seen in Figure 6.5 in Section 6.

Chapter 8

SYSTEMATIC UNCERTAINTIES

Many sources of systematic uncertainty may affect the predicted signal and background event yields, as well as the expected shape of the invariant mass distributions. These can be broadly divided into three categories: systematics related to the background estimation methods, systematics related to the detector simulation and MC modelling, and systematics related to the theoretical predictions.

8.1 Systematic Uncertainties due to background estimation*8.1.1 Systematic Uncertainty on the Multi-jet estimate*

As discussed in Section 7.2, the main uncertainty on the multi-jet estimate is due to the instability of the opposite-sign vs. same-sign ratio, by varying the mass and the isolation criteria. The uncertainty assigned from the isolation criteria depends on the sub-channel and reaches 30% (see Table 7.6). A 10-12% uncertainty is assigned due to the variation with mass in the low-mass b-veto and high-mass categories.

8.1.2 Systematic Uncertainties on the fake tau control regions

For top backgrounds, there is a mixture of true hadronic taus (from a W decay) and taus coming from a misidentified jet in the event. In order to obtain the correct scale factor, it is important that this ratio is the same in the signal region and the control regions. Because the control regions require a b-tagged jet, there is one less jet available to fake the tau in the control region as compared to the b-veto or high-mass signal regions. To gauge the impact of this effect, an alternative control region was defined which requires 2 b-tags. The difference in the scale factor obtained in this region, up to 8%, is applied as a systematic on the top background estimation.

For the W+jets background, the estimation rests on the validity of the extrapolation

between regions of low and high $\Sigma\Delta\phi$. To test this, “intermediate” regions were defined which require $3.3 < \Sigma\Delta\phi < 3.8$. The difference in the scale factor obtained in these regions, which is up to 6%, is applied as a systematic on the W+jets prediction.

For the $Z \rightarrow \ell\ell$ backgrounds where the tau is faked by an associated jet, alternative regions were defined by varying the mass window around the Z peak. No statistically significant deviations were observed.

8.1.3 Systematic Uncertainties for $Z \rightarrow \tau\tau$ embedding

Two sources of systematic uncertainty are considered for the embedding method. The first relates to the isolation requirements placed on the original muons. By default, only a very loose isolation requirement is made, in order to avoid biasing the tau energy reconstruction or identification variables. To see if this loose criterion introduces any bias, an alternative sample is defined with no isolation applied. Similarly, to gauge the impact from possible impurities in the sample, another alternative sample is made using tighter isolation cuts. In both cases, the difference to the default is taken as a systematic.

The second systematic comes from the subtraction of the energy deposited by the muon in the calorimeter. This is done by using simulated muons in a separate *mini-event*. The uncertainty is assessed by varying the cell energy to be subtracted up and down by 30%.

The effect of the systematic variations on the predicted event yield is shown in Table 8.1, and the effect on the ditau invariant mass shape is shown in Figure 8.1.

Finally, because the normalization of the embedding sample is determined by the theoretical cross-section, branching ratio and acceptance, we assign these additional uncertainties, which are detailed in Section 8.3, as an uncertainty on the normalization.

8.2 Systematic Uncertainties from Theory

Cross section uncertainties Table 8.2 summarizes the cross section uncertainties for the various simulated signal and backgrounds [56] [30] [31]. Simulated backgrounds which are scaled in control regions are not included, which leaves only Z boson and diboson production. The uncertainty for the signal cross section depends on $\tan\beta$, the Higgs boson type (A , h or H) and mass.

Table 8.1: Systematic uncertainty for embedded samples: ratios of the yields after the systematic variations in the embedded samples have been applied along with their statistical uncertainties.

Sample	Tight Isolation	No Isolation	Muon Calo	
			Deposition +30%	Deposition -30%
b -tag, electron	0.1	2.9	1.2	1.7
b -tag, muon	0.1	1.6	1.2	5.6
b -veto, electron	<0.1	0.3	0.1	1.8
b -veto, muon	<0.1	0.3	0.2	4.8
high mass	0.1	0.5	0.8	0.5

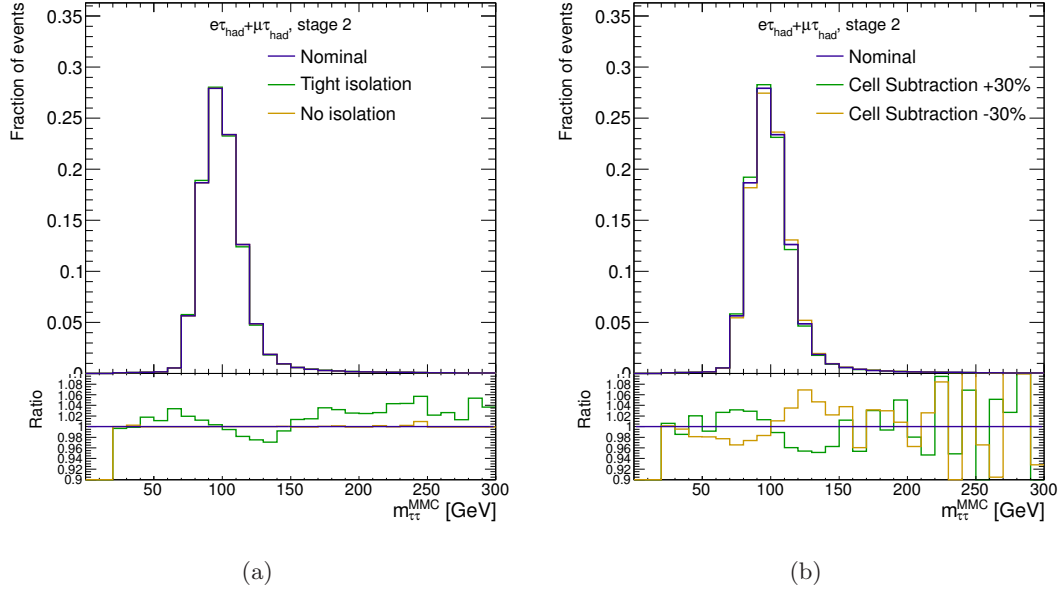


Figure 8.1: The effect of the embedding uncertainties on the ditau MMC mass distribution, shown for the low-mass b -veto selection.

Acceptance systematics The Monte Carlo event generation cannot be expected to perfectly reproduce the kinematics from proton collisions, and for this reason uncertainties are applied to account for possible mis-modelling of the selection efficiency.

Uncertainties on the signal acceptance have been evaluated by producing Monte Carlo samples with varied parameters, and observing the effect at truth-level on the kinematic tau, lepton, and jet cuts. For the b -quark associated production, produced with SHERPA [29], the factorization scale was varied up and down by a factor of 2, and the renormalization scale by a factor of 10%. Additionally, effects from the parton distribution function and the matching between the matrix element and parton shower were considered. The effect of these variations is summarized in Table 8.3, and the effects were summed in quadrature to give the final uncertainty. For the gluon fusion production process, produced with POWHEG [27] and Pythia 8 [28], the initial and final state radiation uncertainties were varied up and down, the renormalization and factorization scales were varied simultaneously (renormalization scale by 10 % and factorization scale by factor 2), and the parton density function was varied in the same way as for the b -quark associated production. These variations are summarized in Table 8.4.

8.3 *Detector-related Systematic Uncertainties*

The following sources of systematics were considered. A summary may be seen in Tables 8.6 through 8.10.

Trigger efficiency Systematic uncertainties on the single-lepton trigger efficiencies are approximately 1-2%, for both the electron and muon channels [43] [57].

Electron reconstruction The systematic uncertainties considered for electrons can be grouped into three categories: energy scale and resolution, identification efficiency and calorimeter isolation [43]. The systematic uncertainties on the energy scale and resolution corrections for electrons are independently evaluated. For the electromagnetic calorimeter energy clusters identified as electrons, typically a 1% (3%) energy scale uncertainty is assigned in the central (forward) region. As the MC simulation does not reproduce the

Table 8.2: Systematic uncertainty for the simulated background sample cross sections. For the singal uncertainties see the Appendix for more details.

Sample	Uncertainty
Background Samples	
$Z \rightarrow ee/\mu\mu/\tau\tau$	$\pm 5 \%$
Diboson	$\pm 6 \%$
Signal Samples($\tan \beta = 20$)	
$ggA/h/H$ ($m_A \leq 300$ GeV)	$< 15\%$
$bbA/h/H$ ($m_A \geq 120$ GeV)	$-(< 20)\%, +(< 9) \%$
$bbA/h/H$ ($m_A = 110$ GeV)	$-(< 25)\%, +(< 9) \%$
$bbA/h/H$ ($m_A = 100$ GeV)	$-(< 28)\%, +(< 9) \%$
$bbA/h/H$ ($m_A = 90$ GeV)	$-(< 30)\%, +(< 9) \%$

Table 8.3: Signal acceptances for several systematic deviations of the theory parameters contributing to the higgs boson and b-quark production. The different variations are added in quadrature to a total uncertainty on the signal acceptance in the b-tag and b-veto sample.

Event yields	b-tag deviation [%]	b-veto deviation [%]
CKKW down	-4.5 ± 0.8	0.2 ± 0.4
CKKW up	-10.0 ± 0.8	0.9 ± 0.4
Fac. scale up	-22.2 ± 0.7	3.3 ± 0.4
Fac. scale down	14.6 ± 0.9	-3.5 ± 0.4
Ren. scale down	0.2 ± 0.8	-0.6 ± 0.4
Ren. scale up	-0.9 ± 0.8	-0.5 ± 0.4
PDF	± 0.1	± 0.2
Total (up)	14.6 ± 1.2	3.4 ± 0.7
Total (down)	-24.7 ± 1.6	-3.6 ± 0.7

Table 8.4: Signal acceptances for several systematic deviations of the theory parameters contributing to the higgs boson production through gluon fusion. The different variations are added in quadrature to a total uncertainty on the signal acceptance in the b-tag and b-veto sample.

Event yields	b-tag deviation [%]	b-veto deviation [%]
FSR down	-13.4 ± 3.2	0.4 ± 0.3
FSR up	22.6 ± 4.2	-0.1 ± 0.3
ISR down	-15.0 ± 3.2	0.2 ± 0.3
ISR up	21.9 ± 4.1	0.3 ± 0.3
Ren./Fac. scales down	0.9 ± 3.6	-0.2 ± 0.3
Ren./Fac. scales up	0.7 ± 3.6	0.4 ± 0.3
PDF	± 0.0	± 0.1
Total (up)	31.5 ± 7.8	0.7 ± 0.6
Total (down)	-20.1 ± 4.5	-0.2 ± 0.4

electron energy resolution correctly, a 1%-4% energy smearing for the constant term is applied in order to obtain the nominal value for acceptance. The uncertainties on the electron reconstruction and identification scale factors have been evaluated to be 3%. The effect of the uncertainty from the isolation requirements is estimated by varying the isolation energy correction by $\pm 2\%$ ($\pm 4\%$) for electrons with p_T greater (smaller) than 20 GeV.

Muon reconstruction Similar to the electrons, the systematic uncertainties associated with the muon momentum resolution and identification efficiency corrections on the total number of selected events are calculated by varying them according to their uncertainties: $\pm 1\%$ for both the momentum resolution and identification efficiency [57].

Tau energy scale and efficiency The τ_h energy scale systematics depend on the number of reconstructed τ_h tracks, the energy of the τ_h and the pseudorapidity η . For 1-prong τ -leptons, the total systematic uncertainty on energy scale ranges from 4.5% at low p_T to

Table 8.5: Systematic uncertainty for the ALPGEN Z +jets MC.

Sources	Uncertainty
ALPGEN Z +jets MC	
Matrix element parton 12 GeV	-3.3 ± 1.7 %
Matrix element parton $\Delta R > 0.4$	-2.2 ± 1.6 %
Different scale definition (iqopt2)	0.4 ± 1.5 %
Different PDF set (MRST2001J)	2.0 ± 1.5 %
Q^2 Scale (double)	-1.9 ± 1.5 %
Q^2 Scale (half)	-3.3 ± 1.5 %
MLM matching condition (p_T 15 GeV)	-6.0 ± 1.4 %
MLM matching condition (ΔR 0.4)	1.0 ± 1.7 %
kt factor (double)	-5.4 ± 1.5 %
kt factor (half)	-0.1 ± 1.6 %
Total (up)	2.3 %
Total (down)	-9.8 %

2% for $p_T > 100$ GeV [52]. For 3-prong τ -leptons, the systematic uncertainty on energy scale ranges from 6.5% at low p_T to 3% for $p_T > 100$ GeV. The effect of this uncertainty is evaluated by scaling all reconstructed taus passing the identification criteria. The τ identification efficiency uncertainties depend on the number of prongs and $|\eta|$ and vary from $\sim 3\%$ to $\sim 10\%$ [51].

Jet energy scale and resolution The jet energy scale affects the analysis via the b -jet identification requirement at low mass, and via the W and top control region definitions at both low and high mass. Additionally, the jet energy measurement uncertainty is propagated to the E_T^{miss} . It has been seen that four sources of uncertainty on the JES have a strong effect on the analysis: modelling/theory uncertainties, uncertainty related to the intercalibration between pseudorapidities, uncertainty of the quark-gluon jet composition in the samples, and uncertainty on the different response to quark and gluon jets [46] [47]. These uncertainties are propagated to the invariant mass distribution via the E_T^{miss} . Smaller effects come from the presence of b -jets in the final state, and from the level of pileup. These change only the overall normalization of the samples. The total uncertainty on the final event yield from the jet energy scale is usually about 7 to 10%. An uncertainty on the jet energy resolution is evaluated by applying a gaussian smearing to all jets and repeating the selection. Additionally, the efficiency of the Jet Vertex Fraction (JVF) cut comes with a p_T and eta-dependent uncertainty, which is typically a few percent.

b -jet identification The b -tagging decision carries an uncertainty for both positive and negative outcomes and hence both b -tag and b -veto samples are affected, as is the high-mass sample via the top control region definition. Separate scale factors are used for b -jets, c -jets, and light-quark or gluon jets [58] [59] [60]. Typical uncertainties on these scale factors are about 3%. The rare cases where a tau is mis-identified as a b -jet are treated as charm-jets, with an additional uncertainty.

Missing Transverse Energy The systematic uncertainty due to the energy scales of electrons, τ jets and jets are propagated to the E_T^{miss} vector. Additionally, there are E_T^{miss} -

specific uncertainties on the scale and resolution, due to the treatment of the energy that is not associated to a physics object. These uncertainties are usually a small effect compared to the uncertainties on the energy scale of high p_T objects.

Luminosity The uncertainty in integrated luminosity is taken to be 2.8% [61].

Pileup In order to have a proper match between the pileup conditions in data and MC, MC events are re-weighted according to the average interactions per bunch crossing, $\langle \mu \rangle$. It has been seen that a proper description of the minimum bias vertex multiplicity is obtained if the $\langle \mu \rangle$ value in MC is first scaled by a factor of 1.11 before re-weighting to match data. The uncertainty on this value of 1.11 is 0.03, and is taken as a systematic for the analysis.

A summary of the detector-related systematics is given in Tables 8.6, 8.7, 8.8, 8.9, and 8.10.

Table 8.6: Summary of detector-related systematic uncertainties for background and signal samples after the b-tagged selection for the electron channel (%). Signal refers to bbA production with $m_A = 150$ GeV and $\tan\beta = 20$. When uncertainty is asymmetric the one with the maximum absolute value is considered.

b -tag selection, electron							
	Embedding						
	Signal	$Z \rightarrow \tau\tau$	QCD	W +jets	$Z \rightarrow ll$	Top	Diboson
JES B-Jets	1.0	-	0.5	4.8	0.2	2.6	1.2
JES Eta Modelling	1.9	-	0.4	7.5	2.3	5.8	4.3
JES Flavor Composition	1.9	-	1.3	8.5	5.0	3.7	5.8
JES Flavor Response	1.9	-	2.2	7.9	3.8	3.0	5.8
JES Modelling	1.4	-	1.6	14.0	3.5	8.0	7.0
JES Pileup	1.0	-	1.9	6.6	3.1	4.4	7.0
TES	4.1	4.6	2.5	1.5	7.2	0.3	4.1
MET Scale/Resolution	0.7	-	1.7	1.1	0.0	0.4	0.0
JER	0.9	-	0.2	12.4	4.7	1.5	2.1
JVF	6.1	-	7.2	8.5	1.6	5.8	2.2
Tau ID	3.4	3.4	0.1	0.9	0.0	0.5	1.7
Lepton to tau fake rate	0.0	0.0	0.0	0.1	5.1	0.0	0.0
Electron ID and energy	2.1	2.1	0.8	1.4	2.5	1.6	2.4
Muon ID and momentum	0.0	0.0	0.7	1.3	0.8	1.1	0.0
Pileup	1.2	0.1	0.4	1.5	0.8	0.5	1.2
b-jet tagging efficiency	5.5	-	0.2	1.9	0.4	3.7	0.7
c and light jet tagging rate	0.3	-	2.9	5.8	4.9	1.0	9.4
Luminosity	2.8	2.8	-	-	2.8	-	2.8

Table 8.7: Summary of detector-related systematic uncertainties for background and signal samples after the b-tagged selection for the muon channel(%). Signal refers to bbA production with $m_A = 150$ GeV and $\tan\beta = 20$. When uncertainty is asymmetric the one with the maximum absolute value is considered.

b -tag selection, muon							
	Embedding						
	Signal	$Z \rightarrow \tau\tau$	QCD	W +jets	$Z \rightarrow ll$	Top	Diboson
JES B-Jets	1.0	-	0.2	5.6	0.1	2.4	0.0
JES Eta Modelling	0.6	-	4.0	12.5	6.7	5.5	3.5
JES Flavor Composition	1.2	-	6.4	13.3	6.6	4.0	5.5
JES Flavor Response	1.2	-	1.6	6.8	2.8	2.3	3.5
JES Modelling	0.7	-	6.2	9.4	6.8	6.9	4.5
JES Pileup	1.8	-	3.9	8.4	2.9	4.0	3.5
TES	6.2	4.9	24	6.2	39	1.4	9.6
MET Scale/Resolution	0.0	-	7.6	1.0	3.4	0.5	0.0
JER	2.3	-	8.6	18.3	9.3	4.0	8.0
JVF	1.6	-	35	13.8	5.7	5.4	2.7
Tau ID	3.5	3.4	0.1	0.9	0.0	0.5	1.5
Lepton to tau fake rate	0.0	0.0	0.0	0.1	0.0	0.1	0.0
Electron ID and energy	0.0	0.1	2.1	1.5	12.2	1.0	0.0
Muon ID and momentum	2.1	2.1	2.1	0.8	3.1	1.0	2.1
Pileup	1.4	0.1	5.3	1.4	1.2	0.6	0.6
b-jet tagging efficiency	5.5	-	1.3	1.7	0.4	3.6	0.8
c and light jet tagging rate	0.2	-	9.6	5.7	5.8	1.0	7.7
Luminosity	2.8	2.8	-	-	2.8	-	2.8

Table 8.8: Summary of detector-related systematic uncertainties for background and signal samples after the b-veto selection for the electron channel (%). Signal refers to ggA production with $m_A = 150$ GeV and $\tan\beta = 20$. When uncertainty is asymmetric the one with the maximum absolute value is considered.

<i>b</i> -veto selection, electron							
	Embedding						
	Signal	$Z \rightarrow \tau\tau$	QCD	W +jets	$Z \rightarrow ll$	Top	Diboson
JES B-Jets	0.0	-	-	0.1	0.0	2.5	0.1
JES Eta Modelling	0.4	-	1.0	1.8	1.0	3.3	1.2
JES Flavor Composition	0.5	-	1.4	2.4	1.3	0.5	1.9
JES Flavor Response	0.7	-	0.8	1.4	0.6	0.4	1.2
JES Modelling	0.6	-	1.2	2.2	1.2	3.5	1.7
JES Pileup	0.8	-	0.6	1.0	0.3	1.6	0.8
TES	1.9	3.4	1.1	1.0	0.6	1.3	3.8
MET Scale/Resolution	0.2	-	0.1	0.2	0.3	0.4	0.3
JER	1.6	-	0.3	0.4	1.1	2.0	0.4
JVF	0.1	-	0.2	0.2	0.5	2.3	0.2
Tau ID	3.4	3.4	0.1	0.1	0.0	0.2	1.7
Lepton to tau fake rate	0.0	0.0	0.3	0.1	14.9	0.0	0.3
Electron ID and energy	1.8	2.1	0.8	1.8	1.5	1.3	1.8
Muon ID and momentum	0.0	0.0	0.5	1.2	0.4	1.1	0.0
Pileup	0.4	0.3	0.1	0.2	0.3	0.0	0.2
b-jet tagging efficiency	0.0	-	0.2	0.3	0.0	18.9	0.1
c and light jet tagging rate	0.8	-	0.6	0.8	0.6	2.6	1.8
Luminosity	2.8	2.8	-	-	2.8	-	2.8

Table 8.9: Summary of detector-related systematic uncertainties for background and signal samples after the b -veto selection for the electron channel (%). Signal refers to ggA production with $m_A = 150$ GeV and $\tan\beta = 20$. When uncertainty is asymmetric the one with the maximum absolute value is considered.

b -veto selection, muon							
	Embedding						
	Signal	$Z \rightarrow \tau\tau$	QCD	W +jets	$Z \rightarrow ll$	Top	Diboson
JES B-Jets	0.0	-	0.1	0.1	0.0	1.9	0.0
JES Eta Modelling	0.4	-	3.0	1.9	0.5	1.9	0.8
JES Flavor Composition	0.6	-	3.8	2.3	0.7	0.5	1.9
JES Flavor Response	0.5	-	2.7	1.5	0.4	0.8	1.1
JES Modelling	0.5	-	2.6	2.1	0.6	2.7	1.5
JES Pileup	0.5	-	1.5	1.0	0.3	1.8	0.8
TES	2.6	3.3	2.0	0.7	1.0	0.8	4.4
MET Scale/Resolution	0.3	-	0.5	0.2	0.3	0.0	0.3
JER	0.7	-	1.1	0.5	0.1	0.2	1.8
JVF	0.2	-	0.3	0.2	0.3	2.3	0.3
Tau ID	3.4	3.4	0.3	0.1	0.0	0.1	1.7
Lepton to tau fake rate	0.0	0.0	0.0	0.1	14.3	0.0	0.0
Electron ID and energy	0.0	0.0	1.4	0.9	0.3	0.9	0.1
Muon ID and momentum	2.1	2.1	1.9	0.9	1.9	1.1	2.2
Pileup	0.6	0.2	0.6	0.2	0.2	0.0	0.2
b -jet tagging efficiency	0.1	-	0.6	0.3	0.0	18.7	0.1
c and light jet tagging rate	0.9	-	1.7	0.8	0.4	2.7	1.7
Luminosity	2.8	2.8	-	-	2.8	-	2.8

Table 8.10: Summary of detector-related systematic uncertainties for background and signal samples after the high-mass selection (%). Signal refers to bbA production with $m_A = 350$ GeV and $\tan\beta = 20$. When uncertainty is asymmetric the one with the maximum absolute value is considered.

high-mass selection, electron + muon							
	Embedding						
	Signal	$Z \rightarrow \tau\tau$	QCD	W +jets	$Z \rightarrow ll$	Top	Diboson
JES B-Jets	0.1	-	0.7	0.4	0.0	0.3	0.0
JES Eta Modelling	0.3	-	3.9	1.6	3.1	0.6	1.6
JES Flavor Composition	0.2	-	4.8	2.6	4.6	0.5	1.6
JES Flavor Response	0.2	-	5.4	1.8	3.1	0.2	1.6
JES Modelling	0.2	-	4.4	2.1	3.1	0.1	1.6
JES Pileup	0.2	-	4.1	1.0	0.0	0.2	1.6
TES	4.5	8.2	6.2	6.0	14.3	0.4	4.6
MET Scale/Resolution	0.1	-	2.2	0.2	0.0	0.1	0.5
JER	0.1	-	7.9	0.5	2.7	1.4	3.9
JVF	0.0	-	0.1	0.3	0.0	0.3	0.0
Tau ID	3.5	3.2	0.3	0.3	0.0	0.3	2.3
Lepton to tau fake rate	0.0	0.0	0.6	0.6	9.1	0.3	0.5
Electron ID and energy	1.1	2.0	2.7	1.2	0.8	0.9	0.7
Muon ID and momentum	1.1	1.8	0.2	0.2	0.6	0.0	1.3
Pileup	0.4	0.3	2.0	0.4	1.9	0.3	1.5
b-jet tagging efficiency	0.0	-	1.3	1.9	0.0	7.8	0.0
c and light jet tagging rate	0.0	-	1.9	0.5	0.0	1.0	0.0
Luminosity	2.8	2.8	-	-	2.8	-	2.8

Chapter 9

STATISTICAL PROCEDURE

As mentioned before, the ditau invariant mass, calculated with the Missing Mass Calculator, is used as the final discriminant. In order to test the background and signal hypotheses, the binned MMC distribution is used to construct a likelihood function, which measures the compatibility of the data with a given hypothesis in a frequentist manner. Systematic uncertainties are incorporated into the likelihood as nuisance parameters, which affect the predicted yield and are allowed to vary with gaussian constraints. If the likelihood for the background-only hypothesis, or for a given signal hypothesis, is much lower than the maximum likelihood, then this hypothesis is excluded.

In particular, the likelihood function is given by:

$$\mathcal{L}(\mu, \boldsymbol{\theta}) = \prod_{\substack{j = \text{bin and} \\ \text{category}}} \mathcal{F}_P(N_j | \mu \cdot s_j(\boldsymbol{\theta}) + b_j(\boldsymbol{\theta})) \prod_{\theta_i} \mathcal{F}_G(\theta_i | 0, 1). \quad (9.1)$$

Here N_j is the observed number of events in bin j , s_j and b_j are the expected events from signal and background, respectively, and μ is the “signal strength” parameter. A value of $\mu = 0$ would correspond to the background-only hypothesis, while $\mu = 1$ would correspond exactly to the signal prediction of the m_A - $\tan\beta$ point in question. $\mathcal{F}_P(N_j | \mu \cdot s_j + b_j)$ denotes the Poisson distribution with mean $\mu \cdot s_j + b_j$ for variable N_j . The nuisance parameters are denoted by the vector $\boldsymbol{\theta}$. $\mathcal{F}_G(\theta_i | 0, 1)$ is a gaussian distribution with mean 0 and variance 1, for the individual nuisance parameter θ_i . Both the signal and background predictions are functions of the nuisance parameters.

A signal hypothesis may be excluded if the value $\mu = 1$ is disfavored at the 95% confidence level. To calculate the upper limit on μ , the compatibility of the observed or expected dataset with the signal-plus-background prediction is checked using a modified frequentist

approach. The test statistic \tilde{q}_μ , used in the upper limit derivation, is defined as

$$\tilde{q}_\mu = \begin{cases} -2 \ln \left(\frac{\mathcal{L}(\mu, \hat{\boldsymbol{\theta}}_\mu)}{\mathcal{L}(0, \hat{\boldsymbol{\theta}}_0)} \right) & \text{if } \hat{\mu} < 0, \\ -2 \ln \left(\frac{\mathcal{L}(\mu, \hat{\boldsymbol{\theta}}_\mu)}{\mathcal{L}(\hat{\mu}, \hat{\boldsymbol{\theta}})} \right) & \text{if } 0 \leq \hat{\mu} \leq \mu, \\ 0 & \text{if } \hat{\mu} > \mu, \end{cases} \quad (9.2)$$

where $\hat{\mu}$ and $\hat{\boldsymbol{\theta}}$ refer to the global maximum of the likelihood, while $\hat{\boldsymbol{\theta}}_\mu$ corresponds to the conditional maximum likelihood for a given μ . It can be seen that a value of μ less than the global maximum is never excluded, while for other values the comparison is made either to $\hat{\mu}$ or to 0, whichever is larger. For the characterization of an excess, a similar test statistic q_0 is used, which is defined as

$$q_0 = \begin{cases} -2 \ln \left(\frac{\mathcal{L}(0, \hat{\boldsymbol{\theta}}_0)}{\mathcal{L}(\hat{\mu}, \hat{\boldsymbol{\theta}})} \right) & \text{if } \hat{\mu} \geq 0, \\ 0 & \text{if } \hat{\mu} < 0, \end{cases} \quad (9.3)$$

In order to calculate a p -value for the background or background+signal hypothesis, it is necessary to know the full expected distribution of the test statistic. This may be done by running an ensemble of pseudo-experiments, for a given μ and nuisance parameter configuration, and observing the resulting distribution. However, this requires un-realistically large computing resources, and therefore an asymptotic approximation to the distribution is used, derived in Reference [62]. In this approximation,

$$p_\mu = 1 - \Phi(\tilde{q}_\mu) \quad (9.4)$$

and in particular,

$$p_0 = 1 - \Phi(q_0), \quad (9.5)$$

where $\Phi(q)$ is the cumulative distribution function of the gaussian distribution. The validity of the approximation has been tested using pseudo-experiments at a number of points.

The significance Z can be calculated directly from the p -value using the following formula:

$$Z_\mu = \Phi^{-1}(1 - p_\mu), \quad (9.6)$$

where Φ is defined as before. If the p -value of the background-only hypothesis is so low that the significance Z_0 rises above 5, then the experiment is considered to have produced

a discovery; or if it rises above 3, then the experiment has shown “evidence”. In a similar fashion, one might say that if the p -value for the $\mu = 1$ hypothesis is so low that the significance Z_1 is above 2, then the signal hypothesis is excluded at the 95% confidence level. However, such a convention would potentially lead to some undesirable effects in the case of a downward fluctuation of the data. By definition, we should expect that 5% of the time, the data will fluctuate down in such a way that the background-only hypothesis is “excluded” under this definition (as are supersymmetry, extra dimensions, and essentially any other scenario). To avoid claiming ridiculous exclusion of models to which we are not sensitive, a modified criterion, known as CL_s [63] is used. With this convention, instead of requiring the p -value for the signal hypothesis to be less than 5%, we require the ratio of p -values p_1/p_0 to be less than 5%. In this way, a downward fluctuation of the data will result in a lower p_0 , and therefore will guard against false exclusion.

It is useful to compare the resulting significance or exclusion limits to the expected result from background only or signal plus background. To do this, the so-called “Asimov” dataset is used. The Asimov dataset is defined as the dataset which, when used to evaluate the estimator for all nuisance and signal parameters, gives the true value for the parameters. The expected sensitivity is evaluated by replacing the actual data with the Asimov dataset, and redoing the full statistical procedure. Additionally, uncertainty on the expected sensitivity or exclusion may be obtained using asymptotic formulae derived in Reference [62].

Chapter 10

RESULTS

Figures 10.1, 10.2, and 10.3 show the final ditau invariant mass distributions. No statistically significant excess is observed in any channel.

Although no evidence for additional Higgs bosons has been found, the result may be used to set upper limits on the parameter $\tan\beta$ as a function of m_A , using the cross sections predicted in the MSSM. In order to do this, one must specify the SUSY parameters which affect the cross-section predictions at higher orders, and the results presented assume a set of parameters known as the m_h^{max} scenario [64]. For each point considered in the $(m_A, \tan\beta)$ plane, the contributions of each of the three neutral Higgs bosons are added, considering both the gluon fusion and b-associated production mechanisms. Using this as the signal model, a 95% confidence level limit can be set on the signal strength parameter μ (see Section 9). If $\mu = 1$ is excluded at the 95% confidence level, then the point is excluded. This procedure is followed for a grid of points on the $(m_A, \tan\beta)$ plane: sixteen mass points between 90 and 800 GeV, and fifteen $\tan\beta$ points between 5 and 60. To determine the exact limit on $\tan\beta$, an extrapolation is done between the lowest grid point which is excluded, and the highest grid point which is not.

Figures 10.4, 10.5, and 10.6 show the limits obtained in this manner.

In order to make the results applicable to a wider range of models beyond the m_h^{max} scenario, an additional interpretation of the analysis is performed. In this case, the signal model is assumed to be a single additional scalar boson, produced either via gluon fusion or b-associated production, and decaying into tau leptons. An upper limit on the cross-section times branching ratio for such a process can be set as a function of the mass of the new boson. This interpretation may be seen in Figures 10.7 and 10.8.

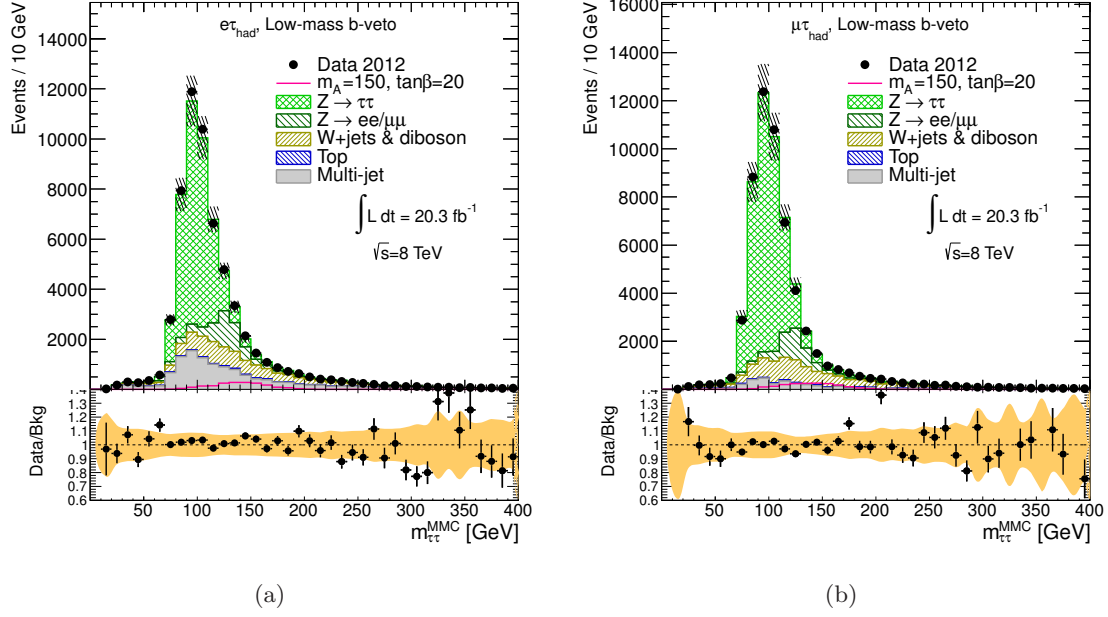


Figure 10.1: Final invariant mass distributions after the low-mass b-veto selection, for the electron (left) and muon (right) sub-channels.

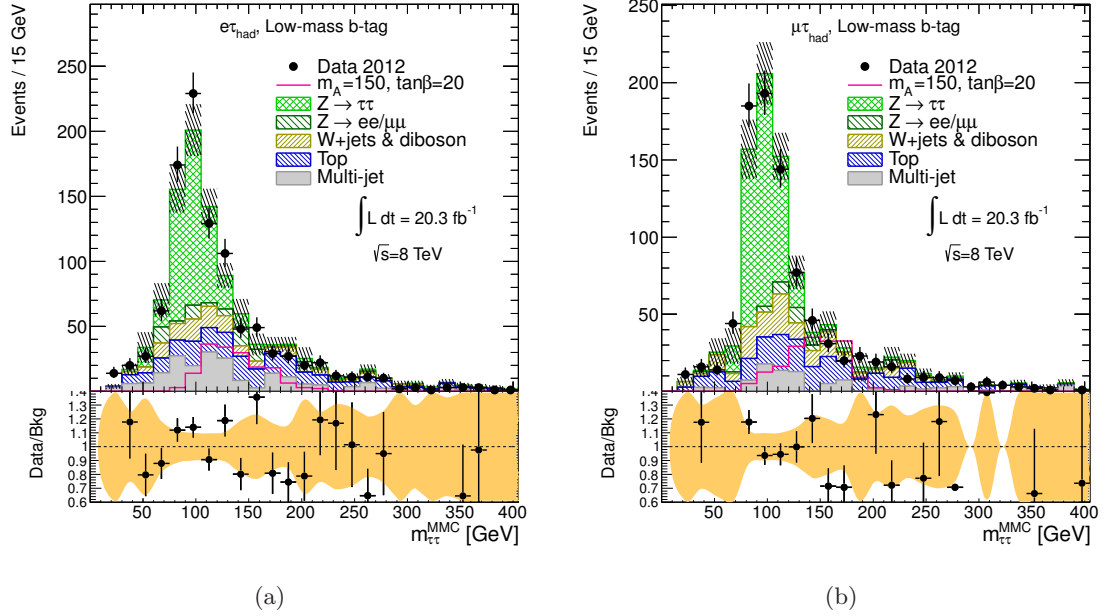
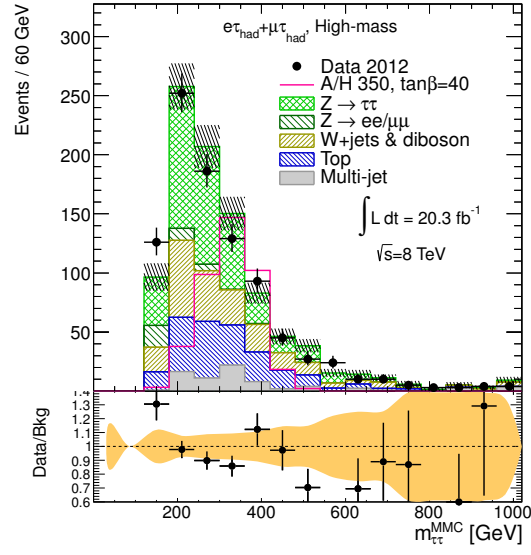


Figure 10.2: Final invariant mass distributions after the low-mass b-tag selection, for the electron (left) and muon (right) sub-channels.



(a)

Figure 10.3: Final invariant mass distributions after the high mass selection. Electron and muon events are combined.

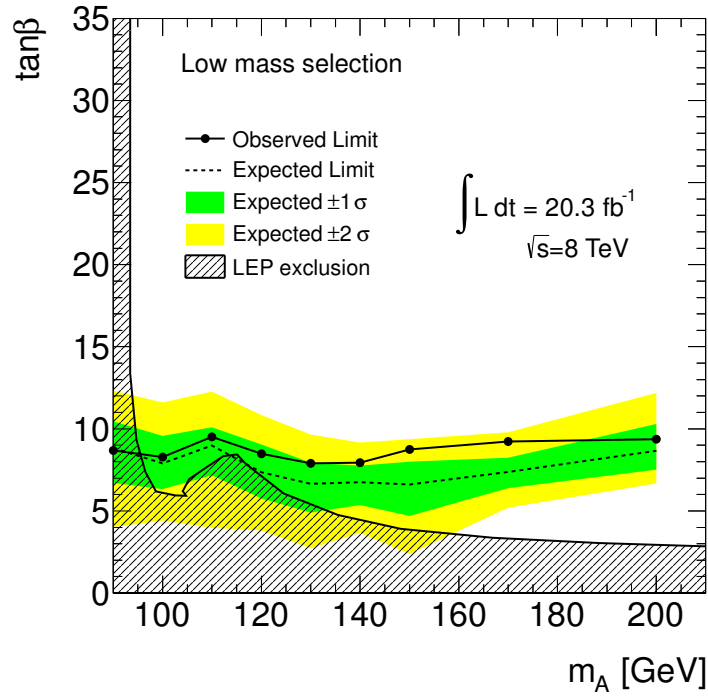


Figure 10.4: Upper limit on $\tan\beta$ as a function of m_A , obtained from the low-mass analysis. The b-tag and b-veto sub-channels are combined.

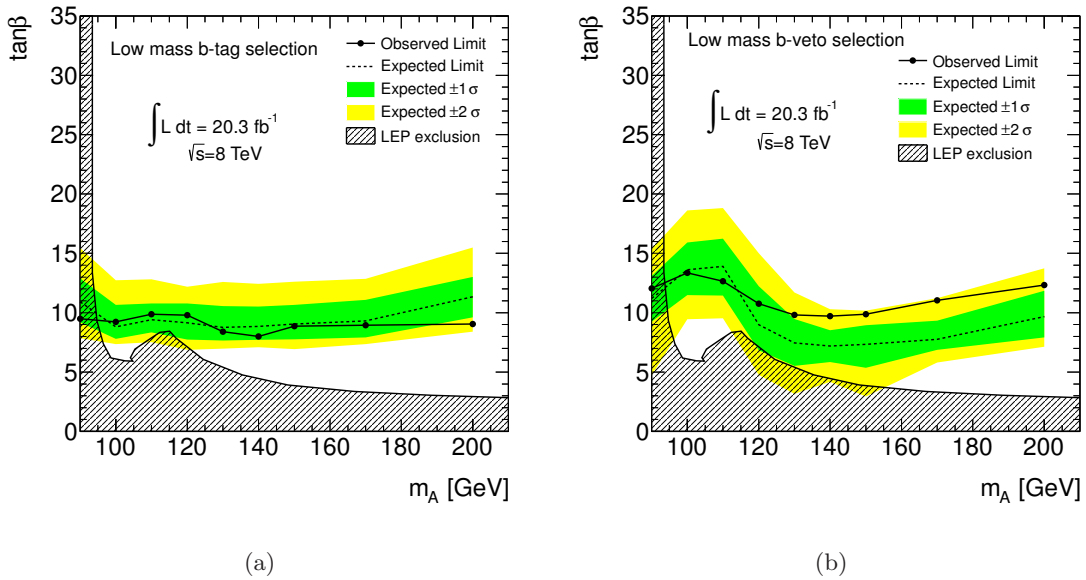


Figure 10.5: Upper limit on $\tan\beta$ as a function of m_A , obtained from the low-mass b-tag (left) and b-veto (right) analyses.

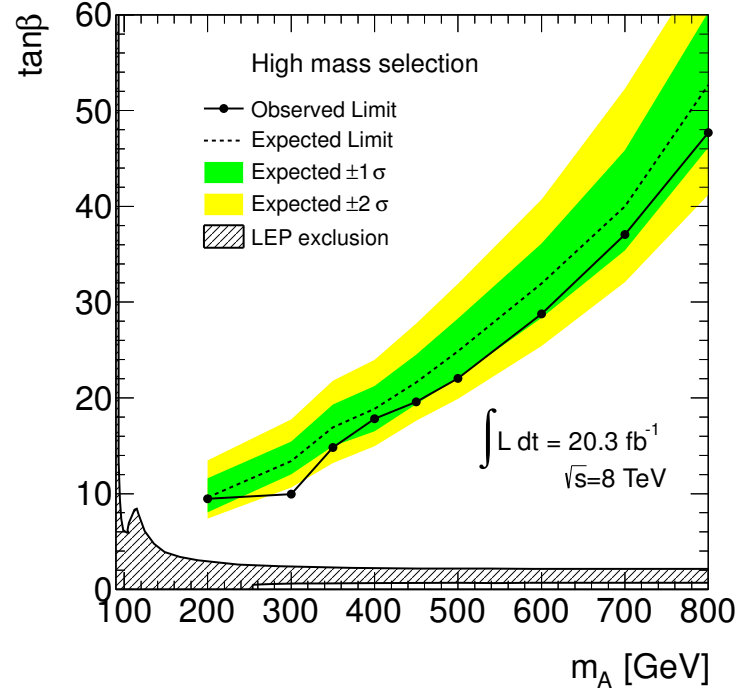


Figure 10.6: Upper limit on $\tan\beta$ as a function of m_A , obtained from the high-mass analysis.

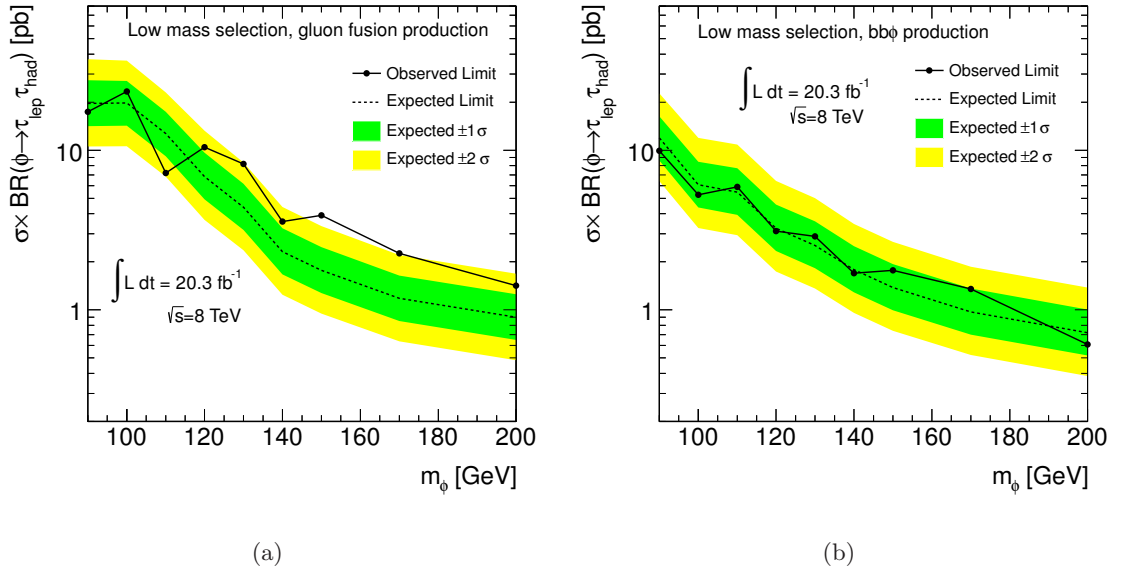


Figure 10.7: Upper limit on the cross-section times branching ratio for a new scalar boson produced via gluon fusion (left) or b-associated production (right), obtained from the low-mass analysis. The b-tag and b-veto sub-channels are combined.

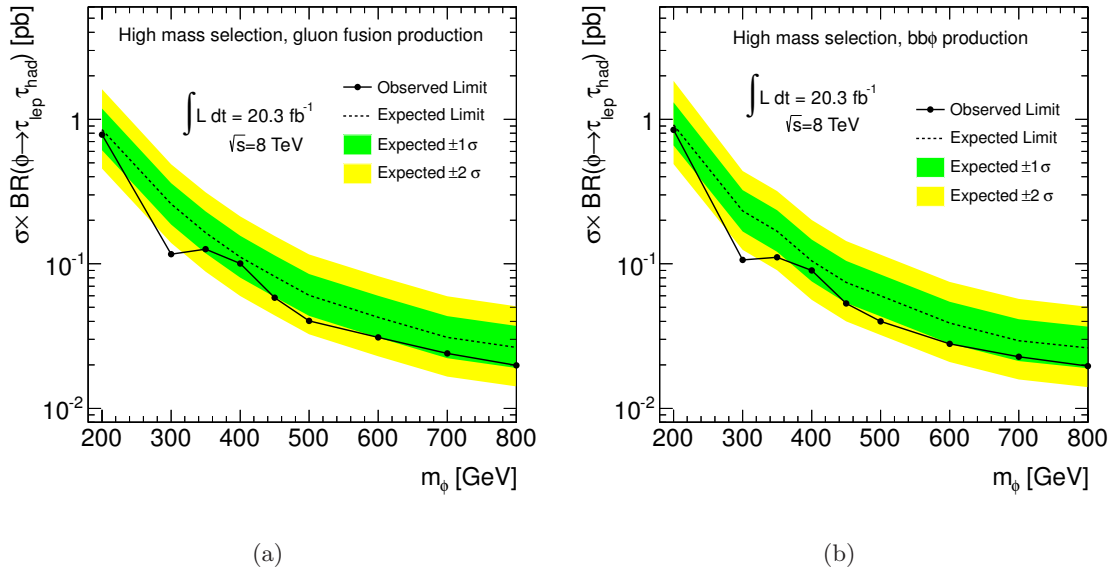


Figure 10.8: Upper limit on the cross-section times branching ratio for a new scalar boson produced via gluon fusion (left) or b-associated production (right), obtained from the high-mass analysis.

Chapter 11

SUMMARY AND CONCLUSIONS

A search for the neutral Higgs bosons of the Minimal Supersymmetric Standard Model has been presented. The analysis searches for the decay into tau leptons, with one tau decaying leptonically and the other hadronically, and the gluon fusion and b-associated production modes are considered. Separate analyses are performed for low-mass and high-mass signal hypotheses, with the former further divided into sub-channels with and without a b-tagged jet to target the two production mechanisms.

Wherever possible, the Standard Model backgrounds were predicted directly using the data. When comparing these predictions to the observed data, no significant deviation is observed. This result has been used to set limits on the parameter $\tan\beta$ as a function of the pseudoscalar mass m_A . Additionally, limits on the cross-section times branching ratio for a generic scalar boson produced in either of the two production mechanisms have been set.

Compared to previous results from the ATLAS experiment [65], the present analysis represents a very large improvement. Although that result was obtained using only 4.7 fb^{-1} of data at a center-of-mass energy of 7 TeV, the gain in sensitivity from the present analysis is approximately twice as large as what would be expected simply from the increase in cross-section and luminosity. The present analysis may also be compared to the latest preliminary results from the CMS [66] experiment, which were based on 17 fb^{-1} of 7 and 8 TeV data, and included the $\tau_{lep}\tau_{lep}$ channel in addition to the $\tau_{lep}\tau_{had}$ channels. The present analysis gives lower limits for all masses above 500 GeV, while the expected sensitivity is better for masses above 350 GeV. For lower masses, where the $\tau_{lep}\tau_{lep}$ channel contributes significantly, the CMS result remains the most sensitive.

Although no evidence for the MSSM Higgs sector has yet been observed, the motivation for this model remains strong. While the available parameter space has been tightly constrained, there are still many regions which are unexplored, and this search channel

promises to remain relevant as more data is delivered by the LHC.

BIBLIOGRAPHY

- [1] A. Djouadi, “The anatomy of electroweak symmetry breaking Tome II: The Higgs bosons in the Minimal Supersymmetric Model,” *Phys. Rep.*, vol. 459, 2008.
- [2] Particle Data Group Collaboration, J. Beringer et al., “Review of particle physics,” *Phys.Rev.*, vol. D86, p. 010001, 2012.
- [3] The ATLAS Collaboration, “Observation of a new particle in the search for the Standard Model Higgs boson with the ATLAS detector at the LHC,” *Physics Letters B*, vol. 716, pp. 1–29, 2012.
- [4] The CMS Collaboration, “Observation of a new boson at a mass of 125 GeV with the CMS experiment at the LHC,” *Physics Letters B*, vol. 716, pp. 30–61, 2012.
- [5] P. W. Higgs, “Broken symmetries, massless particles and gauge fields,” *Phys. Lett.*, vol. 12, p. 132, 1964.
- [6] P. W. Higgs, “Broken Symmetries and the Masses of Gauge Bosons,” *Phys. Rev. Lett.*, vol. 13, p. 508, 1964.
- [7] P. W. Higgs, “Spontaneous Symmetry Breakdown without Massless Bosons,” *Phys. Rev.*, vol. 145, p. 1156, 1966.
- [8] F. Englert and R. Brout, “Broken Symmetry and the Mass of Gauge Vector Mesons,” *Phys. Rev. Lett.*, vol. 13, p. 321, 1964.
- [9] G. S. Guralnik, C.R. Hagen and T. W. B. Kibble, “Global Conservation Laws and Massless Particles,” *Phys.Rev.Lett.*, vol. 13, p. 585, 1964.
- [10] S. Glashow, “Partial Symmetries of Weak Interactions,” *Nucl.Phys.*, vol. 22, pp. 579–588, 1961.
- [11] S. Weinberg, “A model of leptons,” *Phys. Rev. Lett.*, vol. 19, pp. 1264–1266, 1967.
- [12] A. Salam, “Weak and Electromagnetic Interactions,” *Conf.Proc.*, vol. C680519, pp. 367–377, 1968.
- [13] M. Gell-Mann, “Symmetries of baryons and mesons,” *Phys. Rev.*, vol. 125, pp. 1067–1084, 1962.

- [14] C. Berger *et al.*, “A Study of Jets in electron Positron Annihilation Into Hadrons in the Energy Range 3.1-GeV to 9.5-GeV,” *Phys.Lett.*, vol. B78, p. 176, 1978.
- [15] G. Arnison *et al.*, “Experimental Observation of Isolated Large Transverse Energy Electrons with Associated Missing Energy at $s^{1/2} = 540$ GeV,” *Phys.Lett.*, vol. B122, pp. 103–116, 1983.
- [16] M. Banner *et al.*, “Observation of Single Isolated Electrons of High Transverse Momentum in Events with Missing Transverse Energy at the CERN anti-p p Collider,” *Phys.Lett.*, vol. B122, pp. 476–485, 1983.
- [17] G. Arnison *et al.*, “Experimental Observation of Lepton Pairs of Invariant Mass Around 95-GeV/c² at the CERN SPS Collider,” *Phys.Lett.*, vol. B126, pp. 398–410, 1983.
- [18] P. Bagnaia *et al.*, “Evidence for $Z^0 \rightarrow e^+ e^-$ at the CERN anti-p p Collider,” *Phys.Lett.*, vol. B129, pp. 130–140, 1983.
- [19] The CDF Collaboration, “Observation of Top Quark Production in $\bar{p}p$ Collisions with the Collider Detector at Fermilab,” *Phys. Rev. Lett.*, vol. 74, pp. 2626–2631, 1995.
- [20] The D0 Collaboration, “Search for High Mass Top Quark Production in $p\bar{p}$ Collisions at $\sqrt{s} = 1.8$ TeV,” *Phys. Rev. Lett.*, vol. 74, pp. 2422–2426, 1995.
- [21] A. Djouadi, “The anatomy of electroweak symmetry breaking Tome I: The Higgs boson in the Standard Model,” *Phys. Rep.*, vol. 457, 2008.
- [22] S. P. Martin, “A Supersymmetry primer,” 1997.
- [23] J. Wess and B. Zumino, “Supergauge Transformations in Four-Dimensions,” *Nucl.Phys.*, vol. B70, pp. 39–50, 1974.
- [24] H. E. Haber and G. L. Kane, “The search for supersymmetry: Probing physics beyond the standard model,” *Phys. Rep.*, vol. 117, p. 75, 1985.
- [25] L. Evans and P. Bryant, “LHC Machine,” *JINST*, vol. 3, p. S08001, 2008.
- [26] The ATLAS Collaboration, “The ATLAS Experiment at the CERN Large Hadron Collider,” *JINST*, vol. 3, p. S08003, 2008.
- [27] S. Alioli *et al.*, “Higgs boson production in gluon fusion,” *JHEP*, vol. 02, p. 029, 2009.
- [28] T. Sjostrand, S. Mrenna and P. Skands, “PYTHIA 6.4 physics and manual,” *JHEP*, vol. 05, p. 026, 2006.

- [29] T. Gleisberg *et al.*, “Event generation with SHERPA 1.1,” *JHEP*, vol. 02, p. 007, 2009.
- [30] LHC Higgs Cross Section Working Group, “Handbook of LHC Higgs Cross Sections: 1. Inclusive Observables,” 2011.
- [31] LHC Higgs Cross Section Working Group, “Handbook of LHC Higgs Cross Sections: 2. Differential Distributions,” 2012.
- [32] M. L. Mangano *et al.*, “ALPGEN, a generator for hard multiparton processes in hadronic collisions,” *JHEP*, vol. 07, p. 001, 2003.
- [33] J. Alwall *et al.*, “Comparative study of various algorithms for the merging of parton showers and matrix elements in hadronic collisions,” *Eur. Phys. J.*, vol. C53, p. 473, 2008.
- [34] B. P. Kersevan and E. Richter-Was, “The Monte Carlo Event Generator AcerMC 2.0 with Interfaces to PYTHIA 6.2 and HERWIG 6.5,” 2004. arXiv 0405247v1.
- [35] G. Corcella *et al.*, “HERWIG 6: an event generator for hadron emission reactions with interfering gluons (including supersymmetric processes),” *JHEP*, vol. 01, p. 010, 2001.
- [36] S. Jadach, J. H. Kuhn and Z. Was, “TAUOLA - a library of Monte Carlo programs to simulate decays of polarized τ leptons,” *Comput. Phys. Commun.*, vol. 64, p. 275, 1990.
- [37] E. Barberio, B. V. Eijk and Z. Was, “Photos - a universal Monte Carlo for QED radiative corrections in decays,” *Comput. Phys. Commun.*, vol. 66, p. 115, 1991.
- [38] The ATLAS Collaboration, “The ATLAS Simulation Infrastructure,” *Eur.Phys.J.*, vol. C70, p. 823, 2010.
- [39] S. Agostinelli *et al.*, “GEANT4 - a simulation toolkit,” *Nucl. Instrum. Meth.*, vol. A506, p. 250, 2003.
- [40] The ATLAS Collaboration, “Expected Performance of the ATLAS Experiment - Detector, Trigger and Physics,” CERN-OPEN-2008-020.
- [41] R. Kalman, “A new approach to linear filtering and prediction problems,” *Journal of Basic Engineering*, vol. 82, pp. 35–45, 1960.
- [42] The ATLAS Collaboration, “Performance of primary vertex reconstruction in proton-proton collisions at $\sqrt{s} = 7$ TeV,” ATLAS-CONF-2010-069.

- [43] The ATLAS Collaboration, “Electron performance measurements with the ATLAS detector using the 2010 LHC proton-proton collision data,” *Eur.Phys.J.*, vol. C72, p. 1909, 2012.
- [44] The ATLAS Collaboration, “Improved electron reconstruction in ATLAS using the Gaussian Sum Filter-based model for bremsstrahlung,” ATLAS-CONF-2012-047.
- [45] W. Lampl *et al.*, “Calorimeter Clustering Algorithms : Description and Performance,” ATL-LARG-PUB-2008-002.
- [46] The ATLAS Collaboration, “Single hadron response measurement and calorimeter jet energy scale uncertainty with the ATLAS detector at the LHC,” *Eur.Phys.J.*, vol. C73, p. 2305, 2013.
- [47] The ATLAS Collaboration, “Jet energy measurement with the ATLAS detector in proton-proton collisions at $\sqrt{s} = 7$ TeV,” *Eur.Phys.J.*, vol. C73, p. 2304, 2013.
- [48] M. Cacciari, G. P. Salam, and G. Soyez, “The anti- k_t jet clustering algorithm,” *JHEP*, vol. 04, p. 063, 2008.
- [49] The ATLAS Collaboration, “Data-Quality Requirements and Event Cleaning for Jets and Missing Transverse Energy Reconstruction with the ATLAS Detector in Proton-Proton Collisions at a Center-of-Mass Energy of $\sqrt{s} = 7$ TeV,” ATLAS-CONF-2010-038.
- [50] The ATLAS Collaboration, “Commissioning of the ATLAS high-performance b-tagging algorithms in the 7 TeV collision data,” ATLAS-CONF-2011-102.
- [51] The ATLAS Collaboration, “Performance of the Reconstruction and Identification of Hadronic tau Decays in ATLAS with 2011 Data,” ATLAS-CONF-2012-142.
- [52] The ATLAS Collaboration, “Determination of the tau energy scale and the associated systematic uncertainty in proton-proton collisions at $\sqrt{s} = 8$ TeV with the ATLAS detector at the LHC in 2012,” ATLAS-CONF-2013-044.
- [53] J. H. Friedman, “Greedy function approximation: A gradient boosting machine,” *Annals of Statistics*, vol. 29, pp. 1189–1232, 2000.
- [54] The ATLAS Collaboration, “Performance of Missing Transverse Momentum Reconstruction in Proton-Proton Collisions at 7 TeV with ATLAS,” *Eur.Phys.J.*, vol. C72, p. 1844, 2012.
- [55] A. Elagin, P. Murat, A. Pranko, and A. Safonov, “A New Mass Reconstruction Technique for Resonances Decaying to di-tau,” *Nuclear Instrumentations and Methods*, vol. 654, pp. 481–489, 2010.

- [56] J.M.Butterworth *et al.*, “Single Boson and Diboson Production Cross Sections in pp Collision at $\sqrt{s}=7$ TeV,” ATL-COM-PHYS-2010-695.
- [57] The ATLAS Collaboration, “Muon reconstruction efficiency in reprocessed 2010 LHC proton-proton collision data recorded with the ATLAS detector,” ATLAS-CONF-2011-063.
- [58] The ATLAS Collaboration, “Measurement of the Mistag Rate of b -tagging algorithms with 5 fb^{-1} of Data Collected by the ATLAS Detector,” ATLAS-CONF-2012-040.
- [59] The ATLAS Collaboration, “Measurement of the b -tag Efficiency in a Sample of Jets Containing Muons with 5 fb^{-1} of Data from the ATLAS Detector,” ATLAS-CONF-2012-043.
- [60] The ATLAS Collaboration, “Measuring the b -tag efficiency in a $t\bar{t}b\bar{b}$ sample with 4.7 fb^{-1} of data from the ATLAS detector,” ATLAS-CONF-2012-097.
- [61] The ATLAS Collaboration, “Improved luminosity determination in pp collisions at $\sqrt{s}=7$ TeV using the ATLAS detector at the LHC,” 2013. arXiv 1302.4393.
- [62] G. Cowan, K. Cranmer, E. Gross, and O. Vitells, “Asymptotic formulae for likelihood-based tests of new physics,” *Eur.Phys.J.*, vol. C71, p. 1554, 2011.
- [63] A. L. Read, “Presentation of search results: the CL_s technique,” *J.Phys.*, vol. G28, pp. 2693–2704, 2002.
- [64] M. Carena, S. Heinemeyer, C. E. M. Wagner, and G. Weiglein, “Suggestions for benchmark scenarios for MSSM Higgs boson searches at hadron colliders,” *Eur. Phys. J.*, vol. C26, pp. 601–607, 2003.
- [65] The ATLAS Collaboration, “Search for the neutral Higgs bosons of the Minimal Supersymmetric Standard Model in pp collisions at $\sqrt{s}=7$ TeV with the ATLAS detector,” *JHEP*, vol. 1302, p. 095, 2013.
- [66] The CMS Collaboration, “Higgs to tau tau (MSSM) (HCP),” 2012. CMS-PAS-HIG-12-050.